



Ben-Gurion University of the Negev
The Faculty of Natural Sciences
The Department of Physics

Theoretical model for hysteresis and jumps in disordered 2D superconductors near SIT

Thesis submitted in partial fulfillment of the requirements
for the Master of Sciences degree

Shahar Kasirer

Under the supervision of **Professor Yigal Meir**

January 13, 2021



Ben-Gurion University of the Negev
The Faculty of Natural Sciences
The Department of Physics

Theoretical model for hysteresis and jumps in disordered 2D superconductors near SIT

Thesis submitted in partial fulfillment of the requirements
for the Master of Sciences degree

Shahar Kasirer

Under the supervision of **Professor Yigal Meir**

Signature of student:
Signature of supervisor:
Signature of chairperson of the
committee for graduate studies:

Date: 13/01/2021
Date: 13/1/2021
Date: 13.01.2021

January 13, 2021

BEN-CURION UNIVERSITY OF THE NEGEV

Abstract

The Faculty of Natural Sciences
Physics

Master of Sciences degree

Theoretical model for hysteresis and jumps in disordered 2D superconductors near SIT

by Shahar Kasirer

Many disordered superconductors have been shown to undergo a superconducting to insulating phase-transition (SIT), as a function of disorder or external magnetic field. The insulating phase has some unusual properties. Among them is its I-V curve, which sometimes includes hysteresis and current jumps. Other systems, where a similar behavior was measured, are arrays of superconducting or normal islands, that are connected through tunneling junctions (Josephson junction and quantum dot arrays, respectively). Therefore, superconductors near SIT are usually modeled as disordered arrays. Transport properties are acquired by attributing resistance and capacitance to each junction, and treating tunneling as a perturbation to the states with a well defined number of charge carriers on each island. In those models, fast relaxation is usually assumed, meaning that the system restores equilibrium (electrostatic and thermal) quickly after each tunneling, and thus it is approximated as always being in equilibrium. Those models are successful in explaining some measurement results, including the phase transition itself, but fail to reproduce hysteresis and jumps in the predicted I-V curves. Here, we investigate the slow relaxation limit, where equilibrium is not restored between tunnelings. To do that, we used a model for the electric current through a single conducting island, that was suggested by Korotkov [33]. We analyze this model, and generalize it into a random array model, where disorder is realized by randomly assigning resistance and capacitance to tunneling junctions. We then use Kinetic Monte-Carlo simulations [24], to calculate the voltage and temperature dependencies of the current. We show that our model can reproduce hysteresis and jumps in the I-V curve, for certain parameters, and its results are in qualitative agreement with measurements. We investigate the influence of different model parameters and compare our results with existing models. We conclude with suggestions for ways in which our model can be used in future research.

Acknowledgements

First and foremost, I would like to express my sincere gratitude to my research advisor, Professor Yigal Meir, for offering me this project and providing invaluable guidance throughout the research process.

This work was mainly motivated by experimental results from professor Dan Shahar's research group, at the Weizmann institute. I would like to thank him in person, for sharing his measurement results, and some valuable insights, with me.

A significant part of this work was done at Princeton University, NJ, where I was hosted by Professor Ned Wingreen and by the physics department. I would like to thank Professor Wingreen for his warm hospitality and for useful discussions about this project. I would also like to express my appreciation towards Princeton University's physics department, and its chairperson, Professor Herman Verlinde, for hosting me as if I was one of their students. During my stay at Princeton University, I was lucky enough to be assisted by many great scientists. I would like to give a special thanks to Dr. Lailai Zhu, Dr. Amir Erez and Benjamin Weiner for useful discussions about KMC simulations.

Another important group of people, that helped me throughout this project, are my classmates at Ben-Gurion University of the Negev. A special thanks is given to Tomer Dollberg, Dmitry Boriskovsky, Barak Azulay, Yoav Ironi, Yotam Gal and Yuval Bashan for their useful comments and tips.

Last, but not least, I would like to thank my spouse and life partner, Ravit Inbar, my parents, Yehuda Kasirer and Hadass Kasirer-Izraeli, my sister, Stav Kasirer, and all of my family. Thanks to you, I had the time and peacefulness I had needed to work on his project. A special thanks is given to my father, for proofreading this thesis and for sharing his valuable insights with me.

Contents

| | | |
|----------|--|-----------|
| 1 | Introduction | 1 |
| 1.1 | Superconductivity and SIT | 1 |
| 1.2 | Current-voltage characteristics in the vicinity of SIT | 2 |
| 1.3 | Similar results in other systems | 2 |
| 1.4 | Research goals | 3 |
| 2 | Literature review | 4 |
| 2.1 | Random array model | 4 |
| 2.1.1 | Tunneling rates | 4 |
| 2.1.2 | I-V calculation | 5 |
| 2.1.3 | Normal arrays | 6 |
| 2.1.4 | Superconducting arrays | 7 |
| 2.1.5 | Comparison with measurements | 8 |
| 2.2 | Electrons overheating model | 8 |
| 2.2.1 | Comparison with measurements | 9 |
| 2.3 | Summary | 10 |
| 3 | Proposed model | 11 |
| 3.1 | Single island - RC-SET model | 11 |
| 3.1.1 | Time scales separation | 12 |
| 3.2 | Generalization for a random array | 13 |
| 3.2.1 | Inter-tunneling relaxation | 13 |
| 3.2.2 | Energy | 15 |
| 3.2.3 | Interaction range | 16 |
| 3.2.4 | Master equation | 17 |
| 3.3 | Dynamical simulation | 17 |
| 3.4 | Solution using a graph, for $T = 0$ | 18 |
| 3.4.1 | Master equation solution | 18 |
| 3.4.2 | Steady state gate charge for slow relaxation | 19 |
| 3.5 | Disorder realization | 20 |
| 4 | Results | 21 |
| 4.1 | Single island | 21 |
| 4.1.1 | Conditions for hysteresis and jumps | 21 |
| 4.1.2 | Hysteresis and jumps size | 23 |
| 4.1.3 | Threshold voltage | 24 |

| | | |
|----------|--|-------------|
| 4.1.4 | Arrhenius law | 26 |
| 4.1.5 | Summary | 26 |
| 4.2 | Arrays | 27 |
| 4.2.1 | Interactions between different paths | 29 |
| 4.2.2 | Tunneling capacitance | 30 |
| 4.2.3 | Tunneling resistance | 32 |
| 4.2.4 | Gate capacitance | 34 |
| 4.2.5 | Temperature | 35 |
| 4.2.6 | Superconducting arrays | 37 |
| 4.3 | Comparison with other models | 39 |
| 4.3.1 | Random array model | 39 |
| 4.3.2 | Electrons overheating model | 40 |
| 4.4 | Results summary | 42 |
| 5 | Discussion and conclusion | 44 |
| 5.1 | Research limitations | 44 |
| 5.2 | Future research suggestions | 45 |
| 5.3 | Conclusion | 45 |
| A | Single island detailed analysis | i |
| A.1 | Model equations derivation | i |
| A.1.1 | Inter-tunneling relaxation | i |
| A.1.2 | Tunneling rates | ii |
| A.2 | Master equation solution for $T = 0$ | iii |
| A.2.1 | Maximal and minimal island occupation | iii |
| A.2.2 | Steady-state probabilities | iv |
| A.2.3 | Solution for $V \geq 0$ | iv |
| A.2.4 | Steady state current for fast relaxation | vii |
| A.2.5 | Steady-state gate charge and current for slow relaxation | viii |
| A.2.6 | Current jumps for slow relaxation | xii |
| A.2.7 | Threshold voltage | xvi |
| B | 2 island arrays capacitance matrix | xix |
| B.1 | 1X2 array | xix |
| B.2 | 2X1 array | xx |
| B.3 | Discussion | xx |
| C | Additional results | xxii |
| C.1 | Gate capacitance | xxii |
| C.2 | Tunneling capacitance and resistance | xxiii |
| D | Perpendicular electrons temperature | xxv |
| D.1 | Simulation results | xxvi |

List of Figures

| | | |
|------|--|-------|
| 1.1 | I-V curves for disordered amorphous indium oxide | 2 |
| 2.1 | Electrons overheating model I-V curve | 9 |
| 3.1 | Schematic drawing of the RC-SET model | 12 |
| 3.2 | Schematic drawing of the 2D array model | 14 |
| 3.3 | Master equation graph representation | 19 |
| 4.1 | Single island master equation graph representation | 21 |
| 4.2 | Average voltage on island | 23 |
| 4.3 | Single island I-V curves | 25 |
| 4.4 | Single island R-T curves | 27 |
| 4.5 | Jumps and hysteresis for single column arrays | 28 |
| 4.6 | Comparison between single island and single column array | 29 |
| 4.7 | Hysteresis, jumps and threshold voltages as a function of capacitance disorder | 31 |
| 4.8 | Tunneling resistance effect on current | 32 |
| 4.9 | Hysteresis, jumps and threshold voltages as a function of resistance disorder | 34 |
| 4.10 | I-V curves for different gate capacitance | 35 |
| 4.11 | Temperature effect on current | 36 |
| 4.12 | 2D array R-T curves | 37 |
| 4.13 | Results for a superconducting system | 38 |
| 4.14 | Comparison with previous random array results | 39 |
| 4.15 | Perpendicular electron temperature, for small C_G and big disorder | 41 |
| A.1 | Fast relaxation probability function | v |
| A.2 | Slow relaxation probability function | vi |
| A.3 | Single island I-V curves for fast relaxation | ix |
| A.4 | Lyapunov functional for a single island | xi |
| A.5 | Geometrical approximation for jump separation and height | xiii |
| A.6 | Single island jumps separation | xiv |
| A.7 | Separation between upwards and downwards jumps for single island | xv |
| A.8 | Single island jumps height | xvi |
| A.9 | Single island hysteresis area | xvii |
| A.10 | Single island threshold voltage | xviii |
| B.1 | Schematic drawing of a 1×2 array | xix |
| B.2 | Schematic drawing of a 2×1 array | xx |

| | | |
|-----|---|--------|
| C.1 | Hysteresis, jumps and threshold voltages as a function of gate capacitance | xxii |
| C.2 | Tunneling resistance and capacitance effect on current - additional results | xxiii |
| D.1 | Perpendicular electron temperature, for big C_G and large disorder | xxvi |
| D.2 | Perpendicular electron temperature, for small C_G with no disorder | xxvii |
| D.3 | Perpendicular electron temperature, for big C_G and no disorder | xxviii |

Chapter 1

Introduction

1.1 Superconductivity and SIT

Superconductivity was discovered more than a century ago, when liquefying helium enabled the cooling of samples to a very low temperature [30]. It is phenomenologically characterized by the possibility of a dissipationless electric current and the Meissner effect, the repulsion of magnetic field lines from the interior of the sample [37]. Since its discovery, superconductivity has been a central topic in solid-state physics. It offers a diversity of exotic phenomena, many of them are still not well understood theoretically, and are subjects of ongoing research (for example [22, 42]). One interesting phenomenon, is a surprising phase transition in disordered superconductors.

The microscopic foundation of superconductivity was explained, about fifty years after its discovery, by Bardeen, Cooper, and Schrieffer (BCS) [7]. BCS theory attributes superconductivity to the creation of many-body coherent macroscopic wavefunction, by the pairing of electrons (Cooper pairs). Soon after the emergent of BCS theory it was suggested by Lee and Ma [36] that high disorder can lead to localization of the pairs, and therefore cause a superconductor to insulator transition (SIT). Such a transition has indeed been observed in thin superconducting films, when changing their thickness [26]. Similar transition, induced by the application of a magnetic field, was suggested theoretically [20] and later observed [27]. Understanding this transition is an interesting topic on its own, and may also contribute to better understanding of disordered superconductors in general. In particular, this may contribute to the theoretical understanding of High-temperature superconductors, which are intrinsically disordered [14]. Numerous efforts were taken to investigate this transition, theoretically and experimentally. Nonetheless, some measurements have no agreed upon theoretical explanation yet.

SIT has been observed in different disordered superconductors, including granular superconductors [21], thin Pb, Bi [26], amorphous InO [12, 27, 43] and TiN [8] films. In those experiments, the phase of the system (i.e. insulating, superconducting) is determined by its measured resistance for $T, V \rightarrow 0$. In the superconducting phase, resistance vanishes in this limit, while in the insulating phase it diverges. In some systems [10] the transition is direct (from superconductor to insulator), while in other systems [11] it includes an intervening metallic regime with finite resistance. Both the intervening metallic state and the insulating state can be quite unusual [22]. One of the interesting characteristics of the insulating phase, near the phase transition, is a non-usual I-V curve (current as a function of voltage), which is the focus of the current research.

1.2 Current-voltage characteristics in the vicinity of SIT

The measured I-V curves of thin films in a weak insulating state (near the phase transition) include interesting features. For low temperatures and voltages the measured current is very weak, and the resistance approximately follows Arrhenius law [8]

$$R = R_0 \exp(T_0/T) \quad (1.1)$$

Raising the voltage past a critical threshold value, V^{th} , the current suddenly jumps by few orders of magnitude [43]. This big jump is sometimes followed by smaller jumps [9] until, for large voltage, the curve becomes linear [12].

The current behavior usually exhibits hysteresis in the low voltage regime, i.e. the measured current is different for increasing and decreasing voltage. Hysteresis is very pronounced in some measurements [12] and very weak in others [15].

In fig. 1.1 an example for the described behavior, taken from [12], is shown. In this example, the current exhibits pronounced hysteresis and jumps.

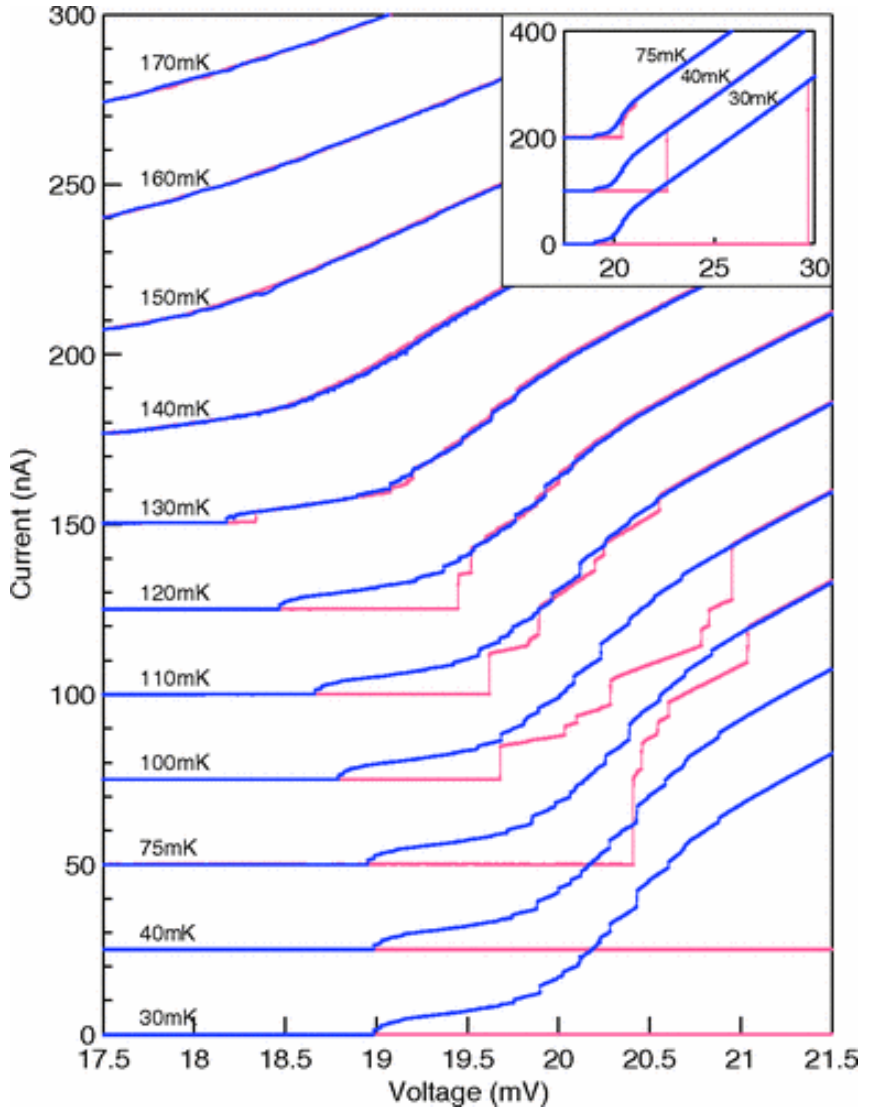


Figure 1.1: I-V curves for disordered amorphous indium oxide. Red - increasing voltage, Blue - decreasing voltage. Taken at different temperatures with an external magnetic field of strength $B = 4T$. The curves are offset from one another by $25nA$. Inset: Expanded V -range view for 30, 40 and 75 mK. Taken from [12].

1.3 Similar results in other systems

Disordered superconductors close to SIT are not the only example where the described behavior was observed. Quantum dot arrays (QDA) are arrays (usually rectangular lattices) of conducting grains surrounded by an insulating medium. Usually one adds a metallic substrate, a gate, over the whole array (the conducting island and the gate are separated by an insulating medium). The gate can be connected to an external voltage source, which is used to control the electrostatic energy and electron density of

the islands. Current jumps and hysteresis, which are qualitatively similar to the presented SIT results, were measured in GaAs QDA [17, 44] and even for a single quantum dot [17]. In those examples, the I-V curves depend strongly on gate voltage. Jumps and hysteresis were only observed for negative gate voltages under a certain value. In another example, a bistable region, where the current was jumping between 2 different values for the same voltage, was measured [40]. As the superconducting samples, QDA also exhibit a phase transition between a conducting state, metallic in this case, to an insulating state. This transition is called Metal to Insulator Transition (MIT) [34].

Another system where SIT was measured is Josephson Junction array (JJA), which is an array of superconducting islands. Hysteresis and blockade region were measured on the insulating side of the transition [2]. Similar results were also measured on the superconducting side, but with I and V interchanged [32].

1.4 Research goals

The main goal of this research is to suggest a theoretical model that will reproduce the measured I-V curve features, with emphasis on current jumps and hysteresis. Preferably, the model will explain the curves measured in superconducting amorphous materials and in Josephson junction and quantum dot arrays. The model should take into account the different physics of each system and be based on reasonable assumptions. Moreover, the suggested model should give testable predictions for the following: When do we expect to measure hysteresis? When do we expect to measure current jumps? How does changing the system parameters affect I-V measurements?

With these goals in mind, we turn to review the research that was already done about related topics, the review will cover relevant theoretical models and experimental results.

Chapter 2

Literature review

There are a few models that can be used to compute the transport properties of amorphous superconductors near SIT. We will focus on two models that have been used to explain the measurements cited in chapter 1.

2.1 Random array model

The common way to account for the measured transport properties in disordered materials is to use a random array model. The sample is modeled as an array of islands, on which the charge carriers are localized. The islands are connected by tunneling barriers. Disorder is introduced through random charge offsets at each island, or through random array parameters (i.e. capacitance, tunneling resistance). For the superconducting case the tunneling barriers are called Josephson Junctions [29]. Josephson junction array (JJA) models have been shown to predict SIT, as a function of the ratio between tunneling and electrostatic terms in the Hamiltonian (see next section)[18]. A similar transition occurs as a function of the magnetic field strength [16]. The success of array models in reproducing SIT, makes them a plausible candidate for explaining the measured transport properties. In addition, the similarity between measurements in QDA, JJA and amorphous superconductors near SIT (see chapter 1), suggests that random array models might be able to explain the measured results in all of them.

2.1.1 Tunneling rates

The Hamiltonian of these models is composed of two terms, $\mathcal{H} = \mathcal{H}_c + \mathcal{H}_T$. \mathcal{H}_c is the electrostatic energy term. Its eigenstates are states with an integer number of charge carriers on each island. Its eigenvalues are the matching electrostatic energies. \mathcal{H}_T is the tunneling term, allowing tunneling of carriers (i.e. electrons or Cooper-pairs) between neighboring islands. The common assumption of all reviewed models is that tunneling of carriers between islands is "weak", therefore \mathcal{H}_T can be treated as a perturbation. In this case we can use a semi-classical description, where the instantaneous state of the system is defined by the number of carriers on each island. Transition between states happens through tunneling, with rates that are calculated using perturbation theory. In [25] the following tunneling rates, for a normal (not superconducting) junction, were calculated

$$\Gamma(\Delta E) = \frac{1}{e^2 R_T} \int_{-\infty}^{\infty} dE \int_{-\infty}^{\infty} dE' f(E) [1 - f(E')] P(-\Delta E - (E' - E)) \quad (2.1)$$

ΔE is the change in electrostatic energy as a result of tunneling. R_T is the tunneling resistance. It is proportional to the density of states on both sides of the junction and to $|T|^2$, where T is the matrix element of the tunneling term in the Hamiltonian. $|T|$ is assumed to be momentum independent. $P(E)$ is the probability that an energy E would be absorbed by the electromagnetic environment, which has a given electric impedance. $f(E)$ is Fermi-Dirac distribution. This result can be interpreted as following: A carrier can tunnel from a state with energy E to one with energy E' if the first is occupied and the second is free (hence the Fermi-Dirac distribution). The extra energy is absorbed by the environment. For a given temperature and impedance, $P(E)$ can be calculated [25]. In the case of low impedance there is no energy absorption

$$P(E) \approx \delta(E) \quad (2.2)$$

and the tunneling rates are given by

$$\Gamma(\Delta E) = \frac{1}{e^2 R_T} \begin{cases} \frac{-\Delta E}{1 - \exp(-\Delta E/k_B T)} & T > 0 \\ -\Delta E \Theta(-\Delta E) & T = 0 \end{cases} \quad (2.3)$$

In the case of high impedance $P(E)$ has Gaussian distribution [25]

$$P(E) = \frac{\exp\left[-(E - E_c)^2 / 4E_c k_B T\right]}{\sqrt{4\pi E_c k_B T}} \quad (2.4)$$

and the resulting rates are

$$\Gamma(\Delta E) = \begin{cases} \frac{1}{e^2 R_T} \int_{-\infty}^{\infty} dE \frac{E}{1 - \exp(-E/k_B T)} \frac{\exp\left[-(\Delta E + E + E_c)^2 / 4E_c k_B T\right]}{\sqrt{4\pi E_c k_B T}} & T > 0 \\ -\frac{\Delta E + E_c}{e^2 R_T} \Theta(-\Delta E - E_c) & T = 0 \end{cases} \quad (2.5)$$

Notice that for $\Delta E < 0$ and $0 < T \ll |\Delta E|$ both eq. 2.3 and 2.5 give $\Gamma \propto \exp(-\Delta E/k_B T)$ and since the current through the junction is proportional to the tunneling rate, it follows Arrhenius law.

2.1.2 I-V calculation

Specifying boundary conditions (i.e. where do we connect electrodes) and using the calculated tunneling rates, we can calculate the current. This is usually done using numerical simulations (e.g. [24]) or, in some special cases, using an analytical calculation (usually an approximated one, see [4] for example).

The rates depend on the change in the total electrostatic energy of the array, which is usually written as

$$E_c = \frac{1}{2} \sum_{i,j} q_i C_{ij}^{-1} q_j + (\text{boundary terms}) \quad (2.6)$$

Where q_i is the charge on i 'th island and C is the capacitance matrix. C_{ii} is i 'th island's self-capacitance. C_{ij} is the mutual capacitance between islands i and j , which is usually taken to be non-zero only for nearest neighbors (although there is evidence that mutual conductance between far islands could be important as well, for large arrays [46]). The electric potential at island i , for a given charge distribution,

is

$$V_i = \sum_j C_{ij}^{-1} q_j \quad (2.7)$$

Calculating the energy difference for tunneling is based on the following assumption: The time it takes to reach electrostatic equilibrium, after tunneling, is negligible compared with the time between tunneling events (which are considered instantaneous themselves). Therefore, energy differences are calculated assuming electrostatic equilibrium at all times.

The model details, which affect the tunneling rates, can differ from one model to another, but the resulting I-V curves have some common features: Because of charge quantization (each carrier can only tunnel as a whole) tunneling requires a finite amount of energy (see chapter 3). Therefore, at low temperatures and voltages, carriers can't tunnel from one electrode to the other and no current flows through the system. This is the Coulomb blockade regime, named that way since Coulomb interactions are responsible for the charging energy. At larger voltages, it becomes possible for carriers to tunnel from one electrode to the other and current can flow. This transition from insulating to conducting state happens when charge carriers can percolate through the array (in analogy to water percolating through porous media) hence it is sometimes called percolation transition. Increasing the voltage further, more and more carriers can tunnel through the array. For small number of carriers this can result in nonlinear I-V curve. This is more likely to happen at small voltage and large disorder, when the carriers move slowly through the array. At larger voltage, carriers move faster through the array and the contribution of more carriers being able to tunnel together becomes negligible. In that case we would see a linear I-V curve. These are the common features of array models. We now turn to reviewing specific models from the literature.

2.1.3 Normal arrays

A frequently used version of this model is a gated rectangular array with M rows and N columns of conducting islands. Each island is connected to its neighbors by tunneling junctions, which function also as capacitors. In addition, each island is connected to the gate voltage by another capacitor (no tunneling is usually allowed to the gate). The electrodes are connected to 2 opposite sides of the array (see fig. 3.2). For the case where all tunneling junctions and all gate capacitors have the same capacitance, C and C_G respectively, the capacitance-matrix can be inverted analytically. Using this analytic solution, Bakhvalov et. al. [6] calculated the electric potential an electron on island i creates at island j

$$V_{i \rightarrow j} = -eC_{j,i}^{-1} \propto \begin{cases} \ln\left(\frac{1}{r}\right) & 1 \ll r \ll \lambda \\ \frac{\exp(-r/\lambda)}{\sqrt{r}} & \lambda \ll r \end{cases} \quad (2.8)$$

$$\lambda \equiv -1/\ln\left(1 + \frac{C_G}{2C} - \sqrt{\left(\frac{C_G}{2C}\right)^2 + \frac{C_G}{C}}\right)$$

where r is the Euclidean distance between the islands (in units of nearest neighbors distance). The logarithmic decay for short distances is the same as for Coulomb interaction in 2D. For larger distances, λ plays the role of a screening length. For $C \gg C_G$ we get $\lambda \rightarrow \infty$, in this case the interaction is un-screened. In the opposite case, $C_G \gg C$ and $\lambda \rightarrow 0$, the interaction is short ranged. In addition,

Bakhvalov et. al. got an expression for the threshold voltage in the large array limit ($M, N \gg 1, \lambda$)

$$V^{th} = \frac{e}{2C_G} \begin{cases} (1 - \frac{2}{\pi}) \sqrt{\frac{C_G}{C}} & C_G \ll C \\ 1 & C_G \gg C \end{cases} \quad (2.9)$$

Using Monte-Carlo simulations, they calculated the steady state current and charge distribution for the case where all tunneling resistance have the same value, R . They showed that, for the case $C_G \ll C$ (the un-screened case), the total number of electrons in the array shows hysteresis, but the I-V curve does not. For high voltage, current approaches an Ohmic behavior $I \propto \frac{M}{RN} V$.

Middleton and Wingreen [38] used a similar model, with the addition of disorder. It was realized in the form of random offset charge that was added to each island. When the voltage on left electrode is increased, electrons can enter the array. But, as a result of the disorder, they get stuck. The distances to which electrons can tunnel, on each row, define together an interface, that grows in a disorder dependent way when voltage is increased. Based on a theory for stochastic growth [31], they found that, for square $N \times N$ arrays in the limit $C_G \gg C$, threshold voltage obeys the following scaling relations:

$$\begin{aligned} \langle V^{th} \rangle \frac{C_G}{eN} - \alpha &\sim N^{-2/3} (\ln N)^{1/2} \\ \frac{\sigma_{V^{th}}}{\langle V^{th} \rangle} &\sim N^{-2/3} (\ln N)^{1/2} \end{aligned} \quad (2.10)$$

$\langle V^{th} \rangle$ is the threshold voltage, averaged over different disorder realizations, and $\sigma_{V^{th}}$ is its standard deviation. α is defined as the threshold in the large array limit, $\alpha \equiv \lim_{N \rightarrow \infty} \langle V^{th} \rangle C_G / Ne$. It is a function of C/C_G . For $C/C_G \rightarrow 0$, numerical simulations yielded the estimation $\alpha \approx 0.388$. Notice that, for large N , the threshold is linear in N , unlike the clean case (equation 2.9) where it is constant. Slightly above the threshold voltage, the current flows on narrow channels. Based on the distance between channel branching, and the current in each of them, they found that the current behaves as a power law

$$I \approx \frac{e}{2RC_G} N \left(\frac{V - V_t}{V_t} \right)^{5/3} \quad (2.11)$$

Experimental results for quantum dot array agree with this result [17].

2.1.4 Superconducting arrays

For a superconducting junction, Josephson's term, $-E_J \cos(\phi)$ [29], is used as the tunneling term in the Hamiltonian. Using perturbation theory, Ingold et. al. [28] calculated the tunneling rates for Cooper pairs

$$\Gamma_{cp}(\Delta E) = \frac{\pi}{2\hbar} E_J^2 P(-\Delta E) \quad (2.12)$$

In addition to Cooper pairs, it is also possible for quasi-particles to tunnel, their tunneling rate are calculated directly from eq. 2.1 [28]

$$\Gamma(\Delta E) = \frac{1}{e^2 R_T} \int_{-\infty}^{\infty} dE \int_{-\infty}^{\infty} dE' \frac{N_s(E) N_s(E' - \Delta E)}{N(0)^2} f(E) [1 - f(E' - \Delta E)] P(E - E') \quad (2.13)$$

where the reduced quasi-particle density of states is [7]

$$\frac{N_s(E)}{N(0)} = \begin{cases} \frac{|E|}{\sqrt{E^2 - \Delta^2}} & |E| > \Delta \\ 0 & |E| < \Delta \end{cases} \quad (2.14)$$

2Δ is the size of the superconducting energy gap, within which the quasiparticle density of states vanishes.

Cole et. al. [13] used those tunneling rates to calculate the I-V curve of a 1D JJA in the high impedance limit (eq. 2.4). They found that the current is proportional to E_J^2 and the voltage has 2 threshold values, one that separates zero conduction from high resistance region and the second separates high from low resistance.

2.1.5 Comparison with measurements

As discussed, the tunneling rates for a normal junction reproduce Arrhenius law for low temperatures. This is approximately true for the superconducting case, where the low temperature ($k_B T \ll \Delta$) is dominated by Cooper-pairs tunneling (only approximately since there is a weak $T^{-1/2}$ dependent in addition to Arrhenius law, see eq. 2.4). Random array models reproduce Coulomb blockade and give predictions for the threshold voltage. Current Jumps are not reproduced by the reviewed models, although jumps in the differential conductance are predicted. Those occur only when the ratio between tunneling resistances on both sides of the island is large [28]. As for hysteresis, in the limit $C_G \gg C$ hysteresis is not possible for the given models [38]. For $C > C_G$ hysteresis is possible, and was demonstrated numerically for the charge distribution [6]. As far as we know, models that are similar to the ones in [1, 38] have never shown to reproduce hysteresis in the I-V curve. One interesting model that does give hysteresis, is a model for a single conducting island, given by Korotkov [33]. In this model, the assumption of fast relaxation time towards electrostatic equilibrium is relaxed. The model that we will suggest here is based on Koroktov's model and thus a comprehensive analysis of the latter would be given in chapter 3.

2.2 Electrons overheating model

The electrons overheating model is a phenomenological model, suggested by Altshuler et. al. [3]. It suggests a fundamentally different reason for the measured I-V curves. The model is based on 3 main assumptions.

1. The electron-electron interaction is strong enough for electrons to be mutually thermalized. Therefore we can introduce the electrons temperature T_{el} .
2. Electron-phonon thermalization mechanism is inefficient at low temperatures. Therefore, T_{el} is not necessarily equal to T_{ph} , the phonons temperature (which is the same as environment's temperature).
3. The conductance is Ohmic, $IR = V$, with resistance that is dependent on electrons temperature and obeys Arrhenius law.

$$R(T_{el}) = R_0 \exp [(T_0/T_{el})] \quad (2.15)$$

where T_0 is a phenomenological constant.

Under these assumptions, electrons temperature is determined by the balance between Joule heating and the cooling by electron-phonon interaction. This gives the heat balance equation [3]

$$\frac{V^2}{R(T_{el})} = \Gamma\Omega \left(T_{el}^\beta - T_{ph}^\beta \right) \quad (2.16)$$

where Γ is the electron-phonon coupling strength and Ω is the volume of the sample. $\beta = 6$ was calculated for the case where thermal phonon wavelength, $\hbar c_s/T$, exceeds electrons elastic mean free path [47]. Together with (2.15) we get an equation for T_{el} as a function of V . Solving for T_{el} , we can calculate the current using ohm's law.

For $T_{ph} \leq T_c = T_0(1 + \beta)^{-(1+\beta)/\beta}$ equation (2.16) has two solutions for voltages in a certain range $V_{LH} < V < V_{HL}$, which means the current has 2 possible values for those voltages. One solution is the "cold branch" where $T_{el} \sim T_{ph}$. This branch has large resistance and thus low current which is sensitive to phonons temperature. The second solution is a hot branch in which $T_{el} > T_{ph}$, the resistance is low and the current is almost independent of T_{ph} . The results of this model for the I-V curve are plotted in fig. 2.1. Increasing the voltage from $V = 0$, current follows the cold branch solution up to V_{HL} . Then, the cold branch vanishes and the current jumps, as it moves to the hot branch solution (from high to low resistance, hence the HL subscript). Decreasing the voltage back, current follows the hot branch solution down to V_{LH} , where it drops to the cold branch solution. For $T_{ph} > T_c$, there is only one solution for T_{el} at a given V , and therefore no hysteresis.

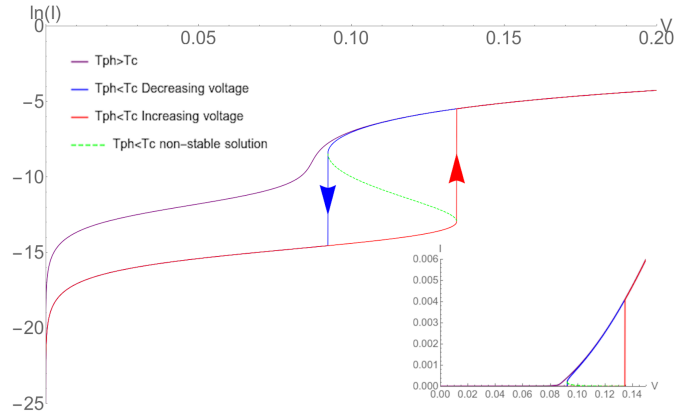


Figure 2.1: Electrons overheating model I-V curve. $\ln(I)$ as a function of V . Red and Blue: increasing and decreasing voltage for $T_{ph} < T_c$, respectively. Purple: $T_{ph} > T_c$. V and I are measured in arbitrary units for $\Gamma\Omega = 1$, $R_0 = 1$, $T_0 = 1$. **Inset** - Linear plot, I as a function of V for the same parameters.

2.2.1 Comparison with measurements

The results of electrons overheating model have several features that compare nicely with measured curves. The qualitative shape of the calculated I-V curve is similar to measurements. For low temperatures, both start in high resistance regime, followed by an abrupt jump, both exhibit hysteresis and both seems linear at high voltages. For high temperatures, the jump becomes smaller and hysteresis is gone. In addition, V_{LH} only slightly changes with T_{ph} , as in measurements. The values of T_0 and T_c can be extracted independently from the data and are in good agreement with the theory [39].

In [35], Levinson et. al. measured resistance in the applied voltage direction and perpendicular to it. In addition, they measured the temperature dependent of resistance for low voltages (where $T_{el} \sim T_{ph}$ by theory) in both directions. Using these measurements, they calculated T_{el} for each direction. Both

calculations gave similar values. This result can be explained by the electrons overheating model, since resistance depends on T_{el} only.

Other aspects of the data cannot be explained using this model. In some measurements there are multiple jumps and hysteresis loops [12, 17], this cannot be accounted for using this model. In addition, for $T_{ph} \ll T_c$ and T_{el} in the cold branch, resistance should satisfy $\ln(R(V \rightarrow 0) / R(V_{HL})) < 1$ [3]. This condition should hold for any $R(T)$ dependency (as long as R depends on a single variable). But measured results [39] clearly do not satisfy this condition.

2.3 Summary

We have reviewed 2 models that can be used to calculate I-V curves of disordered materials. The random array model is based on microscopic foundations (perturbation theory) and is a natural "go to" because of the similarity between the I-V results in amorphous superconductors and arrays. This model can account for the measured transition from high to low resistance and for multiple current jumps but typically don't show hysteresis. The second model is electrons overheating model, which is a phenomenological model. It accounts for the high to low resistance transition and for hysteresis but not for multiple current jumps or hysteresis loops.

Chapter 3

Proposed model

As discussed in chapter 2, the current in a random array model is composed of charge carriers, which tunnel from one island to another. When calculating the current in this model there are 3 relevant time scales to consider:

1. Tunneling time - of the tunneling event itself.
2. Inter-tunneling time - between tunneling events.
3. Relaxation time - how fast an array restores electrostatic and thermal equilibrium after a tunneling has occurred.

In most existing random array models (see chapter 2 for examples), both tunneling and relaxation time scales are assumed to be much shorter than the Inter-tunneling time, and thus treated as instantaneous. While this assumption is justified for the tunneling time (which is of order $\sim 10^{-15}$ sec [19], compared to $\sim 10^{-10} - 10^{-12}$ sec for the inter-tunneling time¹), the relaxation time can be sample dependent. If it is of the same order as the inter-tunneling time, or longer, then we can not assume that the system is always in equilibrium. This may change the dynamics, and in particular the I-V curve. In chapter 2, the electron overheating model [3] was reviewed. In this model, electrons are not in thermal equilibrium with the environment, since their thermal relaxation time (due to electron-phonon coupling) is much longer than the inter-tunneling time (which causes heating). An example, in which the relaxation is towards electrostatic equilibrium, is the RC coupled single electron transistor (RC-SET) which was suggested by Korotkov [33]. The model we suggest is based on it. Next, we will introduce Korotkov's model, for a single conducting island, and analyze its transport properties. Later we will expand it into a random array model.

3.1 Single island - RC-SET model

A schematic drawing of the system is plotted in figure 3.1. First, we will introduce the model and review relevant results from [33]. Then, we will further analyze the model, focusing on current jumps and hysteresis (a more detailed analysis is given in appendix A). In a normal (not superconducting) island, the charge carriers are electrons, each with charge of $-e$. For simplicity, we will instead use positive carriers, with charge $+e$ (this doesn't change the model behavior since every tunneling of a positive carrier can be thought of as a tunneling of a negative one in the opposite direction). Between tunneling

¹Inter tunneling time can be estimated from the measured current, which is in the range of $1 - 100\text{nA}$ [12, 17]

events, the gate charge, Q_G , relaxes towards electrostatic equilibrium [33]

$$\begin{aligned} Q_G(n, t) &= (Q_0 - Q_n) e^{-\frac{t}{\tau}} + Q_n \\ \tau &\equiv \frac{R_G C_G (C_1 + C_2)}{C_\Sigma} \\ Q_n &\equiv \frac{C_G}{C_\Sigma} [(C_1 + C_2) \phi - C_1 V_L - C_2 V_R - ne] \end{aligned} \quad (3.1)$$

where $C_\Sigma \equiv C_1 + C_2 + C_G$, τ is the relaxation time of the system, Q_0 is the initial gate charge on C_G and Q_n is the equilibrium value of Q_G for n excess electrons on the island. The tunneling rates are calculated using eq. 2.1. They depend on energy differences, which, for tunneling through the i 'th junction onto the island (+) or from it (-), are given by (see appendix A)

$$\begin{aligned} W_i^\pm(n, Q_G, V) &= \pm \frac{e}{2} [(U(n \pm 1, Q_G, V) - V_i) \\ &\quad + (U(n, Q_G, V) - V_i)] \end{aligned} \quad (3.2)$$

where $i = L(R)$ for tunneling through the left(right) junction. U is the electric potential on the island

$$U(n, Q_G, V) = \frac{Q_G + ne + C_1 V_L + C_2 V_R}{C_1 + C_2} \quad (3.3)$$

At low temperatures, a carrier can tunnel only if it lowers the energy. Since $U(n \pm 1, Q_G, V) = U(n, Q_G, V) \pm \frac{e}{C_1 + C_2}$, we can say that tunneling requires enough energy to overcome the potential barrier, plus an extra $\frac{e^2}{2(C_1 + C_2)}$. Therefore, tunneling occurs only if the voltage difference is bigger than $\frac{e}{2(C_1 + C_2)}$. Later, this description would help us to gain intuitive understanding of the dynamics.

The tunneling rates for environment with low impedance are given by [25]

$$\Gamma_i^\pm(n, Q_G, V) = -\frac{W_i^\pm(n, Q_G, V)}{e^2 R_i} \begin{cases} \frac{1}{1 - e^{-W_i^\pm(n, Q_G, V)/k_B T}} & T > 0 \\ \Theta(-W_i^\pm(n, Q_G, V)) & T = 0 \end{cases} \quad (3.4)$$

3.1.1 Time scales separation

We can now compare the relaxation time scale, τ , to inter-tunneling times, which are of order $1/\Gamma_i^\pm$. For low voltages and temperatures, the system is in the Coulomb blockade regime and $\Gamma_i^\pm \rightarrow 0$. In that case, relaxation time is always much smaller than inter-tunneling time. For voltages on the order of e/C_i , and

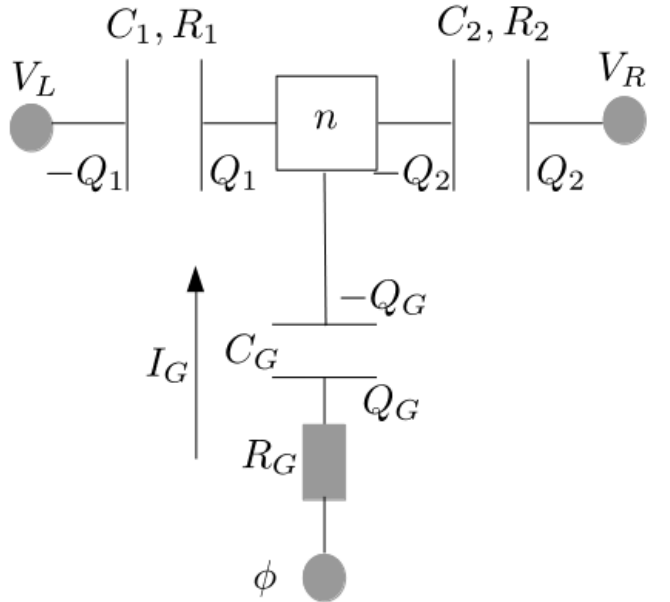


Figure 3.1: Schematic drawing of the RC-SET model. C_i, R_i, Q_i are the capacitance, resistance (or tunneling resistance) and charge of the different components respectively. V_L, V_R, ϕ are the left, right and gate voltages respectively. I_G is the current that flows while charging/discharging the gate capacitor C_G .

above the threshold voltage, $n + Q_G/e$ would be on the order of 1 (as we will see later), so we get

$$\tau\Gamma_i^\pm \sim \frac{R_G C_G}{R_i C_\Sigma} \quad (3.5)$$

For $C_G \gtrsim C_i$, the time scales ratio goes as the ratio between gate resistance, R_G , and tunneling resistances, R_i . In both limits, $R_G \ll R_i$ or $R_G \gg R_i$ we get time scale separation, which allows us to deal with tunneling and relaxation separately (for time scales in the same order, a more complex derivation is needed, see [5]).

For tunneling times that are much shorter than inter-tunneling times, we can consider the tunneling events to be uncorrelated. In this case we can construct a master equation for $p(n)$, the probability to find n carriers on the island

$$\frac{dp(n)}{dt} = \Gamma^+(n-1, Q_G, V) p(n-1) + \Gamma^-(n+1, Q_G, V) p(n+1) - (\Gamma^+(n, Q_G, V) + \Gamma^-(n, Q_G, V)) p(n) \quad (3.6)$$

where $\Gamma^\pm \equiv \Gamma_1^\pm + \Gamma_2^\pm$.

To find a steady state current, we first find a steady state solution to eq. 3.6, $p^*(n, V)$. The current is then given by

$$I(V) = e \sum_n p^*(n, V) [\Gamma_1^+(n, V) - \Gamma_1^-(n, V)] = e \sum_n p^*(n, V) [\Gamma_2^-(n, V) - \Gamma_2^+(n, V)] \quad (3.7)$$

The last equality is the steady state condition. We can get it directly from eq. 3.6 (see appendix A), but it is clear why it has to be correct. To get a steady state, the average rate at which we add and remove carriers from the island must be the same, so that the average occupation $\langle n \rangle$ would be constant.

Equations 3.1 and 3.6 describe the charge dynamics of the model. We will first generalize these results for random arrays. Then, we will describe the methods we used to solve these equations, and calculate transport properties.

3.2 Generalization for a random array

A schematic drawing of a 2D array is given in fig. 3.2. As for a single island, we need to derive an equation that describes the charge relaxation between tunneling events, and a master equation for occupation states probabilities.

3.2.1 Inter-tunneling relaxation

We start from relaxation between tunneling events. The total charge on island (i, j) is (using the notations from fig. 3.2)

$$\begin{aligned} en_{i,j} &= Q_{i,j} - Q_{i,j+1} + Q'_{i,j} - Q'_{i+1,j} - Q_{i,j}^G \\ &= C_{i,j} (V_{i,j} - V_{i,j-1}) - C_{i,j+1} (V_{i,j+1} - V_{i,j}) + C'_{i,j} (V_{i,j} - V_{i-1,j}) - C'_{i+1,j} (V_{i+1,j} - V_{i,j}) - C_{i,j}^G (\phi'_{i,j} - V_{i,j}) \end{aligned} \quad (3.8)$$

where $V_{i,j}$ is the potential on island (i, j) and $\phi'_{i,j} \equiv \phi_{i,j} - \dot{Q}_{i,j}^G R_{i,j}^G$. i goes from zero to $M - 1$, where M is the number of rows in the array. j goes from zero to $N - 1$, where N is the number of columns in the

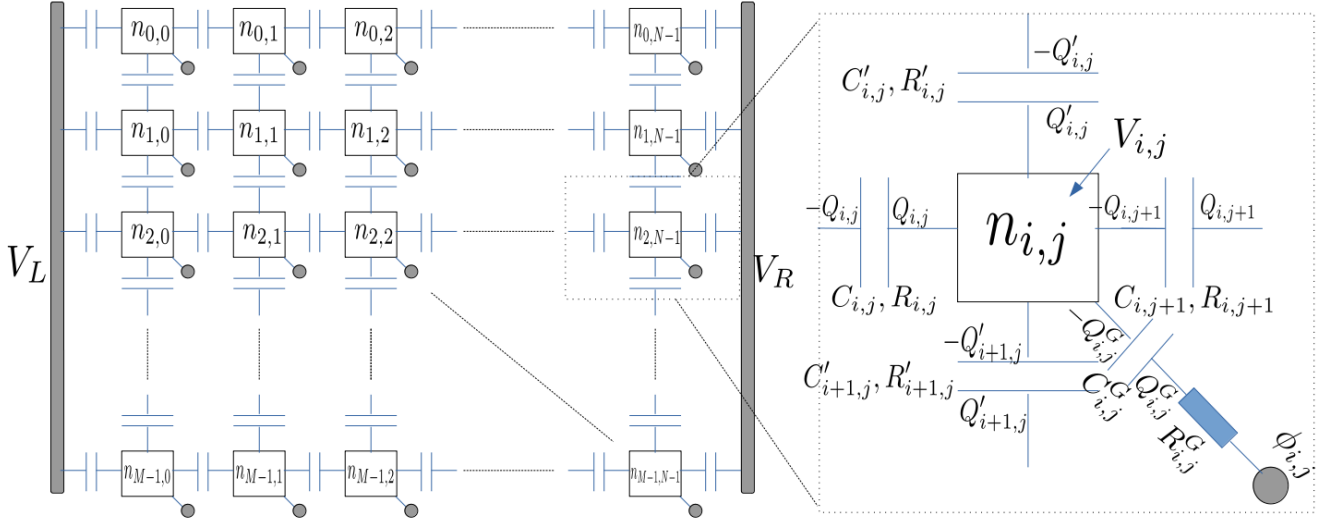


Figure 3.2: Schematic drawing of a 2D array. **left** - The array is composed of conducting islands (squares), connected by tunneling junctions. Each island is also connected to a gate voltage (gray circle). **right** - A larger view of island (i,j) , with the indexing notations used for all of its neighboring components.

array. To conveniently include boundary terms, we define

$$\begin{aligned} V_{i,-1} &= V_L, \quad V_{i,N} = V_R, \quad V_{-1,j} = V_{M,j} = 0 \\ C'_{0,j} &= C'_{M,j} = 0 \end{aligned} \tag{3.9}$$

To write this equation in a matrix form, we define the capacitance-matrix

$$C_{i,j;k,l} = \begin{cases} C_{i,j} + C_{i,j+1} + C'_{i,j} + C'_{i+1,j} & k = i, l = j \\ -C_{i,j} & k = i, l = j - 1 \\ -C_{i,j+1} & k = i, l = j + 1 \\ -C'_{i,j} & k = i - 1, l = j \\ -C'_{i+1,j} & k = i + 1, l = j \\ 0 & \text{else} \end{cases} \tag{3.10}$$

The index $(i, j; k, l)$ is used as an array size independent way of writing $(i \cdot N + j, k \cdot N + j)$. With this definition, we can write eq. 3.8 as

$$en'_{i,j} \equiv en_{i,j} + \delta_{j,0}C_{i,0}V_L + \delta_{j,N-1}C_{i,N}V_R = \sum_{k,l} C_{i,j;k,l}V_{k,l} + C_{i,j}^G(V_{i,j} - \phi'_{i,j}) \tag{3.11}$$

Using Kirchhoff's Laws, the voltage difference between an island and its gate is

$$V_{i,j} = \phi'_{i,j} - \frac{Q_{i,j}^G}{C_{i,j}^G} \tag{3.12}$$

Solving eq. 3.11, 3.12 we get

$$V_{i,j} = \sum_{k,l} C_{i,j;k,l}^{-1} (en'_{k,l} + Q_{k,l}^G) \quad (3.13)$$

Note that, if all junctions have the same capacitance, our capacitance-matrix is like the matrix from [6], with $C_G = 0$ (see chapter 2). Therefore, interactions between the total charge on island i, j , $n'_{i,j} + Q_{i,j}^G$, and charges on other islands, decay approximately as $\ln(1/r)$ (r is the unit-less distance between islands 2.8). Inserting eq. 3.13 to eq. 3.12, we get a differential equation for $Q_{i,j}^G$

$$\begin{aligned} \frac{dQ_{i,j}^G}{dt} &= - \sum_{k,l} \tau_{i,j;k,l}^{-1} (Q_{k,l}^G - Q_{k,l}^n) \\ \tau_{i,j;k,l}^{-1} &\equiv \frac{1}{R_{i,j}^G} \left(C_{i,j;k,l}^{-1} + \frac{1}{C_{i,j}^G} \delta_{i,j;k,l} \right) \\ Q_{i,j}^n &\equiv \frac{1}{R_{i,j}^G} \sum_{k,l} \tau_{i,j;k,l} \left[\phi_{k,l} + \frac{e}{C_{k,l}^G} n'_{k,l} \right] - en'_{i,j} \end{aligned} \quad (3.14)$$

where we used $\sum_{k,l} \tau_{i,j;k,l} C_{k,l;a,b}^{-1} = \delta_{i,j;a,b} - \tau_{i,j;a,b} \frac{1}{C_{a,b}^G}$. This is a system of linear ODEs. It is solvable by diagonalizing $\tau_{i,j;k,l}^{-1}$, to find its eigenvalues $\Lambda_{i,j}$ and eigenvectors matrix $P_{i,j;k,l}$ (such that $\tau_{i,j;k,l}^{-1} = P_{i,j;a,b}^{-1} \Lambda_{a,b} P_{a,b;k,l}$). The solution is given by

$$\begin{aligned} Q_{i,j}^G(t) &= \sum_{k,l} \exp(\tau^{-1}t)_{i,j;k,l} (Q_{k,l}^G(0) - Q_{k,l}^n) + Q_{i,j}^n \\ \exp(\tau^{-1}t)_{i,j;k,l} &\equiv \sum_{a,b} P_{i,j;a,b}^{-1} \exp(\Lambda_{a,b} t) P_{a,b;k,l} \end{aligned} \quad (3.15)$$

3.2.2 Energy

The electrostatic energy of the array is given by

$$\begin{aligned} E &= \frac{1}{2} \sum_{i,j} \left[\frac{(Q_{i,j})^2}{C_{i,j}} + \frac{(Q'_{i,j})^2}{C'_{i,j}} + \frac{(Q_{i,j}^G)^2}{C_{i,j}^G} \right] + \frac{1}{2} \sum_i \frac{(Q_{i,N})^2}{C_{i,N}} + Q_L V_L + Q_R V_R \\ &= \frac{1}{2} \sum_{i,j} \left[C_{i,j} (V_{i,j} - V_{i,j-1})^2 + C'_{i,j} (V_{i,j} - V_{i-1,j})^2 + C_{i,j}^G (\phi'_{i,j} - V_{i,j})^2 \right] \\ &\quad + \frac{1}{2} \sum_i C_{i,N} (V_R - V_{i,N-1})^2 + Q_L V_L + Q_R V_R \end{aligned} \quad (3.16)$$

Using eq. 3.13, we get

$$\begin{aligned} E &= \frac{1}{2} \sum_{i,j,k,l} (en'_{i,j} + Q_{i,j}^G) C_{i,j;k,l}^{-1} (en'_{k,l} + Q_{k,l}^G) - \sum_{i,k,l} (C_{i,N} C_{i,N-1;k,l}^{-1} V_R + C_{i,0} C_{i,0;k,l}^{-1} V_L) (en'_{k,l} + Q_{k,l}^G) \\ &\quad + \frac{1}{2} \sum_i (C_{i,N} V_R^2 + C_{i,0} V_L^2) + \sum_{i,j} \frac{(Q_{i,j}^G)^2}{2C_{i,j}^G} + Q_L V_L + Q_R V_R \end{aligned} \quad (3.17)$$

Now we would like to calculate the change in this energy, when a carrier tunnels from island (a, b) to (a', b') (where $(a', b') = (a \pm 1, b)$ or $(a, b \pm 1)$). The change of $n_{i,j}$ is given by:

$$\Delta n_{i,j;a,b \rightarrow a',b'} = -\delta_{i,j;a,b} + \delta_{i,j;a',b'} \quad (3.18)$$

As for the single island case, the change in electrode charges is given by that of the charge on boundary capacitors (see appendix A). We can calculate it using 3.13 and 3.18

$$\begin{aligned} \Delta Q_{a,b \rightarrow a',b'}^L &= -e \sum_i C_{i,0} \left(C_{i,0;a',b'}^{-1} - C_{i,0;a,b}^{-1} \right) + e (\delta_{a,a';0,-1} - \delta_{a,a';-1,0}) \\ \Delta Q_{i,j;a,b \rightarrow a',b'}^R &= e \sum_i C_{i,N} \left(C_{i,N-1;a',b'}^{-1} - C_{i,N-1;a,b}^{-1} \right) + e (\delta_{a,a';N-1,N} - \delta_{a,a';N,N-1}) \end{aligned} \quad (3.19)$$

The work required for this tunneling is

$$\begin{aligned} W_{a,b \rightarrow a',b'} &= e \sum_{k,l} \left(C_{a',b';k,l}^{-1} - C_{a,b;k,l}^{-1} \right) \left(e n'_{k,l} + Q_{k,l}^G \right) + \frac{e^2}{2} \left(C_{a',b';a',b'}^{-1} + C_{a,b;a,b}^{-1} - 2C_{a,b;a',b'}^{-1} \right) \\ &\quad + e (\delta_{b,b';0,-1} - \delta_{b,b';-1,0}) V_L + e (\delta_{b,b';N-1,N} - \delta_{b,b';N,N-1}) V_R \end{aligned} \quad (3.20)$$

Eq. 3.20 can be written using the voltage on each island (using the conventions from eq. 3.9)

$$W_{a,b \rightarrow a',b'} = e (V_{a',b'} - V_{a,b}) + \frac{e^2}{2} \left(C_{a',b';a',b'}^{-1} + C_{a,b;a,b}^{-1} - 2C_{a,b;a',b'}^{-1} \right) = \frac{e}{2} [(V_{a',b'} - V_{a,b}) + (V'_{a',b'} - V'_{a,b})] \quad (3.21)$$

where $V'_{i,j}$ is the electric potential on island (i, j) after the tunneling.

As for the single island case, the work is given by the average voltage difference, or by the difference before tunneling plus an energy $\frac{e^2}{2} (C_{a',b';a',b'}^{-1} + C_{a,b;a,b}^{-1} - 2C_{a,b;a',b'}^{-1})$. The tunneling rates can be calculated using this work, and eq. 2.3 or 2.5.

3.2.3 Interaction range

As seen from eq. 3.21, tunneling is effected by the local voltage difference. Island voltages depend on external voltages, and on charge distribution in the array (as can be seen in eq. 3.13). In a steady state, we can replace $Q_{i,j}^G$ in eq. 3.13 by its steady state value ($Q_{i,j}^n$ for fast relaxation or $\langle Q_{i,j}^n \rangle$ for slow, see section 3.4.2). In the case where tunneling and gate capacitance are uniform, $C_{i,j}^G = C_G$ and $R_{ij}^G = R_G$, it takes a simple form

$$V_{i,j}^n = \begin{cases} \sum_{k,l} (C_{i,j;k,l} + C_G \delta_{i,j;k,l})^{-1} (C_G \phi_{k,l} + e n'_{k,l}) & \text{fast relaxation} \\ \sum_{k,l} (C_{i,j;k,l} + C_G \delta_{i,j;k,l})^{-1} (C_G \phi_{k,l} + e \langle n'_{k,l} \rangle) + e \sum_{k,l} C_{i,j;k,l}^{-1} (n_{k,l} - \langle n_{k,l} \rangle) & \text{slow relaxation} \end{cases} \quad (3.22)$$

To get an estimation of the interaction length, we use the solution from [6] (eq. 2.8) for uniform capacitance $C_{i,j} = C$. The interaction length is given by λ . For $C_G > C$ we get $\lambda < 1.04$ (in units of the nearest neighbors distance), the interaction has a very short range. For $C_G \rightarrow 0$ we get $\lambda \rightarrow \infty$ and the interaction has a long range (the capacitance-matrix used in [6] is equal to $C_{i,j;k,l} + C_G$ in our notations). Therefore, eq. 3.22 tells us that, for fast relaxation, the interaction length depends on C_G/C . It is short

ranged for $C_G > C$. We can say that the charge on each island is screened by the gate charge. The same is true in slow relaxation, for islands that don't conduct (where $n_{i,j} = \langle n_{i,j} \rangle$). For conducting islands, there is a portion of the charge, $n_{i,j} - \langle n_{i,j} \rangle$, that is un-screened and has long range interaction length (i.e. it affects the electric potential for distant islands). We therefore expect longer interaction length for conducting islands, compared to non-conducting ones.

3.2.4 Master equation

As for the single island case, the tunneling rates would be proportional to $1/R_{i,j}$. The charge relaxation rates are given by the eigenvalues of $\tau_{i,j,k,l}^{-1}$ (eq. 3.14) which are proportional to $1/R_{i,j}^G$. The condition for slow relaxation is, therefore, $R_{i,j}^G \gg R_{k,l}$ for any i, j, k, l (and the opposite for fast relaxation). Let \mathbf{n}, Q_G be the sets of all $n_{i,j}, Q_{i,j}^G$ respectively. The master equation for occupation probabilities is given by

$$\frac{dp(\mathbf{n})}{dt} = \sum_{\tilde{\mathbf{n}} \text{ is neighbor of } \mathbf{n}} [\Gamma_{\tilde{\mathbf{n}} \rightarrow \mathbf{n}}(\tilde{\mathbf{n}}, Q_G, V) p(\tilde{\mathbf{n}}) - \Gamma_{\mathbf{n} \rightarrow \tilde{\mathbf{n}}}(\mathbf{n}, Q_G, V) p(\mathbf{n})] \quad (3.23)$$

where \mathbf{n} and $\tilde{\mathbf{n}}$ are neighbors if we can go from one to the other by one tunneling. Eq. 3.15, 3.23 are the generalizations of eq. 3.1, 3.6 and describe the charge dynamics. We now turn to describing the methods used to solve those equations.

3.3 Dynamical simulation

The numerical method we used is based on an algorithm proposed by Gillespie [24], for solving stochastic master equations. The idea behind this method is very simple. To simulate dynamics that are composed of discrete events (i.e. tunnelings), we need to know 2 things: What is the waiting time (time until next event)? What is the next event? Both questions have probabilistic answers. The probability that the next event will happen in time t (assuming an event had happened in time 0) is given by [24]

$$p_{\text{next-event}}(t) = \exp \left(- \sum_i \Gamma_i t \right) \quad (3.24)$$

The probability that next event would be event- i is proportional to Γ_i , its rate

$$p_{\text{event } i} = \frac{\Gamma_i}{\sum_i \Gamma_i} \quad (3.25)$$

Simulation starts from a chosen initial state, for a given array realization, temperature and external voltages. Waiting time and next event are chosen randomly, using eq. 3.24 and 3.25 respectively. The chosen event is then executed, and the state is updated accordingly. In the original algorithm [24], rates do not change between events, while, in our case, they do, because of their gate charge dependency. To use the algorithm for our case, we adopt a suggestion from [41]. If time until the next event is smaller than the fastest relaxation time, $\tilde{t} = \min_i [1/\Lambda_i]$, we can approximate Q_G as being constant until the next event. Therefore, we update Q_G, \mathbf{n} and the rates only after tunneling. If the chosen waiting time is bigger than \tilde{t} , we advance Q_G for time \tilde{t} , update tunneling rates, and repeat the calculation. The same thing is done if tunneling rates are all zero (happens for small external voltage and temperature).

Since we are interested in steady state properties of the array, we run the simulation in 2 steps. In the first step, simulation runs until a steady state is reached. We verify this by calculating $\langle n \rangle$ and checking that Q_G has reached the matching steady state value from eq. 3.14. In the second step, average current, occupation and gate charge are calculated. This is done by weighting the result from each step by its time, i.e. the average of x is calculated as

$$\langle x \rangle = \frac{\sum_{\text{event-}i} x_i (t_{i+1} - t_i)}{\sum_{\text{event-}i} (t_{i+1} - t_i)} \quad (3.26)$$

where t_i is the time when event i had happened, and x_i is x 's value right after the event. We thus treat Q_G as constant between events when calculating averages. This is justified because, in steady state, Q_G would be approximately constant.

To calculate array's response to changing external voltage we repeat this process for every voltage value. The initial state for each run is chosen as the final state of the former one. By increasing the voltage to a maximal value, and then decreasing it back again, we can check if hysteresis occurs. In the same way we can simulate the array response to different temperatures.

The big advantage of this method lies in its variability. It works for any array realization or tunneling rates, as long as the dynamics are described by eq. 3.15 and 3.23. In addition, it samples the steady state without the need of sampling the whole configuration space of the system. A main computational cost goes to updating the required work (for future tunnelings) after each tunneling. This is done using eq. 3.20 and thus involves multiplication of $NM \times NM$ matrix by NM sized vector. Since we are interested in the slow relaxation limit (this is when hysteresis is predicted by the single island model, see chapter 4), the simulation would require many steps for converging to steady state. The convergence time would become longer as tunneling rates increase, since then more events would happen until Q_G relaxes. The same is true for big arrays, where there are more possible events, and thus the time between consecutive tunnelings would be shorter, compared to small arrays.

3.4 Solution using a graph, for $T = 0$

There is another way to find a steady state solution for eq. 3.14 and 3.23, in the $T = 0$ case. It depends on the relation between inter-tunneling and relaxation time scales. For $R_{i,j}^G \ll R_{i,j}$ relaxation is much shorter than inter-tunneling. Therefore, we can replace Q_G by Q_n in eq. 3.23. For $R_i \ll R_G$, relaxation time is much slower than inter-tunneling time. In this case we can treat Q_G in eq. 3.23 as a constant. In either case, we can solve eq. 3.23 to find a steady state probability. For slow relaxation, it would be Q_G dependent, $p_{Q_G}(n, V)$. Given this probability, eq. 3.14 would take the form

$$\frac{dQ_{i,j}^G}{dt} = - \sum_{n,k,l} p_{Q_G}(n, V) \tau_{i,j,k,l}^{-1} (Q_{k,l}^G - Q_{k,l}^n) \quad (3.27)$$

3.4.1 Master equation solution

For $T = 0$, the number of possible states is finite (since we can only get to those with lower energy than the current one). It is convenient to treat the possible occupation states as vertices of a directed graph. Two states would be connected by an edge if they are neighbors (can get from first to second by

tunneling). The weight of each edge would be the rate of tunneling between the states it connects. To build the graph, we use Breath First Search (BFT) algorithm. Starting from the initial vertex (state), we calculate the tunneling rates to its neighboring states. We then add edges and vertices accordingly. This process is repeated for each new vertex. We save a vector of vertices and an adjacency matrix, where $\Gamma_{i,j}$ is the weight of an edge from vertex i to j . The graph is finished when we have no more vertices to add. Eq. 3.6 can be written using the adjacency matrix as

$$\frac{dp_j}{dt} = \sum_i p_i \tilde{\Gamma}_{i,j} \quad (3.28)$$

$$\tilde{\Gamma}_{i,j} \equiv \Gamma_{i,j} - \delta_{i,j} \sum_k \Gamma_{j,k}$$

where p_i is the probability of finding the system with occupation state n_i . Adding the condition $\sum_i p_i = 1$, we get a system of linear equations with one more equation than variables. We can find a solution using numerical methods (e.g. least squares). An example for a graph representation of eq. 3.23 is shown in fig. 3.3. For $T = 0$, all edges are one directional, since only transitions to a lower energy state are possible. For finite T transitions in the opposite direction (low to high energy) are possible, but they are smaller by a factor of $e^{-|\Delta E|/k_B T}$. For $V = 0, T = 0$ there are no cycles in the graph. System will then converge to the lowest energy state, and no current would flow. When increasing V , cycles start to form. Each cycle represents a chain of events in which a charge of one carrier passes through the array. Transition rates and steady state probabilities, in each cycle, will determine its contribution to the current. Increasing V further more, we will get cycles in which a charge of $n > 1$ carriers passes through the array.

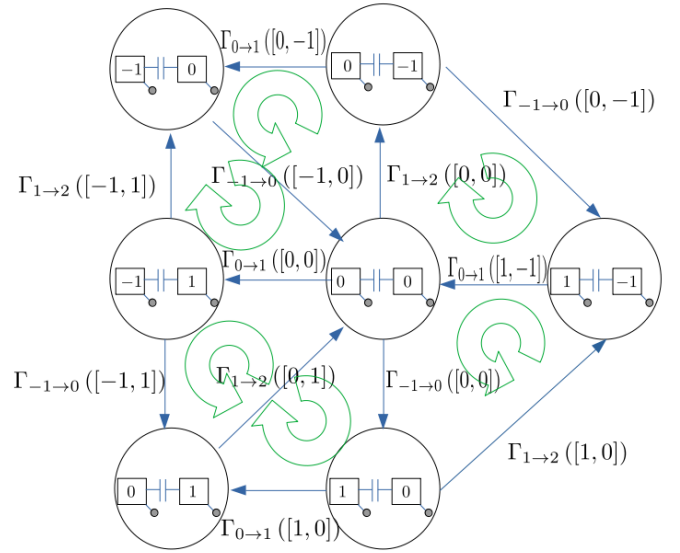


Figure 3.3: Master equation graph representation. For an array with 2 islands, uniform capacitance and external voltage just above threshold. Each vertex represents an occupation state. The weight of each edge is the tunneling rate between the states it connects. Edges directions mark the possible transitions for $T = 0$. Green arrows mark cycles, in which one charge unit passes from left to right.

3.4.2 Steady state gate charge for slow relaxation

Solving for the steady state probability, we can calculate

$$\langle Q_n \rangle_{Q_G} = \sum_n Q_n p(n)_{Q_G} \quad (3.29)$$

and we are left with the task of finding a steady state solution for eq. 3.14. This can be done using the Lyapunov functional method. A Lyapunov functional $L(Q_G)$ is a functional that is monotonically

decreasing with time. The easiest way to define such a functional is by finding L such that

$$\text{sign} \left(\frac{\partial L(\mathbf{Q}_G)}{\partial Q_{i,j}^G} \right) = -\text{sign} \left(\frac{dQ_{i,j}^G}{dt} \right) \quad (3.30)$$

which implies

$$\frac{dL(\mathbf{Q}_G)}{dt} = \sum_{i,j} \frac{dL(\mathbf{Q}_G)}{dQ_{i,j}^G} \frac{dQ_{i,j}^G}{dt} < 0 \quad (3.31)$$

Being a monotonically decreasing function of time, implies that a minimum of the Lyapunov functional is a stable steady state solution, while a maximum of it is not stable. In our case we define a Lyapunov functional by

$$L(\mathbf{Q}_G) = \sum_{i,j} \int_{Q_{min}}^{Q_{i,j}^G} \left(Q - \langle Q_{i,j}^n \rangle_{\mathbf{Q}_G|Q_{i,j}^G \rightarrow Q} \right) dQ \quad (3.32)$$

where $\mathbf{Q}_G|Q_{i,j}^G \rightarrow Q$ means replacing the value of $Q_{i,j}^G$ by Q . Q_{min} is an arbitrary value, smaller than the values of Q_G that we are interested in. The time derivative of L is

$$\sum_{i,j} \frac{\partial L(\mathbf{Q}_G)}{\partial Q_{i,j}^G} \frac{dQ_{i,j}^G}{dt} = - \sum_{i,j,k,l} \left(Q_{i,j}^G - \langle Q_{i,j}^n \rangle_{Q^G} \right) \tau_{i,j;k,l}^{-1} \left(Q_{k,l}^G - \langle Q_{k,l}^n \rangle_{Q^G} \right) < 0 \quad (3.33)$$

The last inequality follows from the fact that all the eigenvalues of τ^{-1} are positive (see eq. 3.14). Our approach to finding the steady-state solution for \mathbf{Q}_G is to use gradient descent to find a minimum of L . In fact, we don't need to calculate L explicitly, since we only need its gradient (eq. 3.30).

This method gives us an alternative way for finding the steady state probability of the system. For a single island, the master equation and the Lyapunov functional are relatively simple, so we can use this method to better understand the dynamics of the single island model. We can also use this method to verify the dynamical simulations by comparing results. In principle, we could use this method for any array size, but practically, the computational resources required grow exponentially with array size (the number of possible states is exponential in the number of islands). Therefore, we use this method only for very small arrays.

3.5 Disorder realization

To find the transport properties of an array we need to specify the value for all capacitance $C_{i,j}, C'_{i,j}, C_{i,j}^G$, resistance $R_{i,j}, R'_{i,j}, R_{i,j}^G$ and gate voltages $\phi_{i,j}$. In principle, changing each of those might effect the transport properties. We use random realizations, where we specify a separate distribution for each class of parameters: capacitance, gate-capacitance, resistance and gate-resistance. The specific realization is then chosen randomly from the given distributions. Standard deviations of the distributions are referred to as model disorder.

We have implemented both methods in Python. The code is publicly available at https://github.com/kasirershaharbgu/random_2D_tunneling_arrays.

Chapter 4

Results

To understand the transport properties of our model, we start from the single island case. The detailed solution is given in appendix A. Here we would only give its outline, focusing on hysteresis and jumps. This would help us to gain intuition that we can later use, when analyzing the numerical results for 2D arrays.

4.1 Single island

In the single island case, the graph representation of the master equation (eq. 3.6) takes a simple form (for example see fig. 4.1). For given Q_G and V , one can find the steady state solution using the following procedure. First, an initial probability is assigned to an edge vertex (e.g. $n = \pm 2$ in fig. 4.1). Then other probabilities are calculated, using eq. 3.6. Finally, the probabilities are normalized to satisfy $\sum_n p(n) = 1$. Having calculated the steady state probability, we can calculate the current using eq. 3.7 (see appendix A)

$$I \frac{(R_1 + R_2)(C_1 + C_2)}{e} = V \frac{C_1 + C_2}{e} - 1 + \frac{C_1 + C_2}{e^2} [p_{n_{max}} W_{n_{max}}^+ + p_{n_{min}} W_{n_{min}}^-] \quad (4.1)$$

where W_n^\pm is the work required to add (+) or remove(-) one carrier to an island with occupation n .

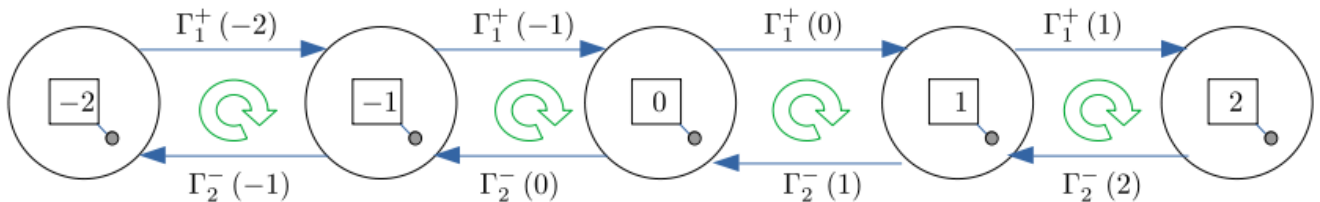


Figure 4.1: Single island master equation graph representation. Calculated for $C_1 = C_2, \phi = 0$ and small external voltage. Each vertex represents an occupation state (number of excess carriers on the island). The edges connect neighboring states. The weight of each state is the corresponding tunneling rate. Green arrows show cycles for which 1 charge unit passes from left to right.

4.1.1 Conditions for hysteresis and jumps

The resulting current depends on the relation between inter-tunneling and relaxation time scales (see chapter 3). For fast relaxation, the master equation has a unique steady-state solution (for a given V , see appendix A). This means that I is uniquely defined by V and there is no hysteresis in the I-V curve.

For slow relaxation, Q_G will relax to its mean equilibrium value and eq. 3.1 would take the form

$$\begin{aligned} Q_G(n, t) &= \left(Q_0 - \langle Q_n \rangle_{Q_G} \right) e^{-\frac{t}{\tau}} + \langle Q_n \rangle_{Q_G} \\ \langle Q_n \rangle_{Q_G} &\equiv \sum_n p_{Q_G}(n, V) Q_n(V) \end{aligned} \quad (4.2)$$

The steady state solution for Q_G would satisfy

$$Q_G = \langle Q_n \rangle_{Q_G} = \frac{C_G}{C_\Sigma} \left((C_1 + C_2) \phi - C_1 V_L - C_2 V_R - \langle n \rangle_{Q_G} e \right) \quad (4.3)$$

where $\langle n \rangle_{Q_G} \equiv \sum_n n p_{Q_G}(n)$. This equation can have multiple solutions for a given V . In that case, it is possible to get hysteresis in the I-V curve. To understand the conditions for hysteresis, we write eq. 4.3 in terms of island's potential. Using eq. 3.3 we get

$$\langle U \rangle_{Q_G} = \phi - \frac{Q_G}{C_G} \quad (4.4)$$

This is the same as requiring that, for a steady state, the average current through R_G would vanish. Notice that, since tunneling rates (eq. 3.4) depend only on $Q_G + ne$, increasing Q_G by e and decreasing n by 1 would leave the master equation (eq. 3.6) unchanged. This means that $p_{Q_G+e}(n) = p_{Q_G}(n+1)$, and therefore $\langle n \rangle_{Q_G+e} = \langle n \rangle_{Q_G} - 1$. Since $\langle U \rangle_{Q_G}$ is a function of $Q_G + ne$, it is periodic in Q_G , with a period e , $\langle U \rangle_{Q_G+e} = \langle U \rangle_{Q_G}$.

Finding $\langle U \rangle_{Q_G}$ requires solving the master equation 3.6, this can be done explicitly for $T = 0$, although the exact solution is quite cumbersome. The solution is derived in appendix A and plotted in fig. 4.2 along with the linear function $\phi - \frac{Q_G}{C_G}$. Hysteresis is possible if eq. 4.4 can have more than one solution, the condition for that is

$$C_G > \left(\max_{Q_G} \left[-\frac{\partial \langle U \rangle_{Q_G}}{\partial Q_G} \right] \right)^{-1} \quad (4.5)$$

since otherwise the linear function $\phi - \frac{Q_G}{C_G}$ (purple curves in fig. 4.2) decreases faster than $\langle U \rangle_{Q_G}$ anywhere, and thus crosses it only once (e.g. green curves in fig. 4.2). Analysis of $\langle U \rangle_{Q_G}$ for small voltages, such that only 2 states are possible, shows (appendix A) that we will get hysteresis for

$$C_G > (C_1 + C_2) \left[\frac{1}{1 - \frac{R_{min}}{R_{max}} \frac{(C_1 + C_2)V}{e}} - 1 \right] \quad (4.6)$$

We can rewrite this, to get a condition for V :

$$V \frac{C_1 + C_2}{e} < V^{hyst} \frac{C_1 + C_2}{e} \equiv \frac{R_{max}}{R_{min}} \frac{C_G}{C_\Sigma} \quad (4.7)$$

As seen in fig. 4.2a, for small V (blue curve), we have more than one steady state solution. For larger V (orange curve) there is only one solution. For even larger V (green curve), more states become available (more carriers can tunnel to, or from, the island) and $\langle U \rangle_{Q_G}$ becomes, approximately, Q_G independent. This convergence is slower when the ratio R_{max}/R_{min} is bigger, as shown in fig. 4.2b. For $R_1 = R_2$ (orange curve), $\langle U \rangle_{Q_G}$ is almost Q_G independent for $V = 2 \frac{e}{C_1 + C_2}$. For $R_2 > R_1$, and the same

voltage (green and red curves), $\langle U \rangle_{Q_G}$ becomes more similar to the result for low voltages (blue curve in fig. 4.2a). Therefore, we will see a more pronounced hysteresis for small voltages and large resistance ratio. For very high voltage, such that $p_{n_{max}}$ and $p_{n_{min}}$ become negligible, I-V curve becomes Ohmic, $I \approx V / (R_1 + R_2)$.

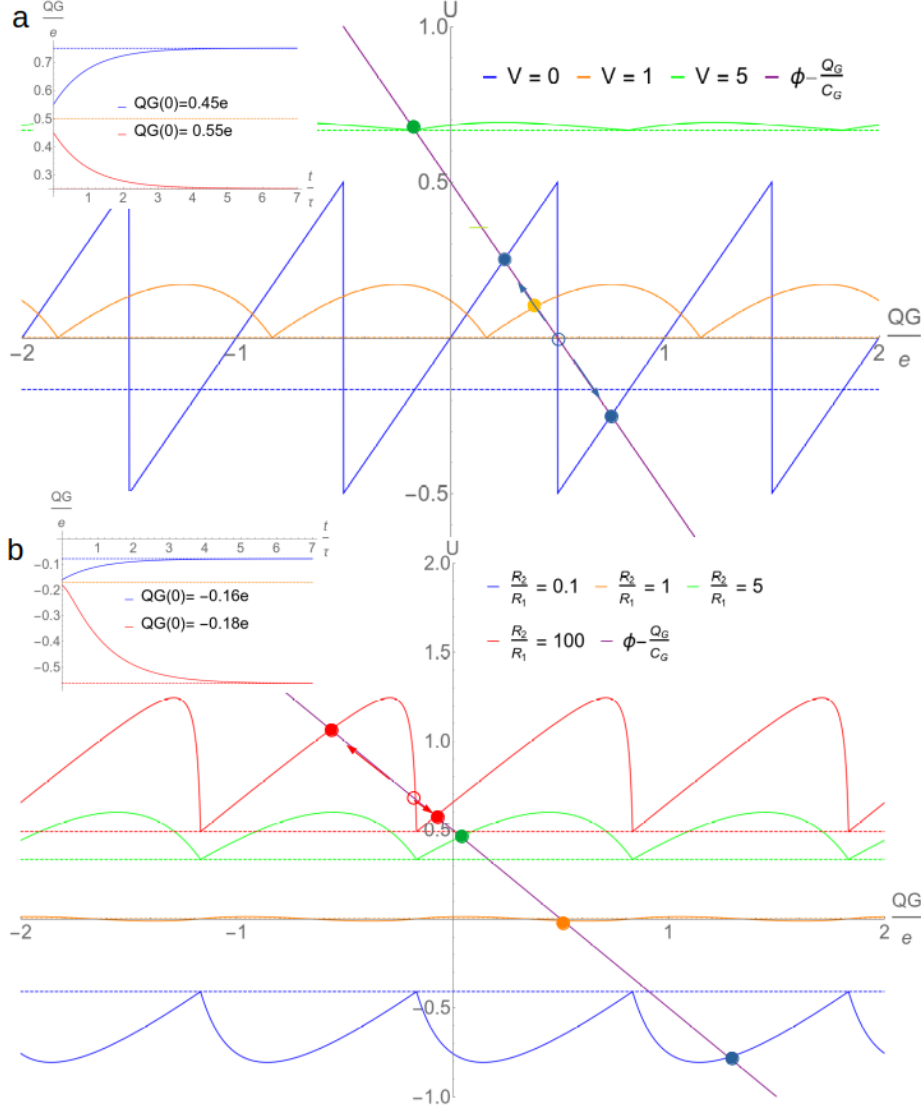


Figure 4.2: Average voltage on island for different external voltages (a) and resistances (b). Stable steady state solutions are marked with a whole circle, unstable with an empty circle. Dashed line - Approximated Q_G independent solutions (see appendix A). Small arrows indicate direction of convergence for bi-stable cases ($V = 0$ in (a) and $R_2/R_1 = 100$ in (b)). Voltages are measured in units of $\frac{e}{C_1+C_2}$. (a) For $V = 0$, the shape is saw-tooth like. For large V , average U approaches the Q_G independent solution. (b) As resistances ratio, R_2/R_1 , increases, $\langle U \rangle_{Q_G}$ shape resembles the $V = 0$ result. For $R_1 > R_2$ the result is mirrored about the x -axis. **Insets** - Q_G for bi-stable cases, as a function of time, for different initial values. Dashed lines mark the steady state solutions (red and blue - stable, orange - unstable). **Mutual parameters:** $C_2 = 2C_1$, $C_G = C_1 + C_2$, $V_L = -V_R = V/2$, $\phi = 0.5\frac{e}{C_1+C_2}$. (a) $R_2 = 2R_1$. (b) $V = 2\frac{e}{C_1+C_2}$.

4.1.2 Hysteresis and jumps size

When increasing the voltage, new occupation states become available. Each new state starts with zero probability, that gradually increases with voltage (see eq. A.20). Therefore, the current would be a continuous function of Q_G and jumps occur only when Q_G jumps. This means that in the fast relaxation case there are no jumps. For slow relaxation, jumps and hysteresis only appear together.

For $R_2 > R_1$ ($R_1 > R_2$) an upward jump will occur every time that the steady state solution gives the minimal(maximal) value of $\langle U \rangle_{Q_G}$. A downward jump will occur when $\frac{\partial \langle U \rangle_{Q_G}}{\partial Q_G} = -\frac{1}{C_G}$ (for example see fig. 4.2b, red curve). Jumps height (ΔI), the separation between jumps in the same direction (ΔV), and between upwards and downwards jumps ($\Delta V_{\uparrow\downarrow}$), can be estimated for $R_{\max}/R_{\min} \gg 1$ and small voltages. For the case where voltage increases symmetrically ($V_R = -V_L = V/2$), this approximation

yields (see detailed derivation and comparison to numerical results in appendix A)

$$\Delta V \approx \begin{cases} \frac{e}{\frac{C_G}{2} \frac{R_2 - R_1}{R_1 + R_2} + C_2} & R_2 > R_1 \\ \frac{e}{\frac{C_G}{2} \frac{R_1 - R_2}{R_1 + R_2} + C_1} & R_1 > R_2 \end{cases}$$

$$\Delta V_{\uparrow\downarrow}(V_{\downarrow}) \approx \Delta V \times \begin{cases} \frac{C_G}{R_2 - R_1} \left[\frac{eR_2}{C_1 + C_2} + R_1 V_{\downarrow} - \sqrt{\frac{eR_1 R_2 V_{\downarrow} (C_1 + C_2 + 2C_G)}{(C_1 + C_2) C_G C_{\Sigma}}} \right] & R_2 > R_1 \\ \frac{C_G}{R_1 - R_2} \left[\frac{eR_1}{C_1 + C_2} + R_2 V_{\downarrow} - \sqrt{\frac{eR_1 R_2 V_{\downarrow} (C_1 + C_2 + 2C_G)}{(C_1 + C_2) C_G C_{\Sigma}}} \right] & R_1 > R_2 \end{cases}$$

$$\Delta I \approx \frac{e}{C_{\Sigma} (R_1 + R_2)}$$
(4.8)

where V_{\downarrow} (in $\Delta V_{\uparrow\downarrow}$) is the voltage in which the downwards jump had occurred. When $\Delta V \leq \Delta V_{\uparrow\downarrow}$ there will be one big hysteresis loop (see fig. 4.3a). When $\Delta V > \Delta V_{\uparrow\downarrow}$ we will get few loops (see fig. 4.3b), one for each upwards jump. In that case, the area of each loop can be approximated by

$$A(V_{\downarrow}) \approx \Delta I \Delta V_{\uparrow\downarrow}(V_{\downarrow}) \quad (4.9)$$

Increasing C_G , we will see more jumps in the I-V curve, each jump would be smaller, and the separation between consecutive jumps will decrease. At the same time, the up-down separation will increase.

The results for single island I-V curves, calculated for various parameter values using both methods from chapter 3, are plotted in fig. 4.3. We can see a good agreement between both methods for $T = 0$. As the analysis predicts, we get visible hysteresis and jumps only for big resistance ratios and small voltages. Notice fig. 4.3b, where the I-V is continuous, although there is a steep slope when conduction starts. This is a result of the steep slope of $\langle U \rangle_{Q_G}$ for $R_2 \gg R_1$ (see fig. 4.2b), and can be mistakenly identified as jumps in numerical or experimental results. Hysteresis loop area becomes bigger when C_G increases. As temperature increase, the area of each hysteresis loop becomes smaller, and the I-V curves become smoother. It is encouraging to note that these results qualitatively resemble the observed ones, for a single quantum dot[17].

4.1.3 Threshold voltage

Current flows through the island whenever steady state probability allows for more than one possible occupation. For $T = 0$, we can find the threshold voltage by looking for the minimal V , for which maximal island occupation exceeds its minimal value. The threshold voltage is bounded from below by the voltage in which minimal and maximal occupation are equal, for any Q_G , $V_{min}^{th} = \frac{e}{C_1 + C_2} \frac{C_G}{C_{\Sigma}}$. For fast relaxation, maximal and minimal occupations depend only on constant parameters (see A.14) and therefore threshold can be easily calculated. For $V_R = -V_L = V/2$ we get (see A.56)

$$V^{th} = \min \left[\frac{q^+}{C_2 + C_G/2}, \frac{q^-}{C_1 + C_G/2} \right]$$

$$q^{\pm} \equiv \pm (\phi C_G + e n_{ini}) + e \frac{C_{\Sigma}}{2(C_1 + C_2)}$$
(4.10)

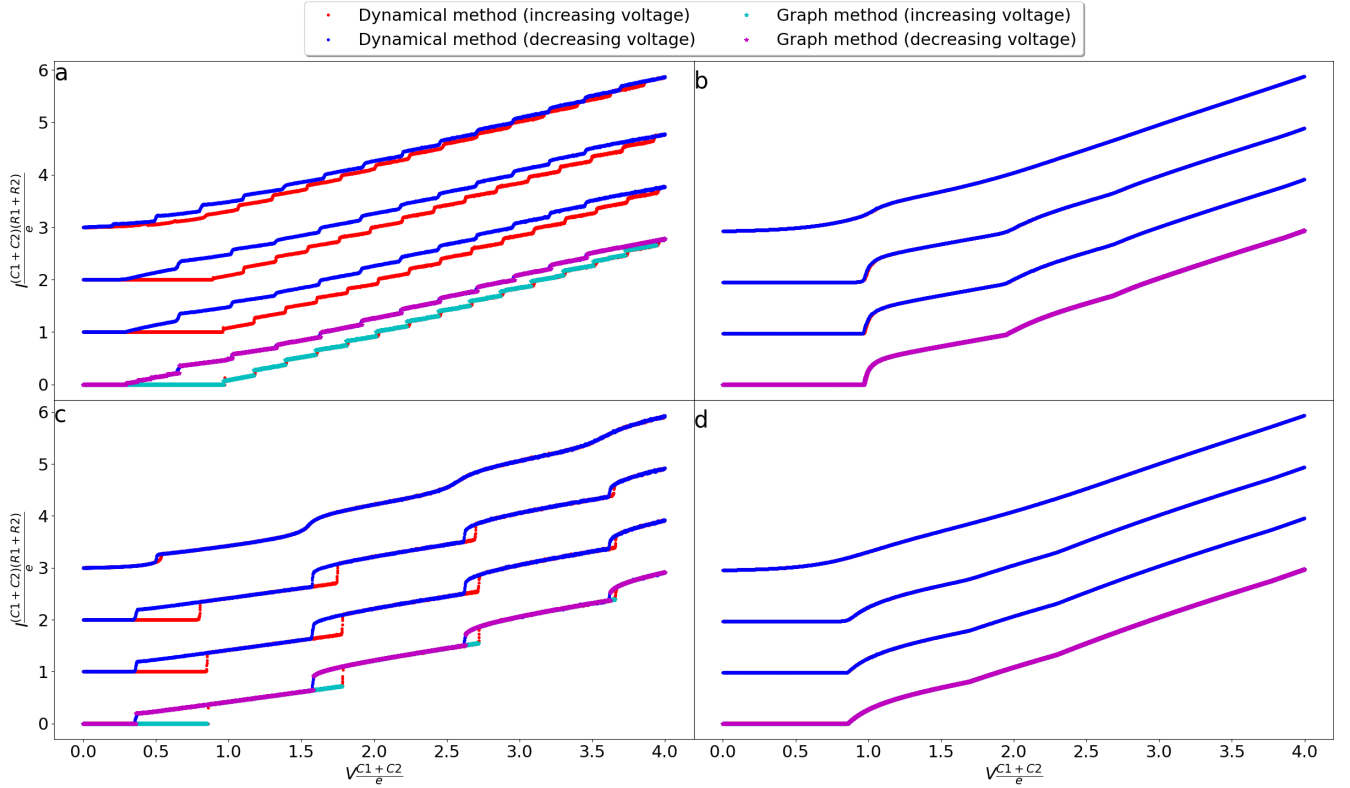


Figure 4.3: Single island I-V curves. Solved using graph method for $T = 0$ and dynamical method for $k_B T \frac{C_1 + C_2}{e^2} = 0, 0.001, 0.01, 0.1$. Curves are ordered from low to high temperature and shifted up by 1 with respect to each other. (a) For large gate capacitance, $C_G = 10(C_1 + C_2)$ and resistance ratio $R_2/R_1 = 10$ we get a single large hysteresis loop, composed of multiple steps. The loop becomes smaller as temperature rises. (b) For large gate capacitance $C_G = 10(C_1 + C_2)$ and small resistance ratio $R_2/R_1 = 1$, we see no hysteresis or jumps. We do see steep, continuous, rise of I around $V \frac{C_1 + C_2}{e} \sim 1$. (c) For small gate capacitance $C_G = C_1 + C_2$ and large resistance ratio $R_2/R_1 = 10$ we see multiple hysteresis loops, one for each current jump. When temperature rises, loops shrink and, eventually, disappear. (d) For small gate capacitance $C_G = C_1 + C_2$ and resistance ratio $R_2/R_1 = 1$ there is no hysteresis nor jumps. As temperature rises all curves become smoother. In all plots there is an agreement between the results of both methods for $T = 0$.

Common parameters: $C_2/C_1 = 2, \phi = 0, R_G = 1000(R_1 + R_2)$.

where n_{ini} is the occupation for $V = V_{min}^{th}$. Notice that threshold depends on the maximal tunneling capacitance, and thus will decrease as C_{max}/C_{min} increases.

For slow relaxation, things are more complicated, since maximal and minimal occupations depend on Q_G . Initial occupation would be determined by the initial gate charge (see eq. A.13). Using this value as n_{ini} in eq. 4.10 we find the voltage for which occupation changes. But, unlike fast relaxation, conduction won't necessarily start for this V . If hysteresis condition 4.6 is not satisfied, Q_G will change continuously and the result for fast relaxation threshold voltage would still be valid. In this case, current will start raising continuously at $V = V^{th}$. If condition 4.6 is satisfied, there are two possible cases: (1) The jump in Q_G brings us to a conducting state; (2) The jump changes both minimal and maximal occupation together, leaving the system in a non-conducting state. The latter case will happen for large gate capacitance. The exact condition can be calculated using the small voltage approximation (see eq.

A.42)

$$C_G > (C_1 + C_2) \left[\frac{e}{(C_1 + C_2) V} - 1 \right]^{-1} \quad (4.11)$$

To calculate the threshold voltage if 4.11 holds, we need to follow an iterative process. Starting from initial conditions, we first determine if the threshold voltage calculated using 4.10 happens before or together with a Q_G jump. If both happen together, we use equation 4.11 to determine if conduction starts. If not, we update our initial conditions and repeat the calculation. Threshold voltage for slow relaxation can be equal to, or greater than, threshold for fast relaxation.

In any case, threshold voltage is bounded from below by $V_{min}^{th} = \frac{e}{C_1+C_2} \frac{C_G}{C_\Sigma}$, and from above by the voltage for which maximal occupation value exceeds its minimal value for any Q_G , $V_{max}^{th} = \frac{e}{C_1+C_2}$. To get hysteresis and jumps, V^{th} must be smaller than V^{hyst} (eq. 4.7). Comparing V^{hyst} to V_{min}^{th} , we get the condition $R_{max} > R_{min}$. Therefore, hysteresis in a single island is not possible for $T = 0$ without tunneling resistance anisotropy.

In fig. 4.3 we can see examples of 2 possible cases for threshold voltage. In fig. 4.3a,c condition 4.6 holds for V^{th} , and conduction start with a jump. In fig. 4.3b,d, condition 4.6 does not hold, and conduction starts gradually.

4.1.4 Arrhenius law

Lastly we would like to check if the single island model satisfies Arrhenius law. Resistance as a function of inverse temperature, for different voltage is plotted in fig. 4.4. For $V < V^{th}$, when $T \rightarrow 0$ resistance diverges faster than Arrhenius law. The reason for this early divergence is the finite energy barrier needed for tunneling (eq. 3.2). For $V \sim V^{th}$ the energy barrier gets smaller. The result for small C_G and R ratio fits Arrhenius law very well. When increasing C_G or R ratio, jumps in Q_G becomes possible, causing a deviation from Arrhenius law. Finally, for $V > V^{th}$, the system is in its metallic phase and R doesn't diverge at $T \rightarrow 0$. In this case we used a modified Arrhenius law, $R^{-1} = (R_\infty^{-1} - R_0^{-1}) e^{-T_0/T} + R_0^{-1}$, to allow for the finite $T = 0$ resistance. The modified law fits the data well. Notice that here we get jumps also for $R_1 = R_2$. This is not a contradiction to the former result, since V^{th} is lower for finite T than it is for $T = 0$.

4.1.5 Summary

To summarize, an analysis of the single island model reveals that hysteresis and jumps in the I-V curve are not possible for fast relaxation. For slow relaxation, our results show that

1. The condition for measuring hysteresis and jumps in the I-V curve is approximately given by $V^{th} \frac{C_1+C_2}{e} < \frac{R_{max}}{R_{min}} \frac{C_G}{C_\Sigma}$. For this condition to be satisfied in zero temperature, resistance anisotropy is required.
2. Increasing resistance anisotropy would increase the voltage for which hysteresis and jumps are measured, and decrease the separation between jumps. Therefore, we will measure more jumps for larger resistance anisotropy.
3. Increasing capacitance anisotropy (C_{max}/C_{min}) main effect would be to decrease the separation between jumps.

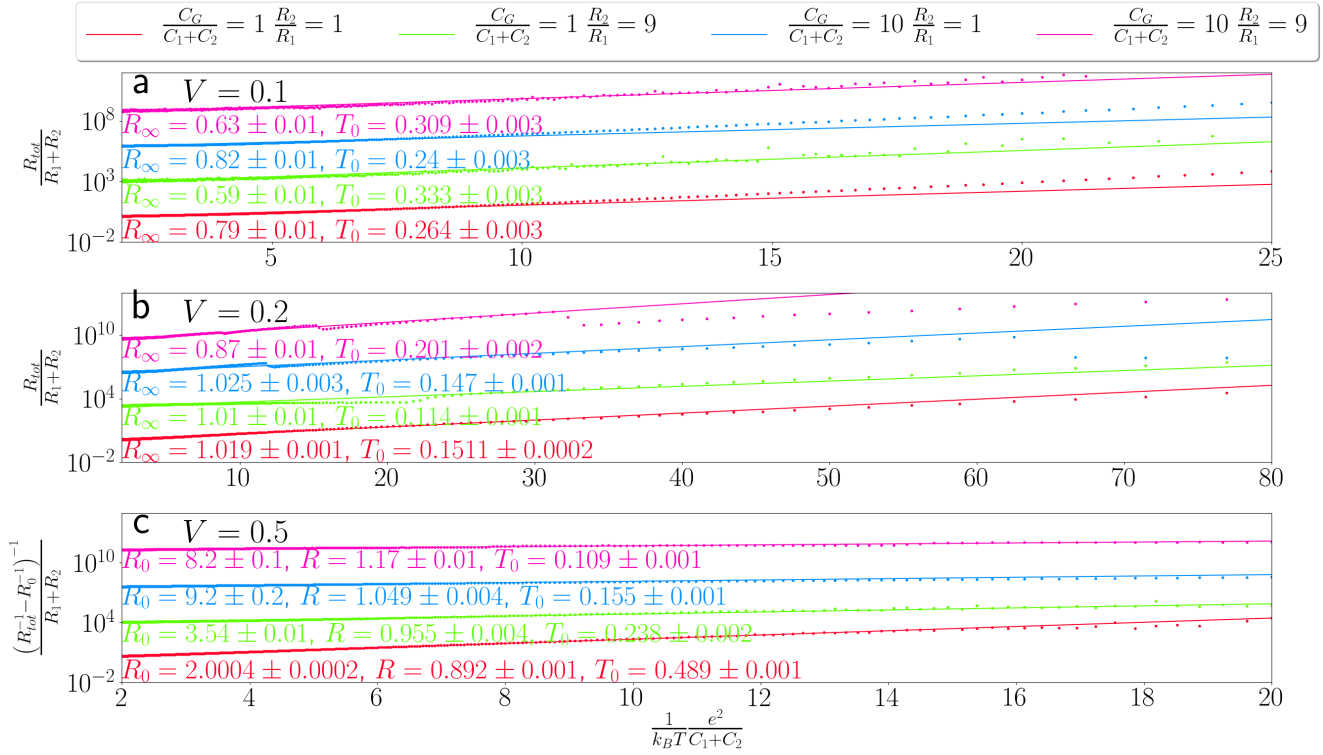


Figure 4.4: Single island R-T curves. R as a function of $1/T$ For different parameters (dots) fitted to Arrhenius law $R = R_\infty e^{T_0/T}$ (continuous curves). Fit parameters are written under each curve. Resistance, temperature and voltage are measured in units of $R_1 + R_2$, $\frac{e^2}{C_1+C_2}$ and $eC_1 + C_2$ respectively. (a) V below threshold. Arrhenius law fits the results well for higher T values but does not match the result for low T . Curves are shifted by $8 \cdot 10^2$ from each other. (b) V near threshold. For low C_G and $R_2/R_1 = 1$ Arrhenius law fits the results very well. For the rest of curves current jumps happens and fits deviates from results. Curves are shifted by $15 \cdot 10^2$ from each other. (c) V above threshold. Resistance converge for $T \rightarrow 0$ and the fit is to a modified Arrhenius law, $R^{-1} = (R_\infty^{-1} - R_0^{-1}) e^{-T_0/T} + R_0^{-1}$. Fits are in good agreement with results. Curves are shifted by $5 \cdot 10^3$ from each other.

Common parameters: $C_2/C_1 = 1, \phi = 0, R_G = 1000 (R_1 + R_2)$

4. Increasing the gate capacitance would cause an increase in hysteresis loop area, and a decrease in the separation and height of jumps.

As for Arrhenius law, when there are no jumps, our simulation results are in good agreement with it, near threshold voltage. Above threshold there is a good agreement with the modified law. As resistance disorder and C_G increase, jumps start to appear, and our results deviate from Arrhenius law.

4.2 Arrays

With results for the single island model in hand, we have a basic understanding of the model. We can now turn to present our numerical results for arrays. We will focus on slow relaxation limit, in which we expect to get hysteresis and jumps.

Different islands in an array do not operate independently, due to interactions between carriers located on different islands. We will start by examining the effect these interactions have on the I-V curve. Then, we will move to examining the influence of changing different parameters in our model.

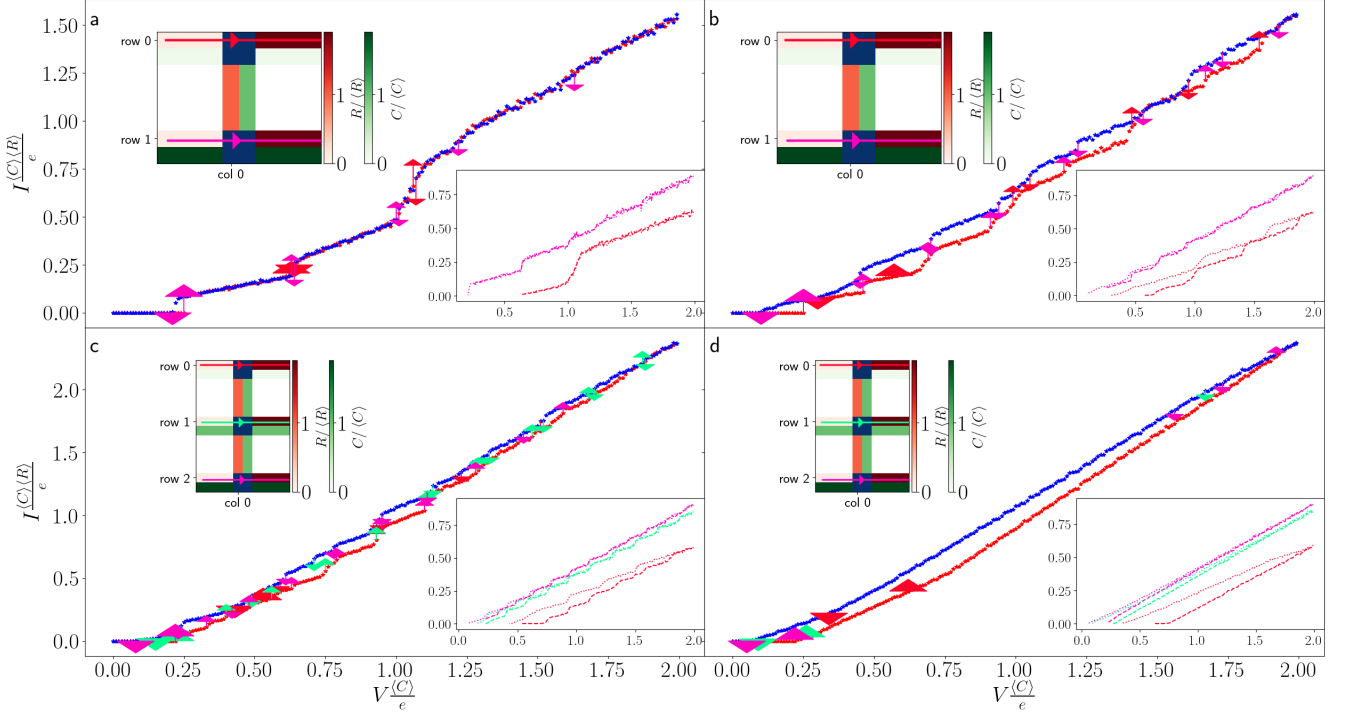


Figure 4.5: Jumps and hysteresis for single column arrays. In an array, current can flow through multiple paths. When a current jump occurs in one of them, it may also be measured as a jump in the general I-V curve. **Main figures:** I-V curves. Red - increasing voltage, blue- decreasing voltage. Small arrows indicate current jumps in different paths. Bigger arrows indicate path openings. Each path has its color, which is used also for insets. **Upper inset:** Resistance (red) and capacitance (green) of tunneling junctions. Each path is marked with its color. **Lower insets:** Current on each path, plotted using its color. Dashed line - increasing voltage, dotted line -decreasing voltage. (a) For 2X1 array with $C_G/\langle C \rangle = 1$, we see significant hysteresis and jumps only for small voltages. Their origin is the current flowing through the lower island (pink path), as seen in the lower inset. (b) Same array as in (a) with $C_G/\langle C \rangle = 5$. The current through lower island (in pink) shows many jumps and small hysteresis loops. The current through upper island (in red) shows loops with larger areas. (c) For 3X1 array with $C_G/\langle C \rangle = 10$, we see a similar pattern. Hysteresis loop is larger for paths with smaller tunneling capacitance. Jumps are bigger and more frequent for paths with larger tunneling capacitance. (d) Same array as in (c) with $C_G/\langle C \rangle = 50$. Jumps become too small to detect and we get one big hysteresis loop. Hysteresis loop area is still bigger for the lowest tunneling capacitance path (in red). **Common parameters:** $\phi = 0$, $R_G = 100 \langle R \rangle$, $R_{max}/R_{min} = 19$, $C_{max}/C_{min} = 19$.

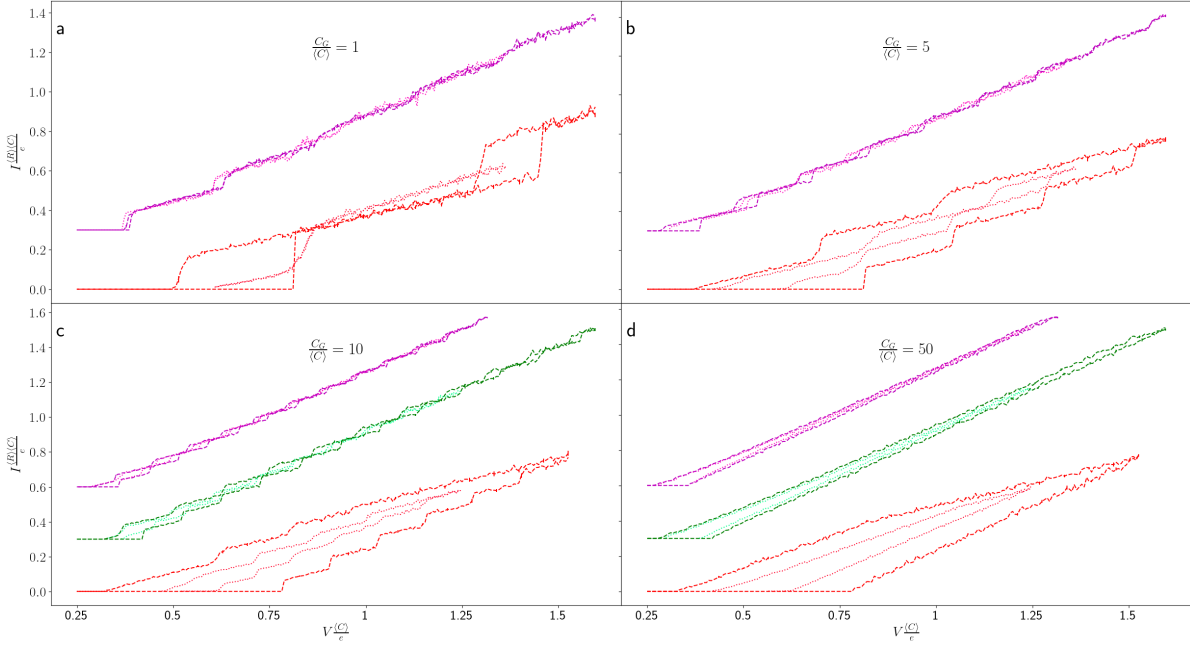


Figure 4.6: Comparison between single island and single column array. Dotted lines - current through each path for the same arrays as in fig. 4.5. Dashed lines- current through single islands with the same parameters (same self-capacitance and same resistance). Curves are shifted up by 0.3 from each other. Hysteresis loop areas are bigger for single islands. Discrepancy between results is larger for paths with bigger self capacitance, and for smaller $C_G / \langle C \rangle$.

4.2.1 Interactions between different paths

An array will conduct when it is in a steady state that enables carriers to tunnel from one electrode to the other. For 2D array, carriers can sometimes do so by more than one path. Hysteresis and jumps, in the current flowing through each path, occur when jumps in Q_G occur in one or more of its islands. If this path holds a large percentage of the total current, this jump would be apparent in the general I-V curve.

To examine the interactions between different paths, we start by looking at a simple case, arrays with a single column. In fig. 4.5, I-V curves for 2X1 and 3X1 arrays are plotted, along with the current for each path. We can see that current flows mostly through the shortest paths (directly from left to right). The current through individual paths acts in a similar way, qualitatively, to the current in the single island case. Paths with larger $C_G / \langle C \rangle$ show bigger hysteresis loop area, smaller jumps separation and smaller height. In addition, the threshold voltage is smaller for paths with bigger capacitance. Paths open in order, from big to small capacitance.

Fig. 4.6 compares the current through each path (for the same arrays as in 4.5) to the current through the matching single island, i.e. one with the same effective self capacitance ($C_{i,j,i,j}^{-1}$, see appendix B), and tunneling resistance. We see that agreement is better for the path that opens first, results diverge as more paths open. This matches the analyses given in chapter 3, where we showed that conducting islands have longer interaction range than non-conducting ones. In a steady state, interaction length decreases as $C_G / \langle C \rangle$ increases. Indeed, we see better agreement for big $C_G / \langle C \rangle$. Another prominent feature in fig. 4.6 is that the area of each loop is smaller for the vertical array, relative to the matching single island.

It seems that interactions with paths without hysteresis, which are also the ones that open first, tend to decrease the hysteresis in paths that open later.

4.2.2 Tunneling capacitance

We now turn to examine the current through longer paths. We focus on the case where voltage increases symmetrically. In that case, left electrode has larger voltage than the gate, and the right one has a lower voltage. When external voltage is high enough, carriers start to tunnel from left to right. They propagate deeper into the array, as external voltage increases. The left side of the array becomes positively charged while the right side charges negatively. This process continues until the positive and negative areas meet, around the middle column, allowing carriers to propagate from one electrode to the other (see https://github.com/kasirershaharbgu/random_2D_tunneling_arrays for video-clips of currents and occupations in different arrays). This is when conduction becomes possible. But steady-state current does not necessarily flow yet. Charge distribution might relax into a non-conducting state, after a short time (this is the same as a jump that leads to a non-conducting state, as we saw for a single island).

Conduction can start with a jump, or continuously, depending on array parameters. When voltage increases further more, new paths open. Current jumps occur either when a new path opens with a jump, or when a jump in the gate charge of a conducting island occurs. Jumps in the gate charge of a non-conducting island would have only short range effect (for $C_G > \langle C \rangle$), as shown in chapter 3, and thus also a negligible effect on current.

For $T = 0$, the work required for tunneling is resistance independent. Examining the master equation graph representation (fig. 3.3), we see that the graph structure (vertices and edges locations and directions) is resistance independent. Therefore, the possible paths for a given external voltage, and gate charge distribution, are determined by tunneling capacitance realization. Nonetheless, the steady state charge distribution will be resistance dependent, as tunneling rates are. To summarize, tunneling capacitance distribution determines the possible paths. To determine in which of those current will actually flow, we need to take resistance into account.

Fig. 4.7 shows the average (over different realizations) of different I-V curve characteristics, as a function of capacitance disorder¹.

The first path to conduct, in each array, will be the one with smallest energy barriers sum (see eq. 3.21). The energy barrier for each tunneling junction goes approximately like 1 over its capacitance. For small disorder, the first path to conduct is one of the shortest paths, and threshold voltage behaves in a similar way to the single island case, where threshold decreases as capacitance disorder increases (fig. 4.7h). For higher disorder, it becomes more probable for the shortest paths to be blocked by junctions with small capacitance. To open a longer path, a larger voltage is required (since external voltage spreads over more junctions). Therefore, threshold voltage starts increasing with capacitance disorder. This happens for smaller disorder in smaller arrays (fig. 4.7d), when there are less possible paths.

For small capacitance disorder, all paths will start to conduct together and we get a big current jump (see fig. 4.7f). When disorder increases, paths no longer open together. Each path opening will contribute a smaller jump. For large arrays, hysteresis loop area would also be smaller when disorder increases, since if paths do not open together, interaction with the first conducting path would suppress

¹Resistance and capacitance values distributes as e^α where α is a uniform random variable. Averages and standard deviations were calculated for the realized values.

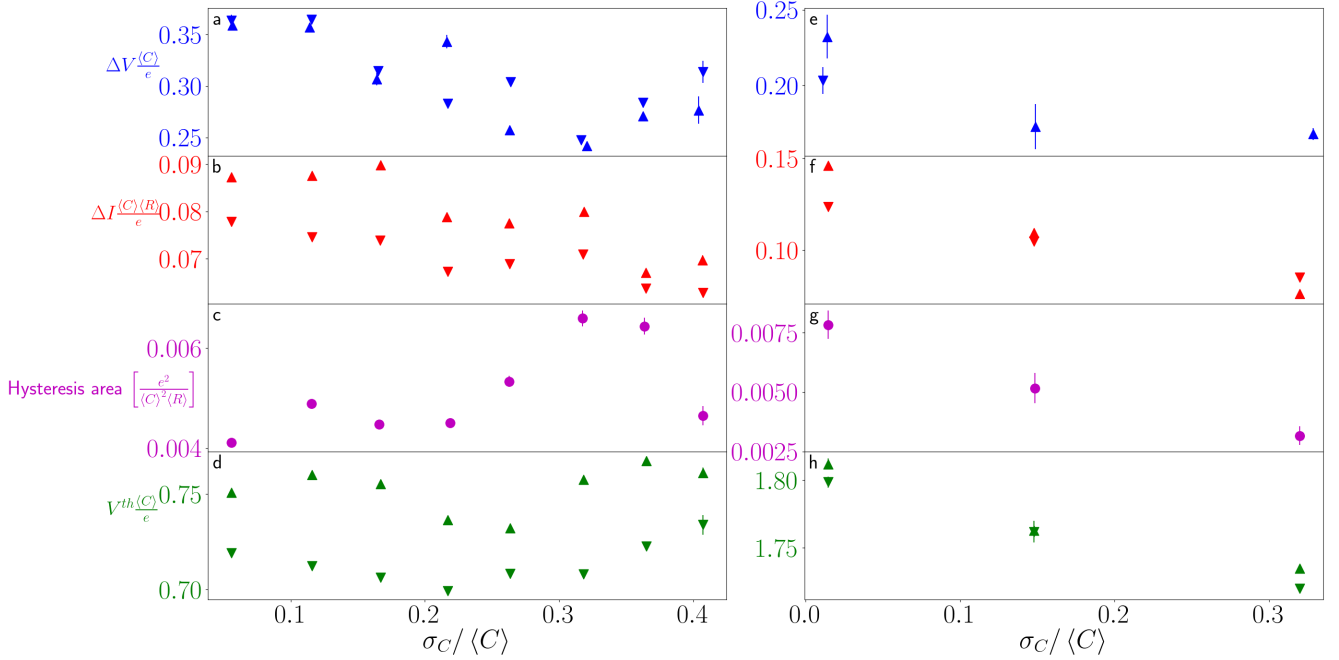


Figure 4.7: Hysteresis jumps and threshold voltages as a function of capacitance disorder. Calculated by averaging the results from > 10 different array realizations for each data point, for various R disorder values. Error bars show standard error of averages. Upwards pointing triangles - increasing voltage. Downwards pointing triangles - decreasing voltage. **(a-d)** Jumps average separation (a), height (b), hysteresis area (c) and threshold voltages (d), for 3×3 arrays at $T = 0$. **(e-h)** Jumps average separation (e), height (f), hysteresis area (g) and threshold voltage (h) for 10×10 arrays at $T = 0.001 \frac{e^2}{\langle C \rangle^2}$. **Common parameters:** $\phi = 0$, $R_G = 100 \langle R \rangle$, $C_G = 10 \langle C \rangle$. **(a-d):** $V_{max} = 2 \langle C \rangle / e$. **(e-h):** $V_{max} = 1.1 \langle C \rangle / e$.

hysteresis in paths that open later (fig. 4.7g). For small arrays, hysteresis area is non-monotonic in capacitance disorder (fig. 4.7c). This can be the result of increasing $V_{\uparrow\downarrow}$, like for the single island case. As for the separation between jumps, for small disorder, jumps in all paths happen together. When capacitance disorder increases, jumps in different paths happen for different voltages, since each path has a different jumps separation. Therefore, the separation between jumps decreases (fig. 4.7a,e).

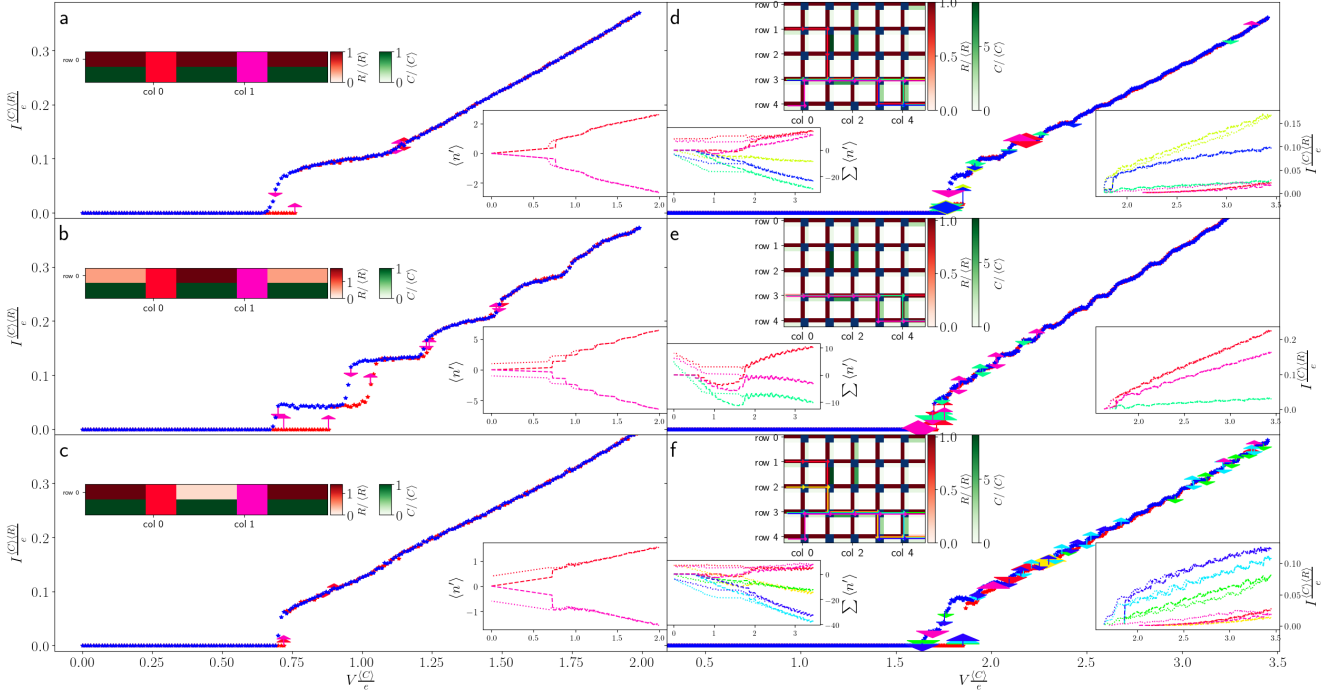


Figure 4.8: Tunneling resistance effect on current for 1D and 2D arrays. **Main figures:** I-V curves, red - increasing voltage, blue - decreasing voltage. Small arrows indicate occupation jumps with a different color for each island (a-c) or current jumps with a different color for each path (d-f). The same colors are used for insets. **Upper insets:** Resistance (red) and capacitance (green) of tunneling junctions. Each island (a-c) or path (d-f) is marked with its color. **Lower right insets:** Island average occupation $\langle n' \rangle$ (a-c) or current in each path (e-f) as a function of V . **Lower left subplots** sum of average occupations for all islands in each path (color indicating path). (a) 1D array with uniform resistance and capacitance. Unlike the case of a single island with uniform resistance, we do see hysteresis. Current and occupation jumps happen for the same voltage. (b) 1D array with small entrance and exit resistance. Here we see more jumps and hysteresis loops. The threshold voltage is slightly higher than in (a) as 2 occupation jumps are required for current to flow. (c) 1D array with large entrance and exit resistance. We see one jump and hysteresis loop with small area (compared with (a)). (d) 2D array with random capacitance and uniform resistance. We see 2 big jumps and a single hysteresis loop, associated with the current in blue and yellow paths. Paths with more islands on the left part of the array (pink and red) tend to be charged positively. Paths with more islands on the right (blue, yellow and green) tend to be charged negatively. (e) The same array as in (d), with smaller entrance resistance in row 3. Path configuration has changed a little (current now flows through the right part of row 2). We see a bigger hysteresis loop for small voltages. All paths have larger average occupation compared with (d). (f) The same array from (d), with smaller exit resistance for row 4. Path configuration is the same as in (d). The path with biggest current is no longer the straight path (in yellow) but a path that involves the small resistance (blue path). We see bigger jump and hysteresis loop for small voltages. We can also see small jumps and hysteresis loops for bigger voltages, that do not exist in (d). All paths have smaller average occupations compared to (a). This is especially pronounced in paths that involve the small resistance (blue, green and red). **Common parameters:** $\phi = 0$, $R_G = 100 \langle R \rangle$. (b): $R_{max}/R_{min} = 3$. (c): $R_{max}/R_{min} = 7$ (d-f): $\sigma_C = 0.648 \langle C \rangle$. $R_{max}/R_{min} = 10$.

4.2.3 Tunneling resistance

When the array is conducting, tunneling rates, which are affected by resistance, will determine the charge distribution in the array. The resistance of the junctions that connect an electrode to the array

have a special importance, since they have a large effect on the total number of carriers in the system. We will refer to the junctions that connect the left electrode to the array as "entrance junctions" and to the ones that connect it to the right electrode as "exit junctions". In fig. 4.8, simulation results which demonstrate the effect of resistance disorder are plotted. Fig. 4.8a,d show that hysteresis and jumps can occur in an array with no resistance disorder (unlike a single island, where we showed that disorder is required). Changing the entrance or exit junctions resistance has a visible effect on current. Small entrance(exit) resistance (relative to the average one) enables more carriers to enter(exit) the path. Therefore, the average occupation of each island in the path jumps more often. In this case, we will see more jumps and bigger hysteresis loops (4.8b). If the path is not symmetric, it might be easier to add or remove carriers (for example, the main paths in 4.8d tend to lose more carriers). In that case, changing the resistance such that the asymmetry is enhanced will have a larger effect on current (4.8f), than a change that reduces the asymmetry (4.8e). Larger entrance and exit resistance will reduce hysteresis, since it would be "harder" for carriers to enter, or exit, the array, and thus the average occupations, and gate charges, will not change significantly while conduction occurs (4.8a). Changing the resistance of a junction that is not part of a conducting path does not effect the current . If a junction is part of a path, but is far from electrodes (in terms of interaction length, see chapter 3) changing its resistance would only have a negligible effect (see additional results in appendix C).

The dependencies of different I-V curve characteristics on resistance disorder are plotted in fig. 4.9. Hysteresis area increases with disorder (fig. 4.9a,g), as could be expected from the single island results (eq. 4.7).

For 3×3 arrays at $T = 0$, Jumps height also increases with disorder (fig. 4.9b), unlike the case for a single island, where it is resistance independent. This could be explained by the differences between different paths. For high R disorder we will get paths with small resistance, in which most of the current will flow. Current jumps in those paths would be bigger than in others. Therefore, apparent jumps would mostly come from these paths, and be bigger than the average jump ($\sim e / [N(\langle C \rangle + C_G) \langle R \rangle]$). This also explains why separation between jumps first decreases, and later increases, with disorder (fig. 4.9c). At first, increasing disorder is adding more jumps (as for a single island, 4.8). Therefore separation between them decrease. Later, jumps in paths with big resistance become negligible and so we see less jumps, and larger separation.

For larger arrays, the threshold voltage is bigger (see eq. 2.10), in addition, we ran the simulation up to a voltage that is slightly higher than threshold (to avoid extremely long running time, see simulation description in chapter 3). Therefore, we see smaller hysteresis area, and detect less jumps, in these results. This makes the results for jump separation less reliable, since we need to detect at least 2 jumps to measure their separation. As for capacitance disorder, jumps height in big arrays relates to correlation between different paths. For small disorder, jumps in different paths occur together and combines into a big jump, while for larger disorder, jumps in each path happen separately and the measured jumps are smaller (4.9f).

Interestingly, threshold voltage also drops when disorder increases (despite being resistance independent for a single island). A possible explanation for the decreasing threshold is that, once conduction becomes possible, the average number of carriers in the conducting paths increases with resistance disorder. Interactions with this extra charge will enable conduction in nearby paths (as we saw earlier). When more paths conduct, it is more probable that the steady state would also be a conducting state,

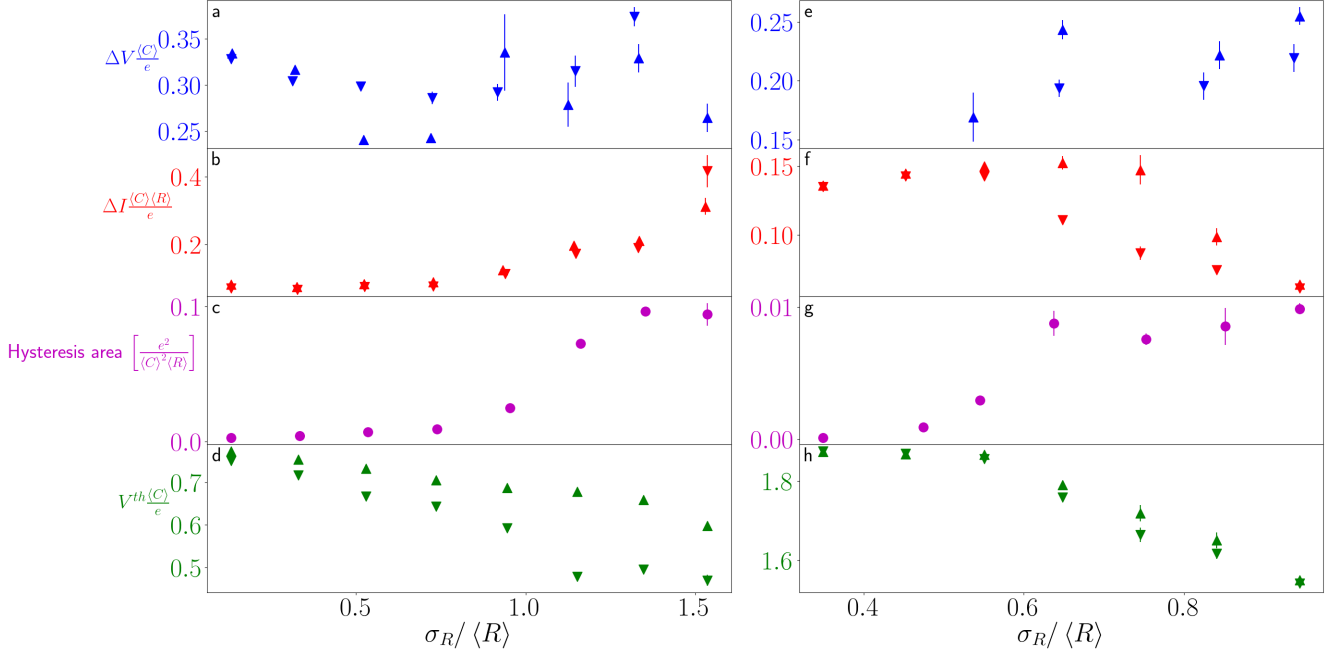


Figure 4.9: Hysteresis jumps and threshold voltages as a function of resistance disorder. Calculated by averaging the results from > 10 different array realizations for each data point, for various C disorder values. Error bars show standard error of averages. Upwards pointing triangles - increasing voltage. Downwards pointing triangles - decreasing voltage. (a-d) Jumps average separation (a), height (b), hysteresis area (c) and threshold voltages (d), for 3×3 arrays at $T = 0$. Hysteresis area and jumps height increase with disorder. Threshold voltages decrease when disorder increases. Average separation decreases at first, but then increases again as disorder grows. (e-h) Jumps average separation (e), height (f), hysteresis area (g) and threshold voltage (h) for 10×10 arrays at $T = 0.001 \frac{e^2}{\langle C \rangle^2}$. Jumps separation is calculated only for examples where 2 or more jumps were detected (hence, only for large disorder). Jump separation and hysteresis area increase with disorder. Threshold voltages decrease when disorder increases. Jump heights increase at first, but then decrease again for large disorder values. **Common parameters:** $\phi = 0$, $R_G = 100 \langle R \rangle$, $C_G = 10 \langle C \rangle$. (a-d): $V_{max} = 2 \langle C \rangle / e$. (e-h) $V_{max} = 2.2 \langle C \rangle / e$.

thus decreasing the threshold voltage.

4.2.4 Gate capacitance

In fig. 4.10 we compare results for the same realization, with different gate capacitance. As for a single island, increasing C_G (while keeping the same tunneling resistance and capacitance realization) makes hysteresis loop area and threshold voltage increase significantly. When there is no capacitance disorder (fig. 4.10a), and $C_G / \langle C \rangle$ is big, all paths open at once (as discussed earlier) and a big jump and hysteresis area are measured. For small $C_G / \langle C \rangle$, most islands do not satisfy the hysteresis condition (some of them will, because of resistance disorder) and we see almost no hysteresis. For an array with capacitance disorder (fig. 4.10b), we see multiple small jumps. For big $C_G / \langle C \rangle$, the hysteresis loop area is smaller than the uniform capacitance result. In contrast, for small $C_G / \langle C \rangle$, tunneling capacitance disorder enables more islands to satisfy hysteresis condition and we see larger hysteresis area, compared to the uniform capacitance result.

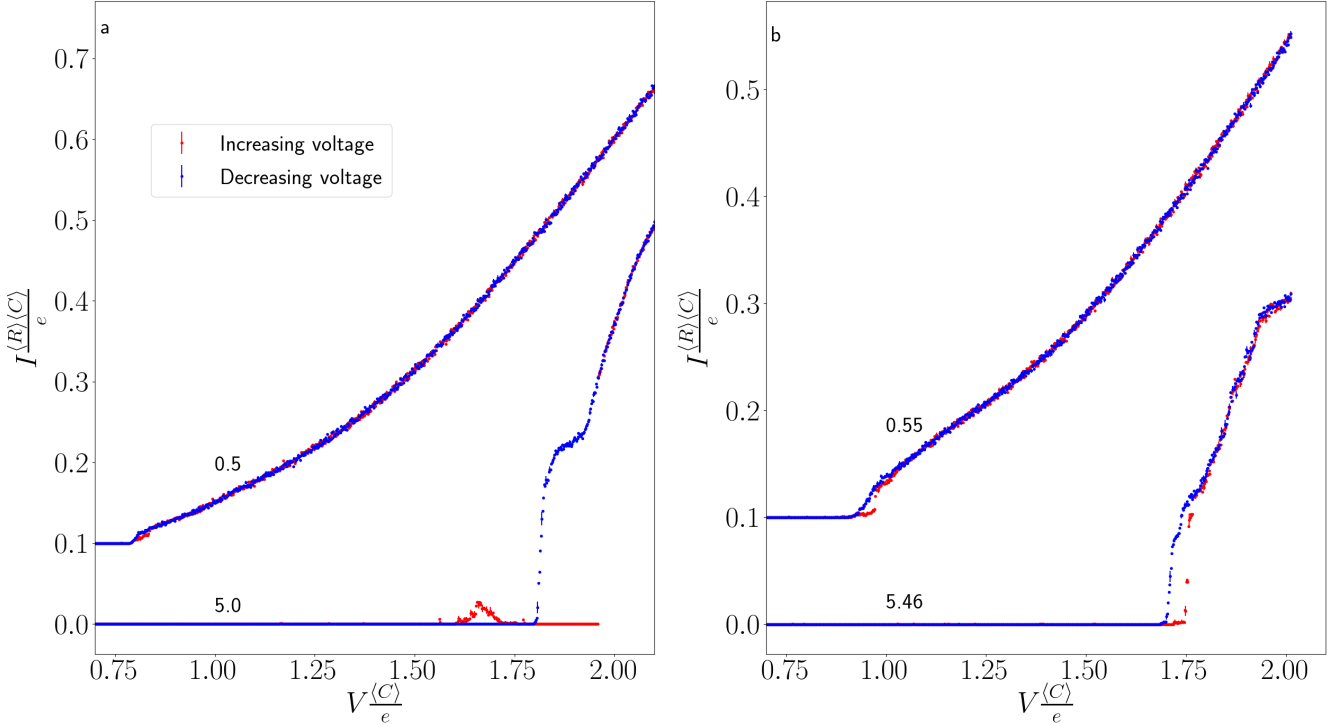


Figure 4.10: I-V curves for 10×10 arrays with different gate capacitance. (a) An array realization with $\sigma_C = 0$. (b) An array realization with $\sigma_C = 0.57 \langle C \rangle$. The value of $C_G / \langle C \rangle$ is indicated above each curve. Threshold voltage and hysteresis loop area increase with C_G . Curves are shifted up by 0.1 with respect to each other. **Common parameters:** $\phi = 0$, $R_G = 86 \langle R \rangle$, $T = 0$, $\sigma_R = 4.8$. (a) $V_{max} = 2.2 \langle C \rangle / e$. (b) $V_{max} = 2 \langle C \rangle / e$.

4.2.5 Temperature

Fig. 4.11a,b show the average temperature dependency of threshold voltage and hysteresis area. For finite temperature, tunneling events that increase the total energy by $\sim k_B T$ become possible. To tunnel, a carrier needs to overcome an energy barrier of $\sim e^2 / 2Z \langle C \rangle$, where Z is the number of nearest neighbors, (this is a generalization of 3.21). As $k_B T$ approaches this value, carriers can overcome this barrier for smaller voltages, and therefore threshold voltage decreases. The hysteresis in our model is a consequence of the change in gate charges, which, in turn, changes the steady-state voltages. Examining eq. 3.22, we see that the relevant energy scale for this change is $\sim e^2 / 2Z (\langle C \rangle + C_G)$, smaller than the energy barrier. This is why increasing temperature has stronger effect on hysteresis, than it has on threshold voltage.

In fig. 4.11c, we compare I-V curves, of the same 10×10 array, for different temperatures. As temperature increases, threshold voltage and hysteresis loop area become smaller (as can be seen in fig. 4.11a,b). The big hysteresis loop we see for small temperatures diminishes quickly when temperature rises, and we are left with smaller loops, which also disappear for even higher temperatures. These results are, qualitatively, similar to the experimental results from [12] (which are also plotted in fig. 1.1).

In fig. 4.12, resistance, as a function of the inverse temperature, is plotted. It was calculated for the same 10×10 array as in fig. 4.11, for different external voltage and C_G values. As for a single island, the curves with diverging resistance for $T \rightarrow 0$ were fitted to Arrhenius law, while other curves were fitted to its modified version. Agreement between fit and numerical results is better for small C_G , when there

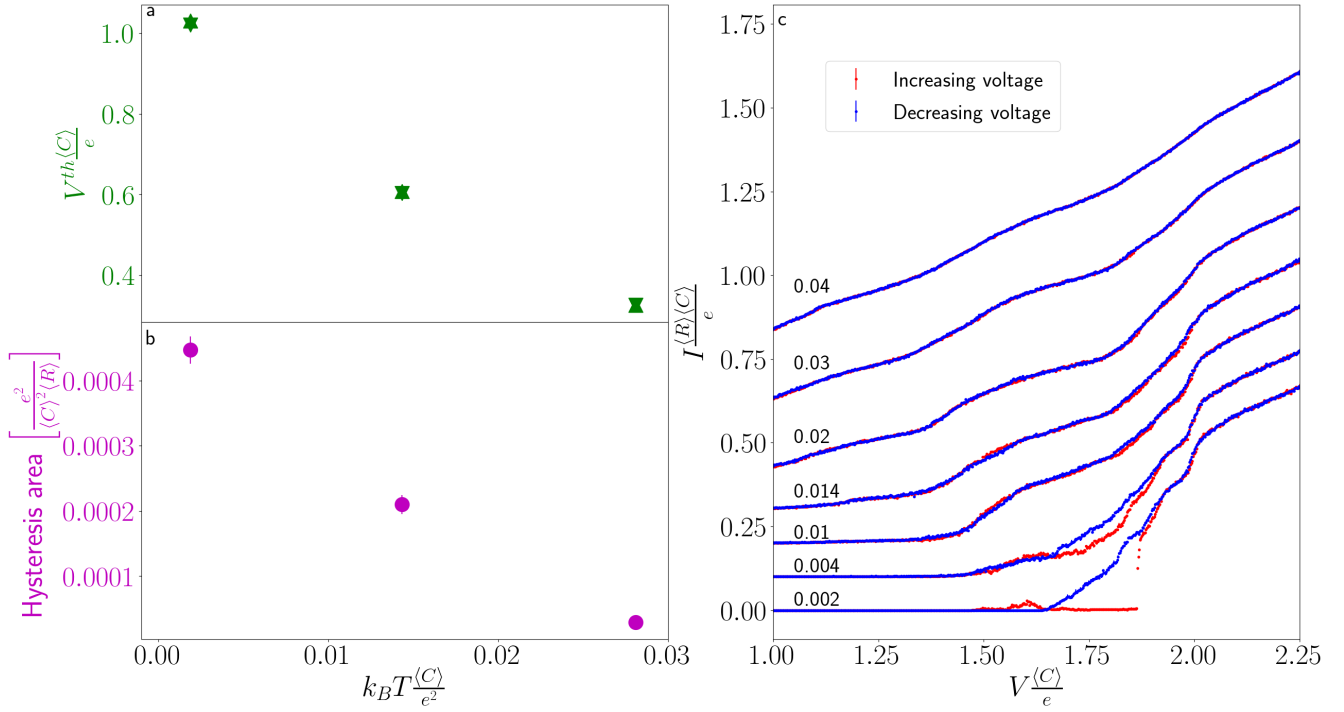


Figure 4.11: Temperature effect on current. As temperature increase, hysteresis loop area and threshold voltage decreases. (a) Average threshold voltage as a function of temperature. Upwards pointing triangles - increasing voltage. Downwards pointing triangles - decreasing voltage. (b) average hysteresis area as a function of temperature. Error bars in (a),(b) indicate standard errors. (c) Numerical results for a square 10×10 array in different temperatures, using the same disorder realization. Value of $k_B T \frac{\langle C \rangle}{e^2}$, for each curve, is indicated above it. Curves for different T are shifted up by 0.1 with respect to each other. **Common parameters:** $V_{max} = 2.4 \langle C \rangle / e$, $\phi = 0$, $R_G = 50 \langle R \rangle$, $C_G = 5 \langle C \rangle$, $\sigma_C = 0.05 \langle C \rangle$, $\sigma_R = 0.9 \langle R \rangle$.

are less current jumps, than it is for large C_G .

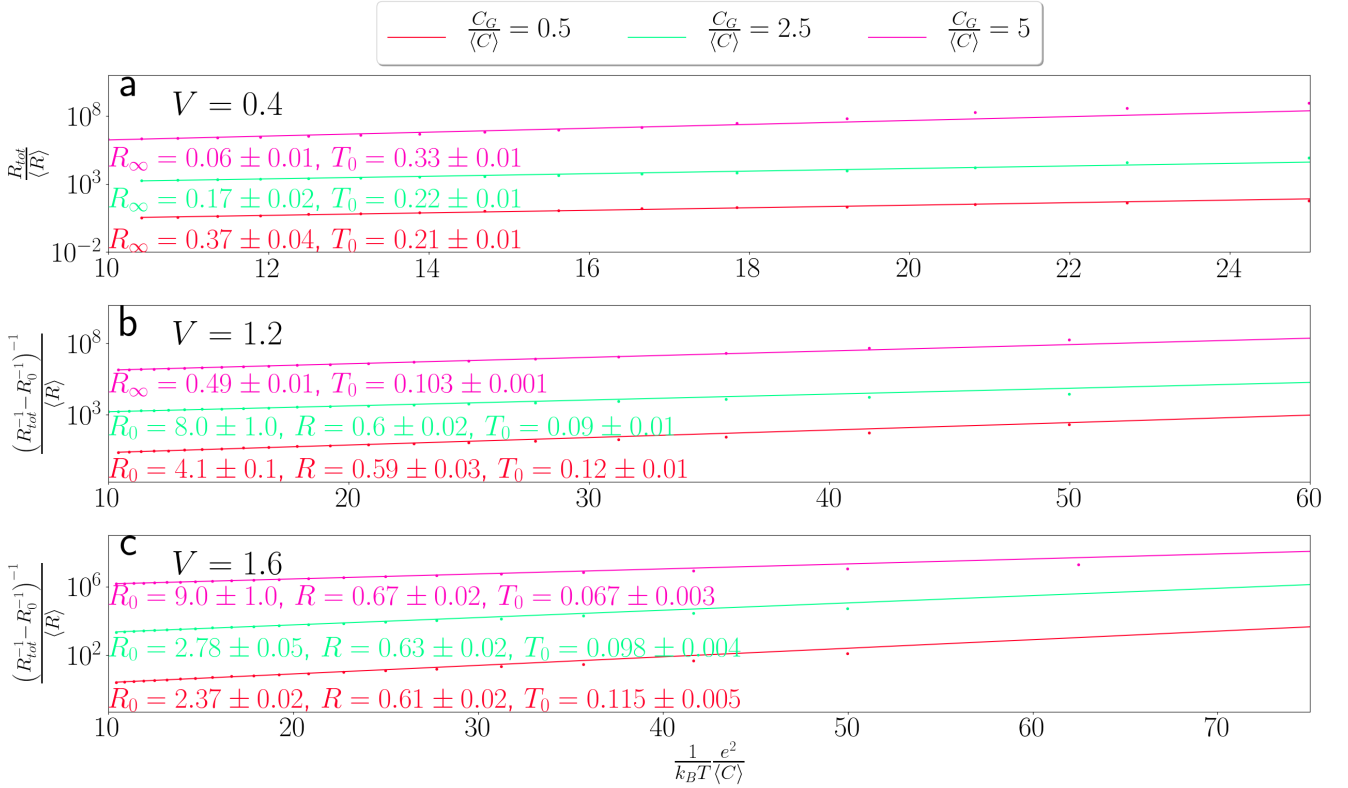


Figure 4.12: Resistance vs. inverse temperature for a 10×10 array (dots). Calculated for the same array as in 4.11, for different voltage and gate capacitance values and fitted to Arrhenius law (continuous curves). Curves are shifted up by 10^3 from each other. Resistance, temperature and voltage are measured in units of $\langle R \rangle$, $\frac{e^2}{\langle C \rangle}$ and $\frac{e}{\langle C \rangle}$ respectively. (a) For $V = 0.4 \frac{e}{\langle C \rangle}$, voltage is below threshold for all C_G values. resistance diverges when $T \rightarrow 0$. All curves are fitted to Arrhenius law $R = R_\infty e^{T_0/T}$ (b) For $V = 1.2 \frac{e}{\langle C \rangle}$, voltage is below threshold for $C_G = \langle C \rangle$. This example was fitted to Arrhenius law. For $C_G = 0.5, 2.5$ voltage is above threshold and curves are fitted to modified Arrhenius law, $R^{-1} = (R_\infty^{-1} - R_0^{-1}) e^{-T_0/T} + R_0^{-1}$. (c-d) For $V = 1.6 \frac{e}{\langle C \rangle}$, voltage is above threshold for all C_G values and curves are fitted to modified Arrhenius law. **Common parameters:** $\phi = 0$, $R_G = 50 \langle R \rangle$, $\sigma_C = 0.05 \langle C \rangle$, $\sigma_R = 0.9 \langle R \rangle$.

4.2.6 Superconducting arrays

In superconducting systems we expect a tunneling of both Cooper-pairs, and quasi-particles. To include both processes in our simulation, we used the tunneling rates calculated in [28] (eq. 2.12 and 2.13). According to these results, since Cooper-pairs occupy only one energy state, they require some energy absorption mechanism to tunnel (otherwise only tunnelings that don't change the total energy are allowed). Since we want to check the effect of Cooper-pairs tunneling on our results, we used the high-impedance limit (eq. 2.4). Tunneling rates were calculated, in a similar way to [13], assuming that energy is absorbed by the intrinsic impedance of the array. In that case, the dominant impedance comes from the gate connections (big R_G in the slow relaxation limit) and the effective charging energy (E_c in eq. 2.4) is given by $\frac{e^2}{2C_G}$. E_j was calculated using the standard formula [45]

$$E_j = \left(\frac{\hbar}{2eR_T} \right) \left(\frac{\pi\Delta}{2e} \right) \tanh \left(\frac{\Delta}{2k_B T} \right) \quad (4.12)$$

The calculated tunneling rates are plotted in fig. 4.13a. Cooper-pairs tunneling rates (solid curves in fig. 4.13a) are centered around $(-\Delta E) \approx 4E_c$ which is the energy that is best absorbed by the intrinsic impedance (see eq. 2.4). Quasi-particles require $(-\Delta E) > 2\Delta$ and E_c , to overcome the superconducting gap and, in addition, to compensate for the energy that is absorbed by the intrinsic impedance (see dashed curves in fig. 4.13a). For larger energy gains, rates grow linearly, in a similar way to the tunneling rates of electrons (purple dotted curve in fig. 4.13a). For $\Delta \approx 2E_c$, both cooper pairs and quasi-particles tunneling would give a significant contribution to the current. For $\Delta \ll E_c$, only quasi particles would contribute to the current.

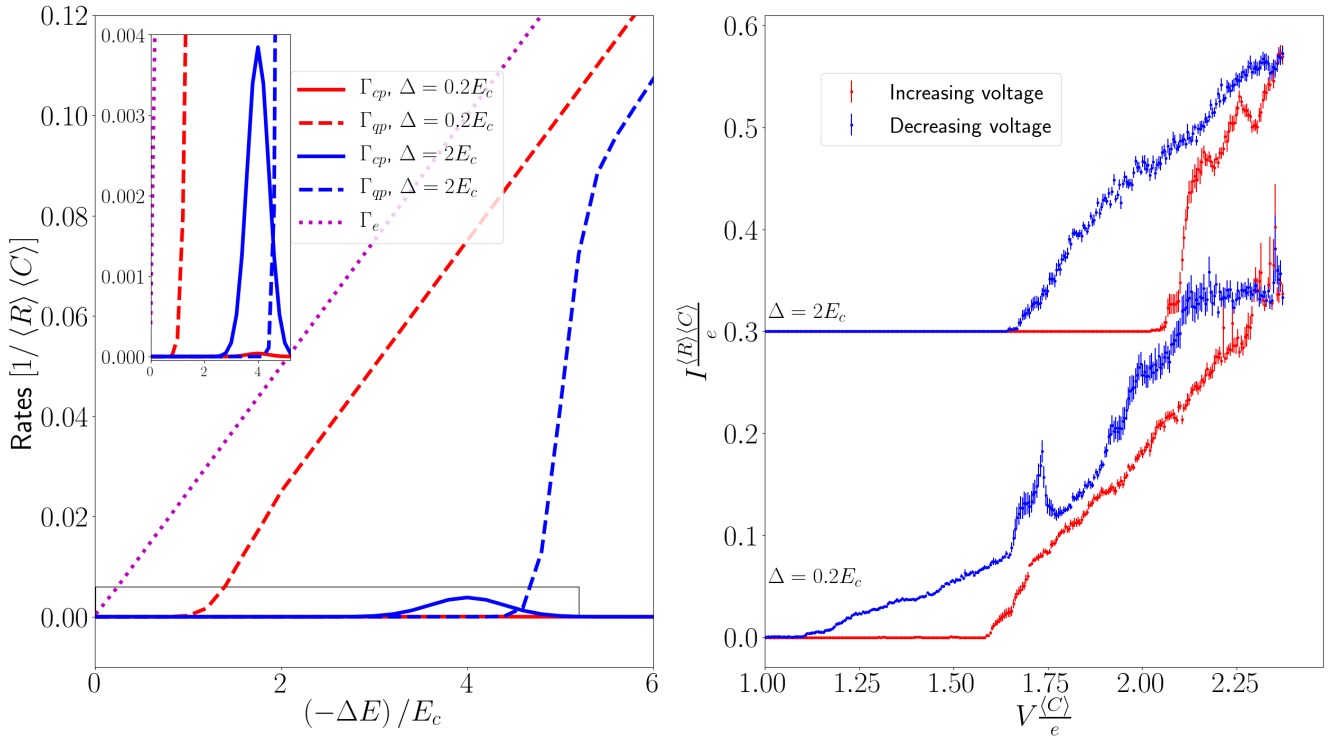


Figure 4.13: Results for a superconducting system. (a) Cooper-pairs (solid line) and quasi-particles (dashed line) tunneling rates, for different superconducting gaps. The tunneling rate for electrons in the small impedance limit (purple dotted line) is plotted for comparison (Inner set) close-up view of the area marked by a rectangle. (b) I-V curve for the same 5×5 array, with different superconducting gaps (indicated near each curve). Curves are shifted up by 0.3 from each other. Error-bars indicate standard errors. **Common parameters:** $k_B T = 0.4 \cdot 10^{-3} \frac{e^2}{\langle C \rangle}$, $E_c = 0.025 \frac{e^2}{\langle C \rangle}$, $V_{max} = 2.4 \langle C \rangle / e$, $\phi = 0$, $R_G = 234 \langle R \rangle$, $C_G = 21 \langle C \rangle$, $\sigma_C = 0.64 \langle C \rangle$, $\sigma_R = 7.8 \langle R \rangle$.

We used our simulation with these rates to calculate the current through a 5×5 array. The resulted I-V curves are plotted in fig. 4.13b. For both superconducting gap values we see hysteresis and jumps. For $\Delta < E_c$, the threshold voltage is smaller and we see smaller current jumps than for $\Delta = 2E_c$.

As we saw for normal arrays, current jumps occur when gate charges, or average occupations, jump. In the case of Cooper-pairs, those jumps would be bigger, because they have twice the charge of a quasi-particle. In addition, if Cooper-pairs and quasi-particles tunnelings are possible for nearby ΔE values, a jump in average occupation, that was created by a Cooper-pair tunneling, will make it easier for quasi-particles to tunnel later. Therefore, in the case $\Delta = 2E_c$ (upper curve in fig. 4.13b), we mostly see big jumps for voltages near threshold, when both Cooper-pairs and quasi-particles tunnelings are possible.

4.3 Comparison with other models

In this section we would compare our model results with those of existing models, that were reviewed in chapter 2.

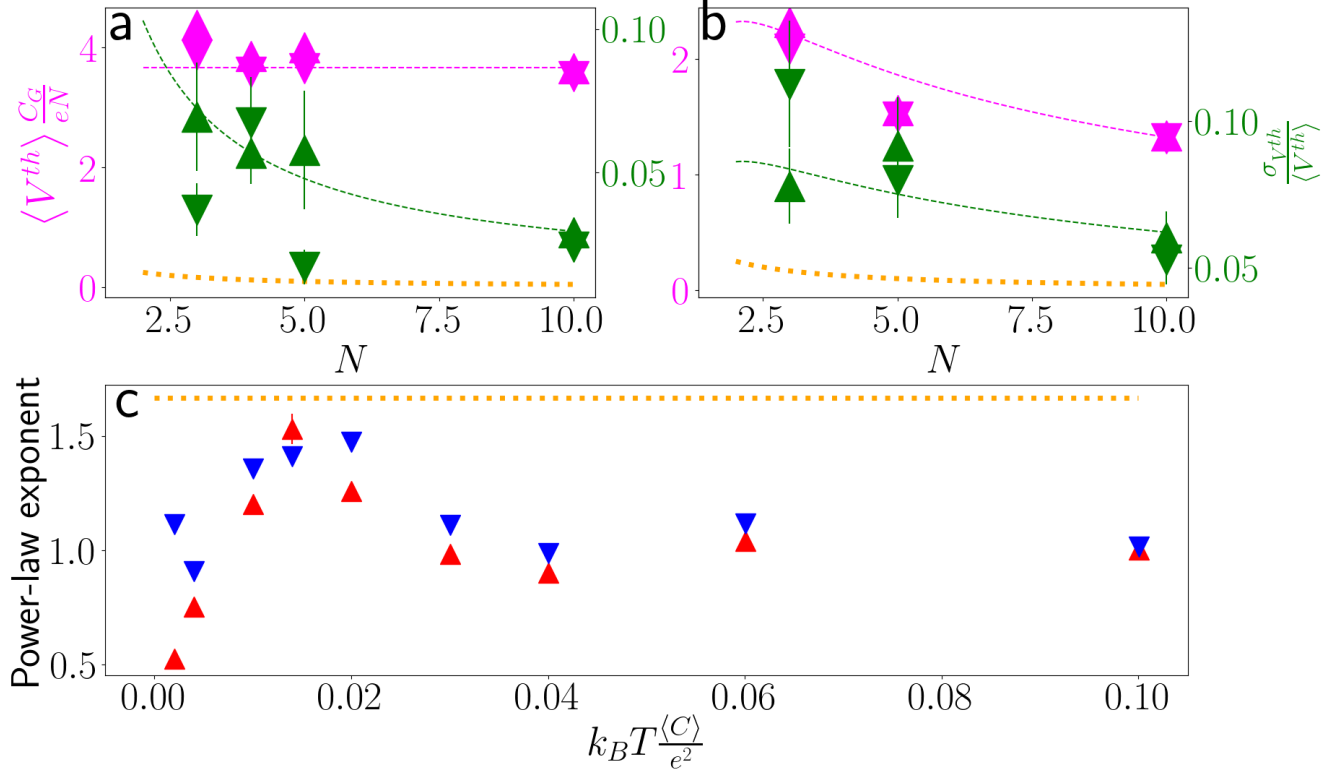


Figure 4.14: Comparison with previous random array results. (a-b) Comparison with threshold voltage average (in pink) and standard deviation (in green) as estimated in [38]. For 1d arrays (a), $\langle V^{th} \rangle / (eN)$ was fitted to a constant function and $\sigma_{V^{th}} / \langle V^{th} \rangle$ to C/N , where C is constant. For 2d arrays (b), both were fitted to $CN^{-2/3} (\ln N)^{1/2}$. Upwards pointing triangles - simulation results for increasing voltage. Downwards pointing triangles - simulation results for decreasing voltage. Dashed curves - fits to theoretical results. Threshold voltages, for an arras with no disorder [6], are plotted for comparison (orange dotted curves). (c) Power law approximation exponents for $I_{\overline{NC_G(R)}}^e$ as a function of $\frac{V-V^{th}}{V^{th}}$. Calculated for the same array as in fig. 4.11, at different temperatures. Red triangles - increasing voltage. Blue triangles - decreasing voltage. Power law exponent calculated by Middleton and Wingreen is plotted for comparison (orange dotted line). **Parameters:** (a,b) $\langle C \rangle < C_G < 10 \langle C \rangle$, $0 < \sigma_C < \langle C \rangle$, $0.5 \langle R \rangle < \sigma_R < 1.1 \langle R \rangle$, $T = 0$. (c) $V_{max} = 2.4 \langle C \rangle / e$, $\phi = 0$, $R_G = 50 \langle R \rangle$, $C_G = 5 \langle C \rangle$, $\sigma_C = 0.05 \langle C \rangle$, $\sigma_R = 0.9 \langle R \rangle$.

4.3.1 Random array model

Fig. 4.14 compares our results with the ones predicted by Middleton and Wingreen (M&W) [38]. For 1D arrays of length N , they predicted that the threshold voltage should be proportional to eN/C_G , so that $\langle V^{th} \rangle / (eN)$ should be constant. $\sigma_C V^{th} / \langle V^{th} \rangle$ was predicted to be proportional to $1/N$. For square arrays with size $N \times N$, both $\langle V^{th} \rangle / (eN)$ and $\sigma_C V^{th} / \langle V^{th} \rangle$ should be proportional to $N^{-2/3} (\ln(N))^{1/2}$. To calculate our model prediction, we used a set of existing $T = 0$ results, including arrays with different

resistance and capacitance disorders, and different C_G . Therefore, there is a lot of variability between the different realizations, used for this calculation. In addition, the used set of realizations is biased towards examples with big disorder and large C_G , as those are the cases we were mostly interested in. Despite this disclaimer, it seems like our results for the threshold voltage could be fitted with M&W's predictions, or at least are not contradictory to them. Our results for $\sigma_{V^{th}}$ for increasing voltage are also not in contradiction with M&W, although we can not say they are in good agreement. For decreasing voltage, $\sigma_{V^{th}} / \langle V^{th} \rangle$ is usually smaller than it is for increasing voltage, and the results do not show any clear trend as a function of N . Our thresholds are always higher than those calculated for an array with no disorder [6].

Another prediction by M&W [38], is the power law approximation near threshold, the predicted power law exponent is 5/3. In our model, power law exponent changes with temperature, as can be seen in fig. 4.14. Calculated exponent ranges from $\sim 1/2$ for low temperatures, and up to about 3/2, which is achieved when $V^{th} \sim 0$. For high temperatures the curve becomes approximately linear. In addition, there is a big difference between the power-law approximation for increasing and decreasing voltage at low temperatures. Exponent for decreasing voltage is higher than for increasing voltage (except for a single example). It seems like power-law exponent is mostly dependent of the threshold value. Exponent is higher for lower thresholds, down to $V^{th} \sim 0$ and then it converges towards 1. Our results are always lower than M&W result of 5/3. This is probably the outcome of our small array size, 10×10 , although an I-V measurement for a quantum dots array of size 200×200 was best fitted with an exponent of 3/2 [17].

4.3.2 Electrons overheating model

As described in chapter 2, a successful model, that is not based on a random array, is electrons overheating model [3]. A strong support to this model was given in a paper by Levinson et. al. [35]. In it, they have calculated electrons temperature, using 2 different measurements of the current, in perpendicular directions. Their results were in good agreement with each other.

To check the prediction of our model, for the same experimental setup, we used a similar procedure to the one used in [35]. First, we ran a simulation with changing voltage in the horizontal direction, and calculated the resistance in both directions. Next, we ran a simulation with changing temperature, and calculated the temperature-resistance relation for both directions. We then used the results from both runs, to calculate electrons temperature as a function of the horizontal voltage. An example to simulation results is plotted in fig. 4.15. Full details for this procedure, along with more examples, are given in appendix D.

Our model offers an alternative explanation to the measurement results from [35]. Since horizontal voltage difference is higher than vertical, it is easier for carriers to flow from left to right than it is from up to bottom. Therefore, most of the current measured in the vertical direction, comes from paths connecting the right, or left, electrode to the upper or lower one (blue and red paths in fig. 4.15a). This is, in our model, the reason for correlation between horizontal and vertical currents. For voltages near threshold, which are also near the ones used to calculate the relation between temperature and resistance, this correlation between currents will translate to the same T_{el} . When current increases, horizontal resistance decreases slower than vertical, and we calculate higher electrons temperature in the vertical direction.

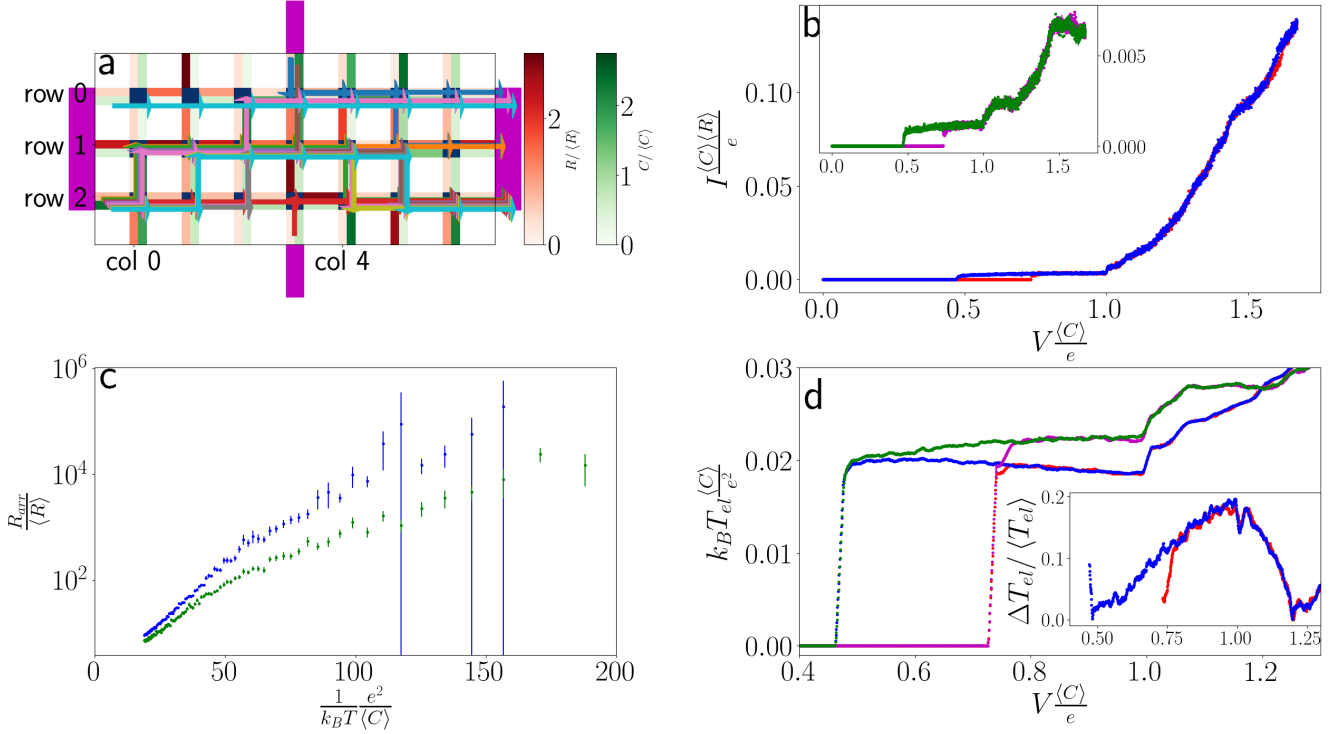


Figure 4.15: Perpendicular electron temperature Results for 3×7 array, for $C_G = 1.5 \langle C \rangle$. (a) Array parameters. Tunneling resistance (red) and capacitance (red) between conducting islands (blue). Electrodes locations are marked in purple. Current paths for maximum voltage are marked by colored arrows. They are plotted for the case when voltage on the top electrode is higher than on the bottom one. (b) I-V curve for horizontal (x) direction. Inset - I-V curve for perpendicular (y) direction. Blue and green - decreasing voltage, red and purple - increasing voltage. (c) Array resistance as a function of inverse temperature. Blue - horizontal (x) direction, green - vertical (y) direction. (d) Electrons temperature, calculated using the results from (b) and (c): Red - x-direction, increasing V ; Blue - x-direction, decreasing V ; Purple - y-direction, increasing V ; Green - y-direction decreasing V . Inset - measurement difference, normalized by mean. Red - increasing V , blue - decreasing V . **Parameters:** $|V^y| = 0.07 \frac{e}{\langle C \rangle}$, $\phi = 0$, $R_G = 160 \langle R \rangle$, $C_G = 1.5 \langle C \rangle$, $\sigma_R = 5 \langle R \rangle$, $\sigma_C = 0.5 \langle C \rangle$. For I-V simulation (b): $k_B T = 0.7 \cdot 10^{-3} \frac{e^2}{\langle C \rangle}$, $V_{max}^x = 1.67 \frac{e}{\langle C \rangle}$. For I-T simulation (c): $k_B T_{max} = 0.1 \frac{e^2}{\langle C \rangle}$, $V^x = 0.25 \frac{e}{\langle C \rangle}$

This is a consequence of the way those resistances were calculated. In our simulation, horizontal voltage increases, and so does the current. Vertical voltage, on the other hand, remains constant. Therefore, when using Ohm's law ($R = V/I$) to calculate resistance, it drops faster for the vertical direction relative to the horizontal one. In fig. 4.15a, the most significant path is from the upper electrode to the right one (blue path). In other arrays, where there are paths from left to right, the agreement between calculated electron temperatures is worse, since current in those paths does not contribute to the vertical current. This is more apparent in arrays with low disorder (see appendix D).

With all that said, the agreement in experimental results is still better than in our simulations. It could be because of the small system size used in our simulations (due to computational time limitations), but could also mean that our model needs to be improved in order to get better predictions.

4.4 Results summary

Using dynamical simulations, we showed that our model can reproduce hysteresis and jumps, in the slow relaxation limit. We examined the influence of different parameters on our model's I-V curve predictions, and found out the following:

1. To measure hysteresis and jumps, temperature ($k_B T$) must be lower than the energy scale for changes in the gate charge $\sim e^2/Z(\langle C \rangle + C_G)$. The same condition must be also satisfied by the voltage applied per junction (V_e/N).
2. For small tunneling-capacitance disorder, different paths open together and we predict bigger current jumps and larger hysteresis area. In this case, hysteresis and jumps are possible even with no tunneling-resistance disorder.
3. For big arrays with large tunneling-capacitance disorder, different paths open for different voltages. In this case, we will get more, although much smaller, jumps. To measure hysteresis in this case, resistance disorder would be required. If exists, hysteresis loop area would be smaller than in the low capacitance disorder case.
4. For big arrays, threshold voltage decreases for larger disorder, both in tunneling resistance and capacitance.
5. Tunneling resistance of entrance or exit junctions have the most significant effect on hysteresis. For small resistance in those junctions, we would get larger hysteresis loop area. Resistance of junctions that are far from electrodes, or not a part of a conducting path, have negligible effect on the I-V curve.
6. Increasing the gate capacitance, for the same array realization, will increase threshold voltage and hysteresis loop area, as well as the number of jumps.
7. For a superconducting array, increasing the superconducting gap would increase the threshold voltage. Superconducting gap values that enable tunneling of both Cooper-pairs and quasi-particles for certain voltages, will increase the measured current jumps heights, for those voltages.

Our model results can be qualitatively compared to different measurements. They are sensitive to the specific disorder realization. This explains the significant sample to sample differences and why large hysteresis loop area was measured for some samples [12], while almost no hysteresis was measured for other [15]. The I-V curve temperature dependency we have found is in qualitatively agreement with the measurements from [12]. For voltages below threshold, calculated resistance resembles Arrhenius law. This is especially true for small gate capacitance.

Our results are also qualitatively similar to those measured in quantum dots arrays. In [17], I-V curves for a single island and an array were measured, for different gate voltages. Those results are qualitatively similar to our results for different C_G . In the same paper, a relation between V_G and C_G is suggested (that does not exist in our model). If this relation is correct, our model can be used to explain these results. In addition, it might be possible to use our model for explaining the measurements from [40], where current was jumping between two values over time, as this might be a result of 2 near-by steady states at finite temperature.

Despite the success in reproducing hysteresis, and the qualitative agreement with some measurements, our model is far from being perfect. The most visible discrepancy lays in the location and height of the first jump. In the low temperature I-V curves that were observed in the lab, we see one big jump when voltage reaches its threshold value [12]. This jump brings the system immediately into the Ohmic region, with no further jumps, and is much bigger than all other jumps. We see the same behavior also for QDA [17]. In our results, first jump is followed by another, non-Ohmic, section, which sometimes includes smaller jumps. Only for higher voltages, the system reaches its Ohmic regime. This discrepancy might be fixed by increasing array size, since for bigger arrays, current jumps may be originated from numerous paths, and thus be bigger.

Chapter 5

Discussion and conclusion

In this work, we used a suggested model for electronic transport through a single conducting island [33], and generalized it for a random array. In this model, an extra degree of freedom was added to the system, in the form of charge distribution (in our model charge can be stored on the gate capacitor as well as on the different tunneling junctions, connecting the island to its neighbors, see next paragraph). We showed that, when the relaxation of charge distribution towards equilibrium is slow (compared to other relevant processes, in this case tunneling), this extra degree of freedom can "remember" the previous state of the system, and cause hysteresis, in a certain parameters range. For this parameters range, charge distribution has more than one stable steady-state solution. When external voltage is raised, one solution can lose its stability, and charge distribution "jumps" to the nearest stable solution. If this causes a significant change to the charge distribution in a conducting island, this jump would be also visible in the I-V curve.

To account for slow charge distribution relaxation, we used a simple model, where each island is coupled to its gate voltage through an RC -circuit. This model was chosen for its simplicity. The physical reality in disordered materials is probably more complicated. Relaxation to electrostatic equilibrium includes a rearrangement of charges in each island which is effected by interactions with charges from different islands and from the substrate (gate). We believe that our results, and the ability to reproduce jumps and hysteresis in particular, do not depend on the specific charge relaxation process, as long as relaxation time is much longer than the average time between tunnelings. Another aspect, that was not accounted for in this work, is the finite thermal relaxation time. Slow thermal relaxation can also be the cause of hysteresis, as shown in electrons overheating model, that was discussed earlier.

5.1 Research limitations

There were 2 main limitations for this work. The first limitation is a computational one. As discussed in chapter 3, running simulations for big arrays require a long running time¹. This would be a problem for any slow relaxation model, since slow relaxations mean that many tunneling events are required to reach a steady state. The running time becomes even longer for superconducting system, where there are more possible events (Cooper-pairs and quasi-particles tunnelings). A possible solution for this problem is using approximations to speed up simulation, we will discuss one possible approximation next.

¹The biggest arrays we used had size of 10×10 , those simulation took about a week to run

The second limitation is the difficulty to get testable predictions. This is an outcome of the many parameters that are needed to define each realization, and the difficulty to measure them directly in the lab. For this reason, the results we presented here were chosen as they most resemble measurement results. It is important to clarify that our results only show that it is **possible** to account for the measured result using our model, but lack a prediction of how **probable** it is. As we will discuss next, we can solve this problem by examining the influence of "easy to control" parameters, as temperature and magnetic field, on our model results. Another option is to run our simulations for many more disorder realizations and different parameters, to gain more statistics. Speeding up the simulation is essential for this solution to be feasible.

5.2 Future research suggestions

Our model and simulation can be used as a basis for future research on transport properties of disordered materials. One possible extension of our work would be to calculate our model transport properties for different tunneling rates, or charge relaxation processes. This would be easily done by applying minor changes to our simulation. In addition, a finite thermal relaxation can be added to our model, possibly using electrons overheating model's heat balance equation (eq. 2.16). Another interesting research direction is to use our model for predicting thermoelectric characteristics (e.g. Seebeck and Thompson effects). Those predictions can be then tested in the lab, to confirm or deny our model.

A more computational direction for future research is looking for approximations that would improve the running time of our dynamical simulations, while not effecting the results significantly. A possible method to speed up simulations, is by using " τ -leaping" approximation [23]. In this method, many tunneling events are simulated in parallel, by approximating them as independent events. Luckily, this would be a good approximation for big array, where tunnelings in far away islands can be considered as independent. We already wrote a basic implementation of this method, which can be found in https://github.com/kasirershaharbgu/random_2D_tunneling_arrays.

5.3 Conclusion

To conclude, we showed that measured I-V curves in disordered superconductors near SIT, that include hysteresis and current jumps, could be explained using a random array model. This was done by adding a slow degree of freedom, in the form of charge distribution, to our model. Our model, and simulation method, can be used as a basis for future research on disordered materials. In addition, the approach we used, adding a slow degree of freedom to account for hysteresis in a system, might be applicable to other disordered systems with hysteresis. We hope that our work, and future ones that would be based on it, would help improving the theoretical understanding of disordered superconductors near SIT, and disordered materials in general.

Appendix A

Single island detailed analysis

A.1 Model equations derivation

A schematic drawing of the model is plotted in figure 3.1. The model is composed of a conducting island, connected via 2 tunneling junctions to an external voltage, $V = V_L - V_R$. The left and right junctions have capacitance C_1, C_2 and tunneling resistance R_1, R_2 respectively. The island is coupled to gate voltage ϕ , via capacitance C_G and resistance R_G , connected in a row. For simplicity, we will consider positive carriers with charge e instead of electrons (with charge $-e$). Since island charge changes only due to tunneling, its total excess charge must be a whole multiplication of e

$$ne = Q_1 - Q_2 - Q_G \quad (\text{A.1})$$

where the sign of charges is as depicted in fig. 3.1.

A.1.1 Inter-tunneling relaxation

Between tunneling events, the total charge on the island, ne , is constant. We can derive the electrical behavior of the circuit using a simple application of Kirchhoff's Laws:

$$\begin{aligned} \frac{Q_1}{C_1} + \frac{Q_2}{C_2} &= V_R - V_L \\ \frac{Q_1}{C_1} + \frac{Q_G}{C_G} + \frac{dQ_G}{dt}R_G &= \phi - V_L \end{aligned} \quad (\text{A.2})$$

together with eq. A.1, we can solve for the charges

$$\begin{aligned} Q_1 &= \frac{C_1 \left(ne + C_2 (V_R - V_L) - C_G \left(V_L - \phi + \frac{dQ_G}{dt} R_G \right) \right)}{C_\Sigma} \\ Q_2 &= \frac{C_2 \left(-ne + C_1 (V_R - V_L) + C_G \left(V_R - \phi + \frac{dQ_G}{dt} R_G \right) \right)}{C_\Sigma} \end{aligned} \quad (\text{A.3})$$

where $C_\Sigma = C_1 + C_2 + C_G$. From here we get a differential equation for Q_G :

$$\begin{aligned} \frac{dQ_G}{dt} &= -\frac{Q_G - Q_n}{\tau} \\ \tau &\equiv \frac{R_G C_G (C_1 + C_2)}{C_\Sigma} \\ Q_n &\equiv \frac{C_G}{C_\Sigma} [(C_1 + C_2) \phi - C_1 V_L - C_2 V_R - ne] \end{aligned} \quad (\text{A.4})$$

with the solution

$$Q_G(n, t) = (Q_0 - Q_n) e^{-\frac{t}{\tau}} + Q_n, \quad (\text{A.5})$$

τ is the relaxation time of the system, Q_0 is the initial charge on C_G and Q_n is the steady state charge for n excess electrons on the island.

A.1.2 Tunneling rates

The tunneling rates are calculated using eq. 2.1. They depend on the energy difference, before and after tunneling. The charging energy for a state with given n and Q_G is:

$$E(n, Q_G) = \frac{1}{2} \left(\frac{Q_1^2}{C_1} + \frac{Q_2^2}{C_2} + \frac{Q_G^2}{C_G} \right) + Q_L V_L + Q_R V_R \quad (\text{A.6})$$

where Q_L, Q_R are the charges on left and right electrodes respectively. When a carrier is tunneling through a junction, it distorts the electrical equilibrium. From eq. A.3, we get the change in charges due to adding (+) or subtracting (-) one carrier from the island:

$$\begin{aligned} \Delta Q_1^\pm &= \pm \frac{C_1 e}{C_1 + C_2} \\ \Delta Q_2^\pm &= \mp \frac{C_2 e}{C_1 + C_2} \end{aligned} \quad (\text{A.7})$$

This change is compensated by charge transfer between junctions and electrodes, in addition to the tunneling itself. The change in electrodes charges, when a carrier is tunneling through the i 'th junction, is

$$\begin{aligned} \Delta Q_L^\pm &= -\Delta Q_1^\pm \mp e\delta_{i,L} \\ \Delta Q_R^\pm &= -\Delta Q_2^\pm \mp e\delta_{i,L} \end{aligned} \quad (\text{A.8})$$

Using eq. A.8 together with eq. A.6 and A.3, we can calculate the work required to tunnel through the i 'th junction onto the island (+) or from it (-):

$$W_i^\pm(n, Q_G, V) = \frac{e^2}{C_1 + C_2} \left(\frac{1}{2} \pm \left(n + \frac{Q_G}{e} \right) \pm (-1)^i \frac{C_1 C_2 V}{e C_i} \right) \quad (\text{A.9})$$

where $i = L(R)$ for tunneling through the left(right) junction. Notice that, using eq. A.3 and A.4, we can write W in terms of island's electric potential

$$U(n, Q_G, V) = \frac{Q_G + ne + C_1 V_L + C_2 V_R}{C_1 + C_2} \quad (\text{A.10})$$

as

$$W_i^\pm(n, Q_G, V) = \pm \frac{e}{2} [(U(n \pm 1, Q_G, V) - V_i) + (U(n, Q_G, V) - V_i)] \quad (\text{A.11})$$

This is exactly the average potential energy barrier crossed by the carrier (averaged for its height before and after the tunneling).

A.2 Master equation solution for $T = 0$

At $T = 0$ a carrier can tunnel only if, while doing so, it reduces the energy of the system. Since island's potential (eq. A.10) becomes higher(lower) when adding(removing) carriers to(from) island, the occupation would have a finite possible range. This will enable us to find an explicit solution for the master equation (eq. 3.6).

The solution will be for 2 cases, fast and slow relaxation (see chapter 3 for details).

A.2.1 Maximal and minimal island occupation

To add(remove) a carrier to(from) the island when there are n carriers on the island, the following condition should hold (+) for adding, (-) for removing)

$$\min [W_1^\pm(n, Q_G), W_2^\pm(n, Q_G)] < 0 \quad (\text{A.12})$$

This gives us the maximal and minimal n for a given voltage V and gate charge Q_G . For slow relaxation we get

$$\begin{aligned} n_{\max}(V, Q_G) &= \left\lceil \frac{C_i}{e} |V| - \frac{1}{2} - \frac{Q_G}{e} \right\rceil \\ n_{\min}(V, Q_G) &= \left\lfloor -\frac{C_j}{e} |V| + \frac{1}{2} - \frac{Q_G}{e} \right\rfloor \\ \text{where } &\begin{cases} i = 1, j = 2 & \text{if } V < 0 \\ i = 2, j = 1 & \text{if } V > 0 \end{cases} \end{aligned} \quad (\text{A.13})$$

For fast relaxation

$$\begin{aligned} n_{\max}(V) &= \left\lceil \frac{C_\Sigma}{C_1 + C_2} \left[\frac{C_i}{e} |V| - \frac{1}{2} - \frac{Q_0}{e} \right] \right\rceil \\ n_{\min}(V) &= \left\lfloor \frac{C_\Sigma}{C_1 + C_2} \left[\frac{-C_j}{e} |V| + \frac{1}{2} - \frac{Q_0}{e} \right] \right\rfloor \\ Q_0 &\equiv \frac{C_G}{C_\Sigma} [(C_1 + C_2) \phi - C_1 V_L - C_2 V_R] \end{aligned} \quad (\text{A.14})$$

Using eq. A.9 one can verify that, both for fast and slow relaxation

$$\begin{aligned} \Gamma_1^-(n), \Gamma_2^+(n) &= 0 \text{ if } V > 0 \\ \Gamma_2^-(n), \Gamma_1^+(n) &= 0 \text{ if } V < 0 \end{aligned} \quad (\text{A.15})$$

Which is just saying that carriers can't tunnel in the opposite direction to the applied voltage.

A.2.2 Steady-state probabilities

Setting the time derivative in the master equation (eq. 3.6) to zero, we get a set of equations for steady state probabilities. Steady state is realized when the probability of getting into a state with n carriers on the island is equal to the probability of getting out from the same state

$$\Gamma^+ (n - 1) p(n - 1) + \Gamma^- (n + 1) p(n + 1) = (\Gamma^+(n) + \Gamma^-(n)) p(n) \quad (\text{A.16})$$

where $\Gamma^\pm(n) \equiv \sum_i \Gamma_i^\pm(n)$. Since we know that there is a minimal value for n , for which $\Gamma^-(n) = 0$, we can use it to solve eq. A.16 for $p(n_{\min} + 1)$:

$$\begin{aligned} \Gamma^-(n_{\min} + 1) p(n_{\min} + 1) &= \Gamma^+(n_{\min}) p(n_{\min}) \Rightarrow \\ p(n_{\min} + 1) &= p(n_{\min}) \frac{\Gamma^+(n_{\min})}{\Gamma^-(n_{\min} + 1)} \end{aligned} \quad (\text{A.17})$$

And then use the solution to solve for $p(n_{\min} + 2)$

$$\begin{aligned} p(n_{\min} + 2) &= \frac{(\Gamma^+(n_{\min} + 1) + \Gamma^-(n_{\min} + 1)) p(n_{\min} + 1) - \Gamma^+(n_{\min}) p(n_{\min})}{\Gamma^-(n_{\min} + 2)} \\ &= p(n_{\min}) \frac{\Gamma^+(n_{\min} + 1)}{\Gamma^-(n_{\min} + 2)} \frac{\Gamma^+(n_{\min})}{\Gamma^-(n_{\min} + 1)} \end{aligned} \quad (\text{A.18})$$

Continuing the same way we find

$$p(n) = p(n_{\min}) \prod_{m=n_{\min}}^{n-1} \frac{\Gamma^+(m)}{\Gamma^-(m+1)} \quad (\text{A.19})$$

Since we usually assume the system starts from the neutral state, $n = 0$, it is beneficial to write the probabilities as a function of $p(0)$

$$p(n) = p(0) \begin{cases} \prod_{m=0}^{n-1} \frac{\Gamma^+(m)}{\Gamma^-(m+1)} & n > 0 \\ \prod_{m=n+1}^0 \frac{\Gamma^-(m)}{\Gamma^+(m-1)} & n < 0 \end{cases} \quad (\text{A.20})$$

$p(0)$ can be found from the normalization condition

$$\sum_{n=n_{\min}}^{n_{\max}} p(n) = 1 \quad (\text{A.21})$$

A.2.3 Solution for $V \geq 0$

From now on, we will assume $V \geq 0$ for simplicity. The solution for $V \leq 0$ can be obtained as a mirror reflection of the system ($V_L \leftrightarrow V_R, R_1 \leftrightarrow R_2, C_1 \leftrightarrow C_2$). Using the tunneling rates for $T = 0$ (2.3), we write the probabilities as

$$p(n) = p(n_{\min}) \left(\frac{R_2}{R_1} \right)^{n-n_{\min}} \frac{(\alpha - n_{\min})(\alpha - n_{\min} - 1) \cdot \dots \cdot (\alpha - n + 1)}{(\beta + n_{\min})(\beta + n_{\min} + 1) \cdot \dots \cdot (\beta + n - 1)} \quad (\text{A.22})$$

Where α, β are defined as

$$\begin{aligned}\alpha_{slow} &\equiv \frac{C_2 V}{e} - \left(\frac{Q_G}{e} + \frac{1}{2} \right) \\ \beta_{slow} &\equiv \frac{C_1 V}{e} + \left(\frac{Q_G}{e} + \frac{1}{2} \right)\end{aligned}\quad (\text{A.23})$$

for slow relaxation, and

$$\begin{aligned}\alpha_{fast} &\equiv \frac{C_2 C_\Sigma V}{e(C_1 + C_2)} - \frac{C_G}{2(C_1 + C_2)} - \left(\frac{C_\Sigma}{C_1 + C_2} \frac{Q_0}{e} + \frac{1}{2} \right) \\ \beta_{fast} &\equiv \frac{C_1 C_\Sigma V}{e(C_1 + C_2)} - \frac{C_G}{2(C_1 + C_2)} + \left(\frac{C_\Sigma}{C_1 + C_2} \frac{Q_0}{e} + \frac{1}{2} \right)\end{aligned}\quad (\text{A.24})$$

for fast relaxation. Notice that $\lceil \alpha \rceil = n_{max}, \lfloor -\beta \rfloor = n_{min} - 1$. From here, $p(n)$ can be calculated in terms of Hyper-geometric functions. The probability distributions are plotted in fig. A.1,A.2. The explicit expression is cumbersome and doesn't add to our understanding, so we won't give it here (see https://github.com/kasirershaharbgu/random_2D_tunneling_arrays). Instead, we will use approximated solutions for some simple cases.

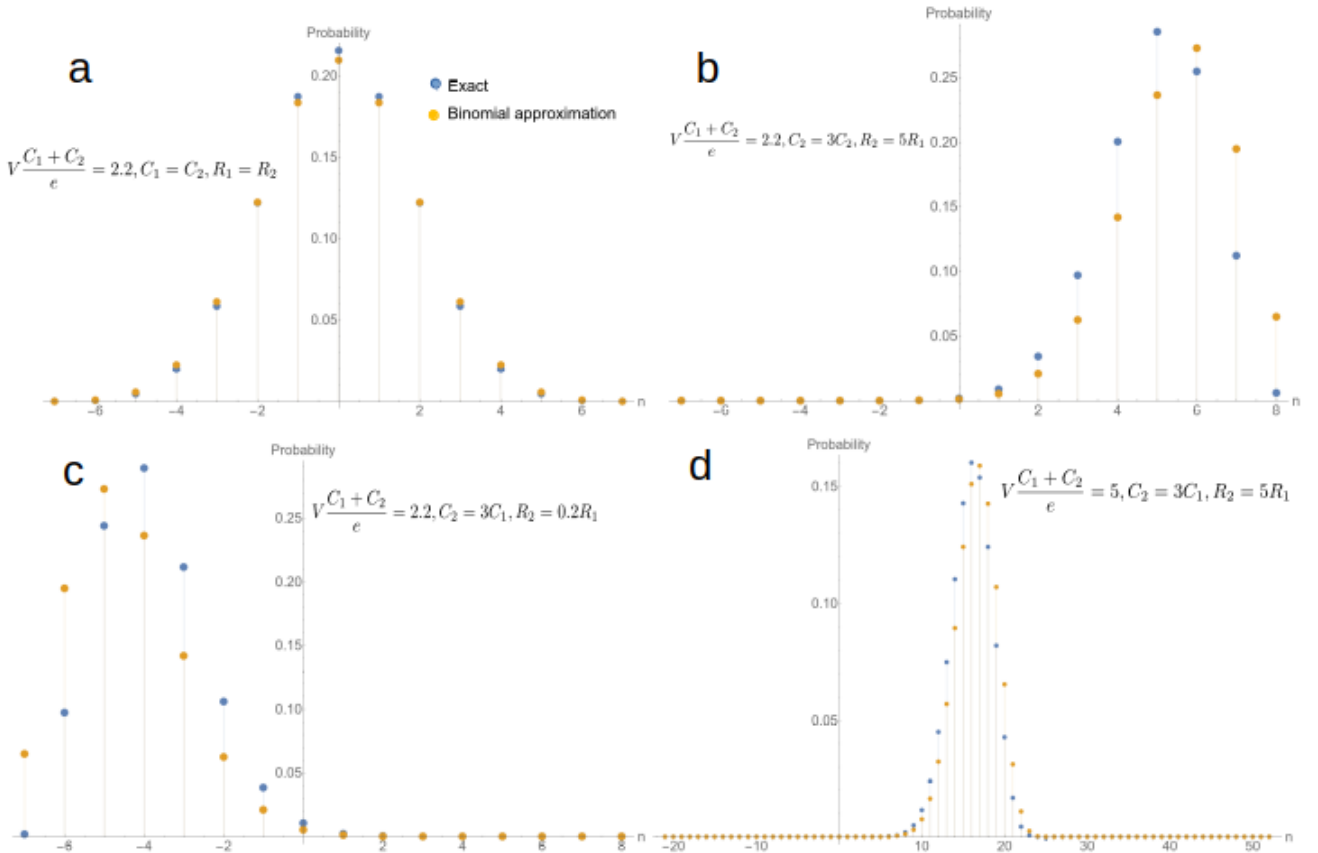


Figure A.1: Fast relaxation probability function. Exact solution and binomial approximation of the fast relaxation probability function, for different parameters. (a) For symmetric system (equal capacitance and resistance on both junctions), the probability function is symmetric. (b) For large resistance on the right side, the probability function is skewed to the right. (c) For large resistance on the left side, the probability function is skewed to the left. (d) For large voltage, the probability function resembles the binomial approximation. **Mutual parameters:** $C_G = 2C_1, V_L = -V_R = V/2, \phi \frac{C_1 + C_2}{e} = 0.5$.

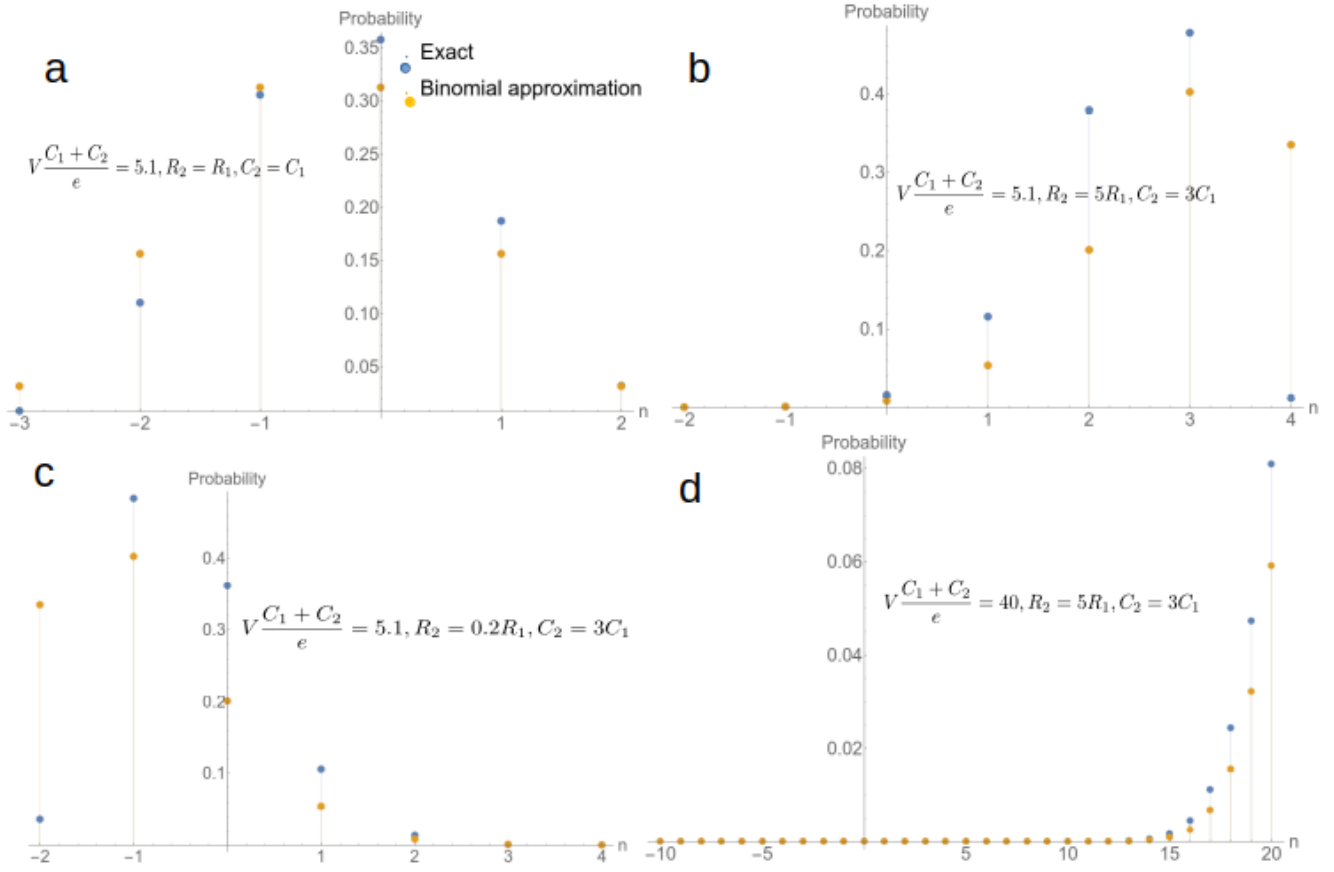


Figure A.2: Slow relaxation probability function. Exact solution and binomial approximation of the slow relaxation probability function, for different parameters. (a) For symmetric system (equal capacitance and resistance on both junctions), the probability function is symmetric. (b) For large resistance on the right side, the probability function is skewed to the right. (c) For large resistance on the left side, the probability function is skewed to the left. (d) For large voltage, the probability function resembles the binomial approximation.

Mutual parameters: $C_G = 2C_1$, $V_L = -V_R = V/2$, $\phi \frac{C_1+C_2}{e} = 0.5$.

Solution for special V, Q_G values

There are special values of V and Q_G for which the probability function is binomial. This is the case for

$$\alpha, \beta \in \mathbb{Z} \quad (\text{A.25})$$

In these cases $\alpha = n_{max}, \beta = -n_{min} + 1$ are whole numbers and we can write the probabilities as:

$$p(n) = p(n_{min}) \binom{n_{max} - n_{min}}{n - n_{min}} \left(\frac{R_2}{R_1}\right)^n \quad (\text{A.26})$$

Using binomial identities, we can sum up the probabilities to find $p(0)$:

$$\begin{aligned} 1 &= p(n_{min}) \sum_{n=n_{min}}^{n_{max}} \binom{n_{max} - n_{min}}{n - n_{min}} \left(\frac{R_2}{R_1}\right)^n = p(n_{min}) \left(\frac{R_2}{R_1}\right)^{n_{min}} \left(1 + \frac{R_2}{R_1}\right)^{n_{max} - n_{min}} \\ \Rightarrow p(n_{min}) &= \left(\frac{R_2}{R_1}\right)^{-n_{min}} \left(1 + \frac{R_2}{R_1}\right)^{-n_{max} + n_{min}} \end{aligned} \quad (\text{A.27})$$

so now we can write the probability explicitly

$$p(n) = \binom{n_{max} - n_{min}}{n - n_{min}} \frac{\left(\frac{R_2}{R_1}\right)^{n - n_{min}}}{\left(1 + \frac{R_2}{R_1}\right)^{n_{max} - n_{min}}} \quad (\text{A.28})$$

The random variable $n - n_{min}$ distribution is binomial with "success rate" $p = \frac{R_2}{R_1 + R_2}$ and "number of trials" $N = n_{max} - n_{min}$.

Solution for small voltages

For $0 < V < \frac{e}{C_1 + C_2}$ the system has a maximum of 2 occupation states, since $\Delta n \equiv n_{max} - n_{min} < 2$. In that case, the solution to eq. A.22 takes a simple form. For $\Delta n = 0$:

$$p(n_{min}) = 1 \quad (\text{A.29})$$

and for $\Delta n = 1$:

$$\begin{aligned} p_{slow}(n) &= \begin{cases} \left[\frac{R_2}{R_1} \left(\frac{V(C_1+C_2)}{\frac{e}{2} + ne + Q_G + C_1 V} - 1 \right) + 1 \right]^{-1} & n = n_{min} \\ \left[\frac{R_1}{R_2} \left(\frac{V(C_1+C_2)}{\frac{e}{2} - ne - Q_G + C_2 V} - 1 \right) + 1 \right]^{-1} & n = n_{max} \end{cases} \\ p_{fast}(n) &= \begin{cases} \left[\frac{R_2}{R_1} \left(\frac{VC_\Sigma(C_1+C_2)+C_G}{\left(\frac{e}{2}+ne\right)(C_1+C_2)-\frac{e}{2}C_G+(Q_0+C_1V)C_\Sigma} - 1 \right) + 1 \right]^{-1} & n = n_{min} \\ \left[\frac{R_1}{R_2} \left(\frac{VC_\Sigma(C_1+C_2)+C_G}{\left(\frac{e}{2}-ne\right)(C_1+C_2)-\frac{e}{2}C_G-(Q_0-C_2V)C_\Sigma} - 1 \right) + 1 \right]^{-1} & n = n_{max} \end{cases} \end{aligned} \quad (\text{A.30})$$

A.2.4 Steady state current for fast relaxation

Using eq. A.19, we find a relation between the average tunneling rates:

$$\begin{aligned} \sum_{n=n_{min}}^{n_{max}} \Gamma^+(n) p(n) &= \sum_{n=n_{min}}^{n_{max}} p(n_{min}) \Gamma^+(n) \prod_{m=n_{min}}^{n-1} \frac{\Gamma^+(m)}{\Gamma^-(m+1)} = \\ \sum_{n=n_{min}}^{n_{max}} p(n_{min}) \Gamma^-(n+1) \prod_{m=n_{min}}^n \frac{\Gamma^+(m)}{\Gamma^-(m+1)} &= \sum_{n=n_{min}+1}^{n_{max}+1} p(n_{min}) \Gamma^-(n) \prod_{m=n_{min}}^{n-1} \frac{\Gamma^+(m)}{\Gamma^-(m+1)} = \\ \sum_{n=n_{min}}^{n_{max}} \Gamma^-(n) p(n) \end{aligned} \quad (\text{A.31})$$

where in the last equality we could ignore the term with $n = n_{max} + 1$, and add a term with $n = n_{min}$, since both equal zero (the former because $\Gamma^+(n_{max}) = 0$ and the latter because $\Gamma^-(n_{min}) = 0$). For

$T = 0, V > 0$ it yields

$$\sum_{n=n_{min}}^{n_{max}} \Gamma_1^+(n) p(n) = \sum_{n=n_{min}}^{n_{max}} \Gamma_2^-(n) p(n) \quad (\text{A.32})$$

This result matches our intuition about steady state current where, on average, there is no accumulation of charge in the system. The current is given by

$$I = e \sum_n p(n) \Gamma_1^+(n) = e \sum_n p(n) \Gamma_2^-(n) \quad (\text{A.33})$$

Using this equality, and the tunneling rates for $T = 0$ (eq. 2.3), we can write the current as

$$I(V) \frac{(R_1 + R_2)(C_1 + C_2)}{e} = V \frac{C_1 + C_2}{e} - 1 + \frac{C_1 + C_2}{e^2} [p_{n_{max}}(V) W_{n_{max}}^+(V) + p_{n_{min}}(V) W_{n_{min}}^-(V)] \quad (\text{A.34})$$

For fast relaxation

$$\begin{aligned} W_{n_{max}}^+(V) &= \frac{e^2}{C_1 + C_2} \left(\frac{1}{2} + n_{max} + \frac{Q_{n_{max}}}{e} - \frac{C_2 V}{e} \right) \\ W_{n_{min}}^-(V) &= \frac{e^2}{C_1 + C_2} \left(\frac{1}{2} - n_{min} - \frac{Q_{n_{min}}}{e} - \frac{C_1 V}{e} \right) \end{aligned} \quad (\text{A.35})$$

and we can calculate the current using eq. A.20,A.21. The current is plotted in fig. A.3. Both probabilities and works are continuous functions of V , as long as n doesn't change. n changes when $W_{n_{max/min}}$ approach 0 and, after it does, $p_{n_{max/min}}$ approaches 0 (see eq. A.20). Therefore, $W_{n_{max/min}} p_{n_{max/min}}$ are continuous functions of V , and so does the current. This shows that, in the fast relaxation case, the current has no hysteresis and no jumps.

For slow relaxation

$$\begin{aligned} W_{n_{max}}^+(V) &= \frac{e^2}{C_1 + C_2} \left(\frac{1}{2} + n_{max} + \frac{Q_G}{e} - \frac{C_2 V}{e} \right) \\ W_{n_{min}}^-(V) &= \frac{e^2}{C_1 + C_2} \left(\frac{1}{2} - n_{min} - \frac{Q_G}{e} - \frac{C_1 V}{e} \right) \end{aligned} \quad (\text{A.36})$$

and the current is a continuous function of Q_G , but not necessarily of V , since the steady state solution for Q_G might not be continuous as a function of V . We have found an expression for the steady state current as a function of V and Q_G . We are left with the task of calculating the steady state value of Q_G .

A.2.5 Steady-state gate charge and current for slow relaxation

In the slow relaxation limit, Q_G relaxes according to the steady state probability. Let $\langle \cdot \rangle_{Q_G}$ be the average of a variable with respect to the steady state probability (which is Q_G dependent). The steady state Q_G is realized when $\langle Q_n \rangle_{Q_G} = Q_G$ (see eq. A.4) calculating the average Q_n yields

$$\langle Q_n \rangle_{Q_G} = \frac{C_G}{C_\Sigma} \left(-C_1 V_L - C_2 V_R - \langle n \rangle_{Q_G} e + \phi(C_1 + C_2) \right) \quad (\text{A.37})$$

Equating $\langle Q_n \rangle_{Q_G}$ and Q_G is the same as equating the steady state average voltage on the island, $\langle U \rangle_{Q_G}$, and the voltage on the island, calculated using Kirchoff's laws. This would be more convenient, since

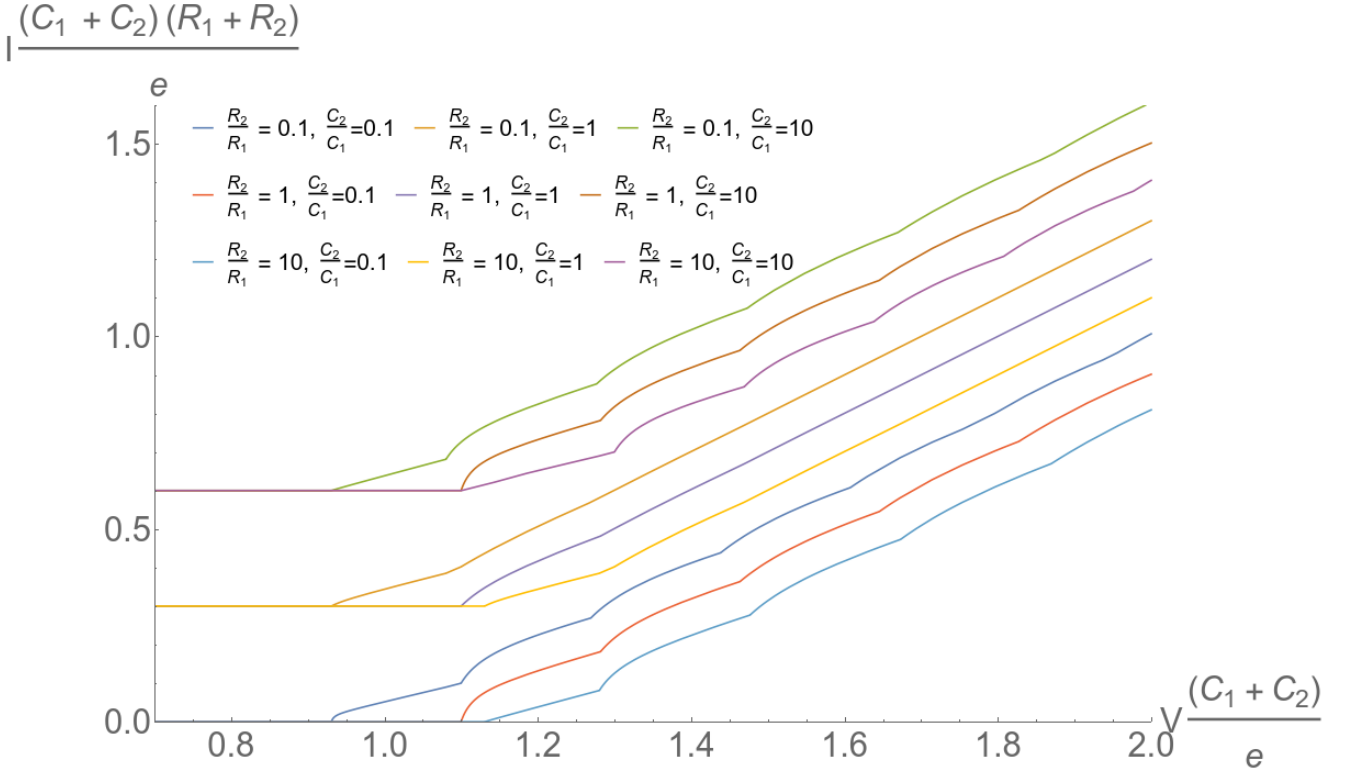


Figure A.3: Single island I-V curves for fast relaxation. Curves are shifted upwards by 0.3 for different resistance, and right by 0.1 for different capacitance, with respect to each other. **Mutual parameters:** $C_2 = C_G = 2C_1$, $V_L = -V_R = V/2$, $\phi \frac{C_1+C_2}{e} = 0.5$.

$\langle U \rangle_{Q_G}$ is a periodic function of Q_G . We are looking for Q_G such that

$$\phi - \frac{Q_G}{C_G} = \langle U \rangle_{Q_G} = \frac{C_1 V_L + C_2 V_R + Q_G + \langle n \rangle e}{C_1 + C_2} \quad (\text{A.38})$$

Binomial approximation

For the case when eq. (A.25) is satisfied, we can use eq. (A.28) to calculate $\langle U \rangle_{Q_G}$. Using eq. (A.28), we can calculate $\langle n \rangle_{Q_G}$ explicitly, as the average of a binomial distribution:

$$\langle n \rangle_{Q_G} = \frac{V}{e} \frac{R_2 C_2 - R_1 C_1}{R_2 + R_1} + \frac{1}{2} \frac{R_1 - R_2}{R_2 + R_1} - \frac{Q_G}{e} \quad (\text{A.39})$$

In the special cases of eq. (A.25), $\langle n \rangle_{Q_G}$ has a simple linear dependence on V and Q_G . In those cases $\langle U \rangle_{Q_G}$, would be Q_G independent

$$\langle U \rangle_{Q_G} = V \frac{R_2 C_2 - R_1 C_1}{(C_1 + C_2)(R_2 + R_1)} + \frac{C_1 V_L + C_2 V_R}{C_1 + C_2} - \frac{e}{2} \frac{R_2 - R_1}{(C_1 + C_2)(R_2 + R_1)} \quad (\text{A.40})$$

The steady state Q_G would be linear in V . This is a good approximation for large voltages ($V \gg \frac{e}{C_1 + C_2}$) as can be seen in fig. 4.2. For large voltages, the probabilities $p_{n_{max}}$, $p_{n_{min}}$ approaches 0, and eq. A.34 would give Ohmic conduction

$$I(V) \approx \frac{V}{R_1 + R_2} \quad (\text{A.41})$$

Small voltages

For small voltages, $V < \frac{e}{C_1 + C_2}$, we can use eq. A.30 to find

$$\langle U \rangle_{Q_G} = \frac{(n_{min} + \sigma) e + Q_G + V_L C_1 + V_R C_2}{C_1 + C_2} \quad (A.42)$$

$$\sigma \equiv \Delta n R_2 \frac{C_2 V - Q_G - n_{min} e - \frac{e}{2}}{(Q_G + n_{min} e + \frac{e}{2})(R_1 - R_2) + V(C_1 R_1 + C_2 R_2)}$$

Exploiting the periodicity of $\langle U \rangle_{Q_G}$ (see explanation in chapter 4), we can calculate it only for $-C_1 V - e/2 < Q_G < -C_1 V + e/2$ and $n_{min} = 0$, and get the solution for any Q_G

$$n_{min} + \sigma = \begin{cases} -l + R_2 \frac{C_2 V - Q_G + le - \frac{e}{2}}{(Q_G - le + \frac{e}{2})(R_1 - R_2) + V(C_1 R_1 + C_2 R_2)} & -C_1 V - \frac{e}{2} + le \leq Q_G < C_2 V - \frac{e}{2} + le \\ -l & C_2 V - \frac{e}{2} + le \leq Q_G < -C_1 V + \frac{e}{2} + le \end{cases} \quad (A.43)$$

where l is a whole number. Notice that σ (and thus also $\langle U \rangle_{Q_G}$) is a continuous function of Q_G . We can also calculate the current as a function of Q_G using 3.7

$$I(V, Q_G) = \begin{cases} \frac{1}{C_1 + C_2} \left(\frac{R_2}{C_1 V + \frac{e}{2} - le + Q_G} + \frac{R_1}{C_2 V - \frac{e}{2} + le - Q_G} \right)^{-1} & -C_1 V - \frac{e}{2} + le \leq Q_G < C_2 V - \frac{e}{2} + le \\ 0 & C_2 V - \frac{e}{2} + le < Q_G < -C_1 V + \frac{e}{2} + le \end{cases} \quad (A.44)$$

Looking at fig. 4.2, we see that eq. A.38 can have more than one solution if $C_G > \left(\max_{Q_G} \left[-\frac{dU}{dQ_G} \right] \right)^{-1}$. The minimal derivative would be obtained for the minimal(maximal) $\langle U \rangle_{Q_G}$, if $R_2 > R_1$ ($R_1 > R_2$), and the following Q_G values

$$Q_G = \begin{cases} C_2 V - \frac{e}{2} & R_2 > R_1 \\ -C_1 V - \frac{e}{2} & R_2 < R_1 \end{cases} \quad (A.45)$$

and is given by

$$\left(\max_{Q_G} \left[-\frac{\partial \langle U \rangle_{Q_G}}{\partial Q_G} \right] \right)^{-1} = (C_1 + C_2) \left[\frac{1}{1 - \frac{R_{min}}{R_{max}} \frac{(C_1 + C_2)V}{e}} - 1 \right] \quad (A.46)$$

where $R_{max} = \max[R_1, R_2]$, $R_{min} = \min[R_1, R_2]$. As the ratio between resistances becomes larger, we will get hysteresis for lower C_G values. Notice that this solution would be a good approximation also for $V > \frac{e}{C_1 + C_2}$ if $R_{max}/R_{min} \gg 1$, when the probability is skewed towards the highest or lowest occupation states. In that case, we will need to replace $(C_1 + C_2)V/e$ by $(C_1 + C_2)V/e - \lfloor (C_1 + C_2)V/e \rfloor$.

Not every solution to eq. A.38 is a stable solution for Q_G . To find which solutions are stable, we use the Lyapunov functional method. This will also allow us to find the current numerically.

Lyapunov Functional

Lyapunov functional is any functional that is monotonically decreasing with respect to time. In our case, we can define it as

$$L[Q_G] = \int_{Q_{min}}^{Q_G} dQ'_G \sum_n p_n(Q'_G) (Q'_G - Q_n) \quad (A.47)$$

where Q_{min} is an arbitrary value, smaller than the values we are interested in for Q_G . Differentiating with respect to time

$$\begin{aligned}\delta L [Q_G] &= \sum_n p_n (Q_G) (Q_G - Q_n) \delta Q_G \Rightarrow \\ \frac{dL [Q_G]}{dt} &= \sum_n p_n (Q_G) (Q_G - Q_n) \frac{dQ_G}{dt} = -\frac{1}{\tau} \sum_n p_n (Q_G) (Q_G - Q_n)^2 < 0\end{aligned}\quad (\text{A.48})$$

So L is indeed a monotonically decreasing function of time. The local minima of L with respect to Q_G are stable steady state solutions, L second derivative should be positive at these points

$$0 < \frac{\delta^2 L [Q_G]}{\delta Q_G} = 1 - \frac{\partial \langle Q_n \rangle_{Q_G}}{\partial Q_G} = 1 + \frac{C_G (C_1 + C_2)}{C_\Sigma} \frac{\partial \langle U \rangle_{Q_G}}{Q_G} \Rightarrow \left(\frac{\partial \langle U \rangle_{Q_G}}{\partial Q_G} \right) > -\frac{1}{C_G} \quad (\text{A.49})$$

Looking at fig. 4.2, we see that the i 'th smallest solution to eq. A.38 is stable if i is odd, and unstable if i is even. L is plotted for several cases in fig. A.4.

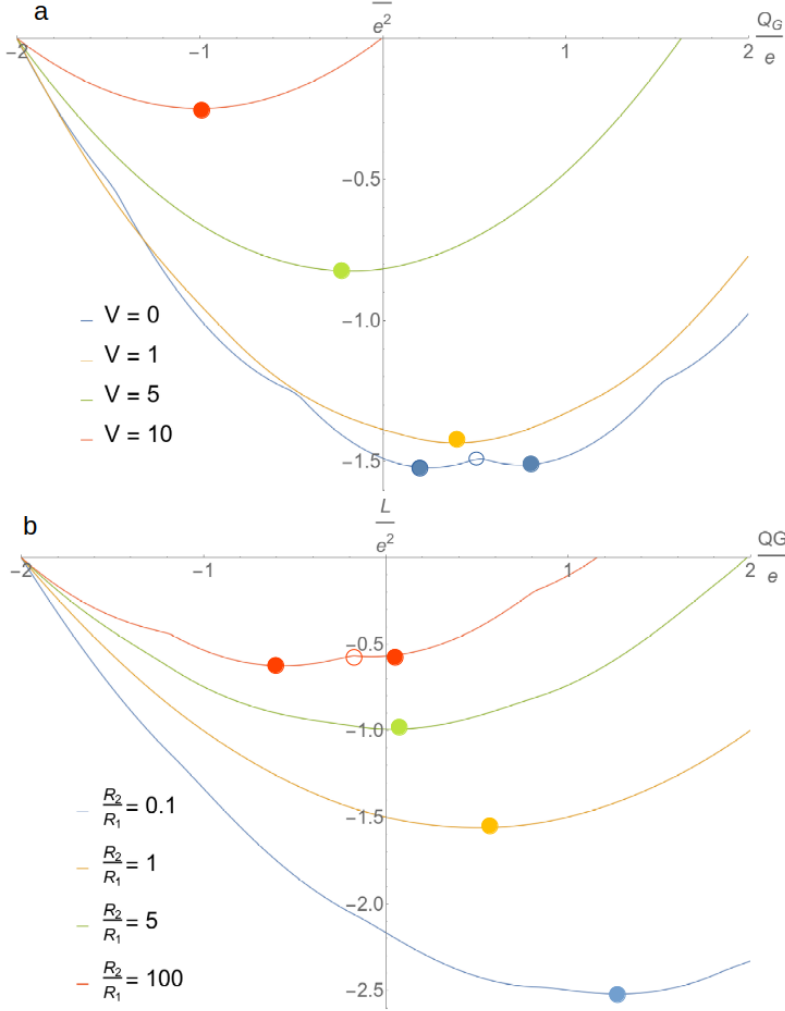


Figure A.4: Lypunov functional for different voltages (a) and resistances (b). Stable steady state solutions of eq. A.38 are marked with a whole circle, unstable with an empty circle. (a) As V increases, the functional becomes more "smooth" (as a function of Q_G) and there are less local minima. (b) As the resistances ratio, R_2/R_1 , increases, more local minima start to appear. **Mutual parameters:** $C_2 = C_G = 2C_1$, $V_L = -V_R = V/2$, $\phi \frac{C_1 + C_2}{e} = 0.5$, $Q_{min}/e = -2$. (a) $R_2 = 2R_1$ (b) $V(C_1 + C_2)/e = 2$.

Back to the analysis of the small V case, to get hysteresis for low V in the $I - V$ curve we need the stable solutions to conduct, i.e. the steady state Q_G should satisfy $-C_1 V - \frac{e}{2} + le \leq Q_G < C_2 V - \frac{e}{2} + le$.

For $R_1 = R_2$ the derivative takes the form

$$\frac{\partial \langle U \rangle_{Q_G}}{\partial Q_G} = \begin{cases} \frac{1}{C_1+C_2} \left(1 - \frac{e}{V(C_1+C_2)} \right) & -C_1 V - \frac{e}{2} + le \leq Q_G < C_2 V - \frac{e}{2} + le \\ \frac{1}{C_1+C_2} & C_2 V - \frac{e}{2} + le \leq Q_G < -C_1 V + \frac{e}{2} + le \end{cases} \quad (\text{A.50})$$

which means that for hysteresis we need $C_G > \left(\frac{e}{V(C_1+C_2)} - 1 \right)^{-1}$ and the stable solutions will come only from the raising part of $\langle U \rangle_{Q_G}$, which are non-conducting solutions. Therefore we won't get any hysteresis for $R_1 = R_2$ in low voltages.

General Case

In the general case, we can use A.20 and solve eq. A.38 numerically (using gradient descent for L). The resulting $I - V$ curves are plotted in fig 4.3. We see that hysteresis is more significant for large R_{max}/R_{min} and C_G .

A.2.6 Current jumps for slow relaxation

As discussed earlier, eq. A.34 shows that the current is a continuous function of Q_G , and current jumps can occur only when Q_G jumps. This happens only when there is more than one steady state solution for Q_G . Then, when V changes, one of the solutions ceases to be a steady state solution, and Q_G jumps to the next stable solution. This means that, for a single island, hysteresis and jumps always come together. We already saw the condition for hysteresis, this is also the condition for current jumps.

We would now like to estimate the separation and magnitude of the jumps. To do that, we look at figure 4.2. When increasing the voltage, a jump will occur when Q_G matches the minimal (maximal) value of $\langle U \rangle_{Q_G}$ for $R_2 > R_1 (R_1 > R_2)$. Those values are given in eq. A.45. For large V , the value of $\langle U \rangle_{Q_G}$ at these points is approximately given by the binomial approximation A.40 (as can be seen in fig. 4.2). For small V , we can use eq. A.42 to find

$$\begin{aligned} \langle U \rangle_{max} &= \frac{e/2}{C_1 + C_2} - V_R \text{ for } R_1 > R_2 \\ \langle U \rangle_{min} &= V_L - \frac{e/2}{C_1 + C_2} \text{ for } R_2 > R_1 \end{aligned} \quad (\text{A.51})$$

There are two kinds of jumps. The first occurs when the linear function $\phi - \frac{Q_G}{C_G}$ intersects with the minimum(maximum) of $\langle U \rangle_{Q_G}$ for $R_2 > R_1 (R_1 > R_2)$, the second is when the two functions are tangent. The first kind occurs when $R_2 > R_1 (R_1 > R_2)$ and the occupation increases(decreases), this occurs naturally when the voltages is increased symmetrically ($V_L = -V_R = V/2$). Therefore, in this case, jumps from the first kind occur when the voltage increases, and from the second kind when it decreases. If the voltage doesn't increase symmetrically, we can get jumps from the first kind also when V_R is decreased(V_L is increased) for $R_2 > R_1 (R_1 > R_2)$. Say that $R_2 > R_1$ and a jump from the first kind had just occurred, we know that the linear function $\phi - \frac{Q_G}{C_G}$ is intersecting with $\langle U \rangle_{Q_G}$ at one of its minima. The next jump will occur when the next minimum (one minimum to the left of the intersecting one) will intersect with the linear function. Changing $V_{R/L}$ by $\Delta V_{R/L}$, each minimum moves right by $C_2 \Delta V$ and up by $\Delta U = \frac{\Delta V_L R_2 + \Delta V_R R_1}{R_1 + R_2}$. Since the distance between minima is e , we know that the next

intersection will occur when $\Delta U = \frac{e - C_2 \Delta V}{C_G}$ (see geometrical explanation in fig. A.5a). From here, we can find the jump separation. It depends on the way external voltages are changed. Using the same method, we get the separation for $R_1 > R_2$. The results are

$$\Delta V_L \approx \begin{cases} \frac{e}{C_G \frac{R_2}{R_1+R_2} + C_2} & R_2 > R_1 \\ \frac{e}{|C_G \frac{R_2}{R_1+R_2} - C_1|} & R_1 > R_2 \end{cases}, \quad \Delta V_R \approx \begin{cases} \frac{e}{|C_G \frac{R_1}{R_1+R_2} - C_2|} & R_2 > R_1 \\ \frac{e}{C_G \frac{R_1}{R_1+R_2} + C_1} & R_1 > R_2 \end{cases}, \quad \Delta V \approx \begin{cases} \frac{e}{\frac{C_G}{2} \frac{R_2 - R_1}{R_1+R_2} + C_2} & R_2 > R_1 \\ \frac{e}{\frac{C_G}{2} \frac{R_1 - R_2}{R_1+R_2} + C_1} & R_1 > R_2 \end{cases} \quad (\text{A.52})$$

Where $\Delta V_L(\Delta V_R)$ is for the case when $V_R(V_L)$ is held constant and ΔV is for the case where both are changed symmetrically, $V_L = -V_R = V/2$. This approximation will be more accurate for large resistance ratio, since then the solution for small V holds approximately also for large voltages. We can use the same approximation for the voltage separation between jumps from the second kind.

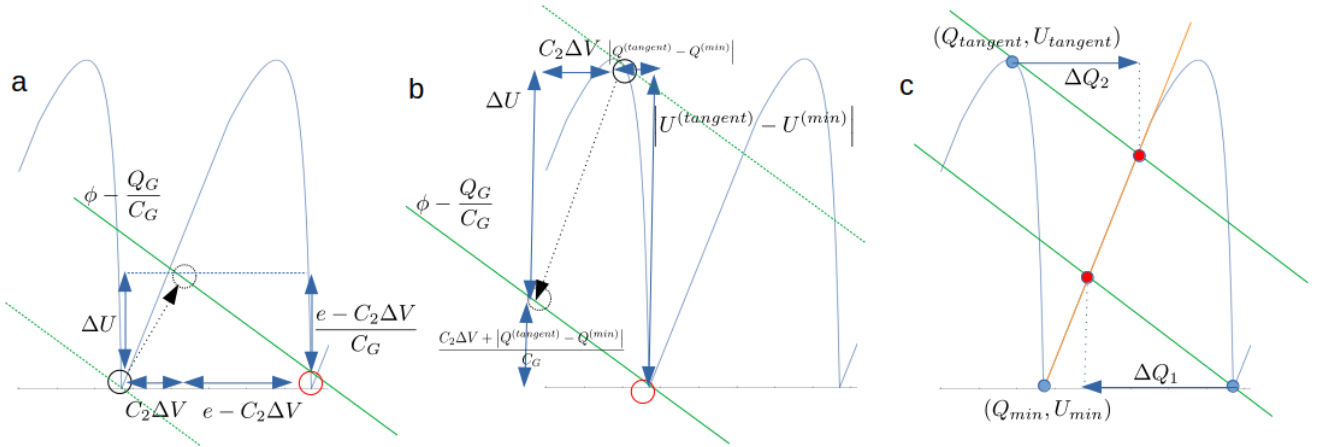


Figure A.5: Geometrical approximation for jump separation and height, for $R_2 > R_1$. (a) For increasing voltage, a jump occurs when a minimum of $\langle U \rangle_{Q_G}$ (blue curve) intersects with $\phi - Q_G/C_G$ (line marked in green, intersection in red circle). When the voltage is increased after a jump, the average voltage minima moves right and up. The next jump occurs when the next minimum (black circle) intersects with this linear function (dotted black circle). (b) When an upwards jump occurs, solution jumps from the intersection with the minimum of $\langle U \rangle_{Q_G}$ (red circle) to the next intersection (black dotted circle). When the voltage is decreased afterwards, a downwards jump occurs when the point where $\langle U \rangle_{Q_G}$ (blue curve) and $\phi - Q_G/C_G$ (green line) are tangent (black circle). (c) The change in Q_G when a jump occurs can be approximated for small voltages. In a jump from the first kind Q_G jumps by ΔQ_1 , from a minimum of $\langle U \rangle_{Q_G}$ (blue curve) to the intersection of $\phi - Q_G/C_G$ (green line). The intersection occurs in the part where $\langle U \rangle_{Q_G}$ is linear (marked with orange line) and has a slope of $1/(C_+ C_2)$. In a jump from the second kind it jumps from the tangent point to the same line, by ΔQ_2 .

In fig. A.6 this approximation is compared with the numerical results. The agreement is very good for increasing voltage, and less accurate for decreasing, as expected.

Say we stop increasing the voltage right after a jump, and start decreasing it back again. What is the separation between the upwards and downwards jumps? For $R_2 > R_1$, when $V_{L/R}$ is decreased by $\Delta V_{L/R}$ the graph of $\langle U \rangle_{Q_G}$ moves left and down (see fig. 4.2b), a jump downwards will occur when $\phi - \frac{Q_G}{C_G}$ would be tangent to $\langle U \rangle_{Q_G}$. An approximation for that separation can be obtained using the

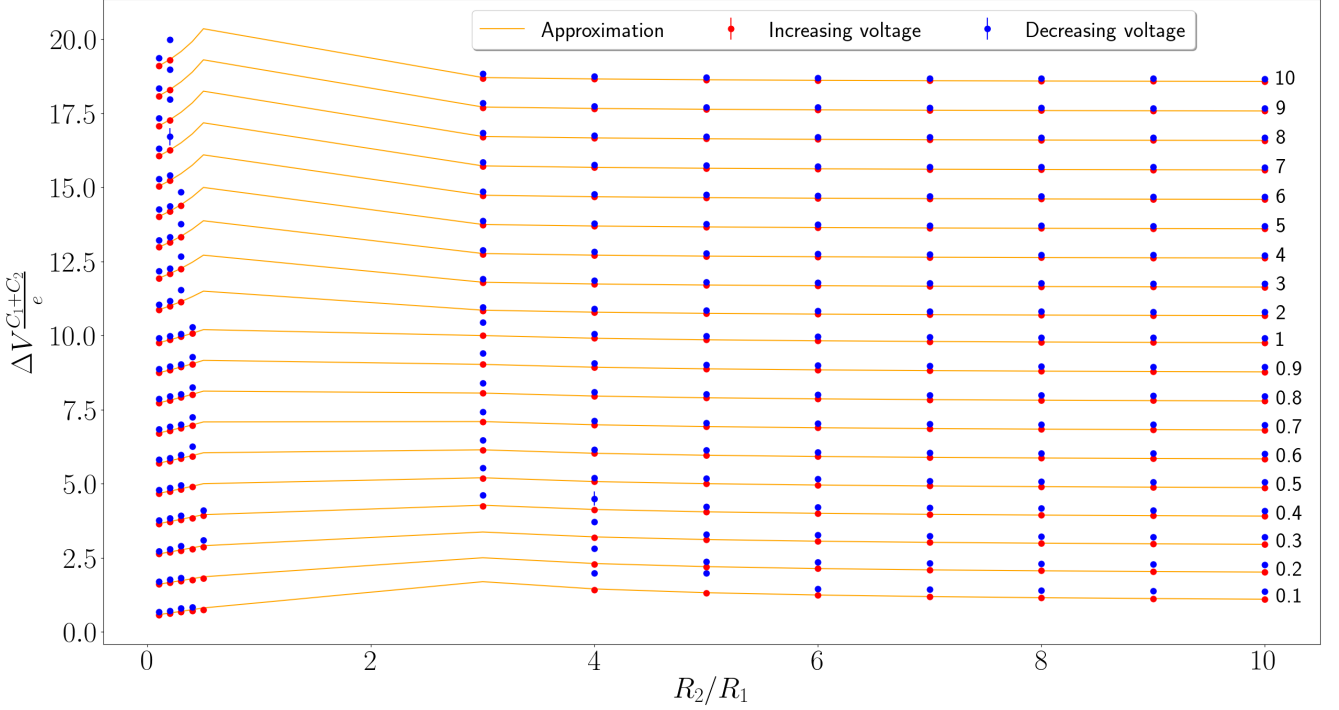


Figure A.6: Single island jumps separation. Average separation between consecutive jumps as a function of R_2/R_1 , for different values of C_2/C_1 , which are indicated to the left of each curve. Curves are shifted upwards by 1 with respect to each other. The analytical approximation (orange line) agrees with the numerical results for upward jumps (red dots). The approximation is less accurate for downward jumps (blue dots) which are usually further apart from each other. Only results where jumps were detected are shown.

Common parameters: $\phi = 0.5e/(C_1 + C_2)$, $C_G = 2(C_1 + C_2)$, $V_{max} = 4e/(C_1 + C_2)$.

small voltage solution for $\langle U \rangle_{Q_G}$ (eq. A.42). We use it to find the point where $\partial \langle U \rangle_{Q_G} / \partial Q_G = -1/C_G$:

$$\begin{aligned} Q_G^{tangent} &\approx V \frac{C_1 R_1 + C_2 R_2}{R_2 - R_1} - \frac{e}{2} - \frac{1}{R_2 - R_1} \sqrt{\frac{(C_1 + C_2) C_G R_1 R_2 V e}{C_\Sigma}} \\ \langle U \rangle_{Q_G}^{(tangent)} &\approx \frac{1}{R_2 - R_1} \left[\frac{e/2}{C_1 + C_2} (R_1 + R_2) + R_2 V_L - R_1 V_R - \sqrt{\frac{e R_1 R_2 V}{(C_1 + C_2) C_G C_\Sigma}} (C_2 + C_1 + 2C_G) \right] \end{aligned} \quad (\text{A.53})$$

Using simple geometrical consideration (see fig. A.5b), we find an approximation for $R_2 > R_1$. In the same way we can also find an approximation for $R_1 > R_2$. The results are:

$$\Delta V_{\uparrow\downarrow} \approx \Delta V \times \begin{cases} \frac{C_G/e}{R_2 - R_1} \left[\frac{e R_2}{C_1 + C_2} + \frac{C_\Sigma R_1}{C_G} V_\downarrow - 2 \sqrt{\frac{e R_1 R_2 V_\downarrow C_\Sigma}{(C_1 + C_2) C_G}} \right] & R_2 > R_1 \\ \frac{C_G/e}{R_1 - R_2} \left[\frac{e R_1}{C_1 + C_2} + \frac{C_\Sigma R_2}{C_G} V_\downarrow - 2 \sqrt{\frac{e R_1 R_2 V_\downarrow C_\Sigma}{(C_1 + C_2) C_G}} \right] & R_1 > R_2 \end{cases} \quad (\text{A.54})$$

where V_\downarrow is the voltage when downwards jump had happen. When $\Delta V \leq \Delta V_{\uparrow\downarrow}$ there will be one big hysteresis loop (see fig. 4.3a). When $\Delta V > \Delta V_{\uparrow\downarrow}$, we will get few loops, one for each upwards jump (see fig. 4.3c). This approximation is valid for $V < e/(C_1 + C_2)$, we see in fig. 4.3 that this separation becomes smaller as V increases. Therefore, we will get smaller separation and smaller hysteresis loops for larger V . A comparison between this approximation and the numerical results is plotted in fig. A.7.

We see a good agreement for big resistance disorder, and a fair one for small.

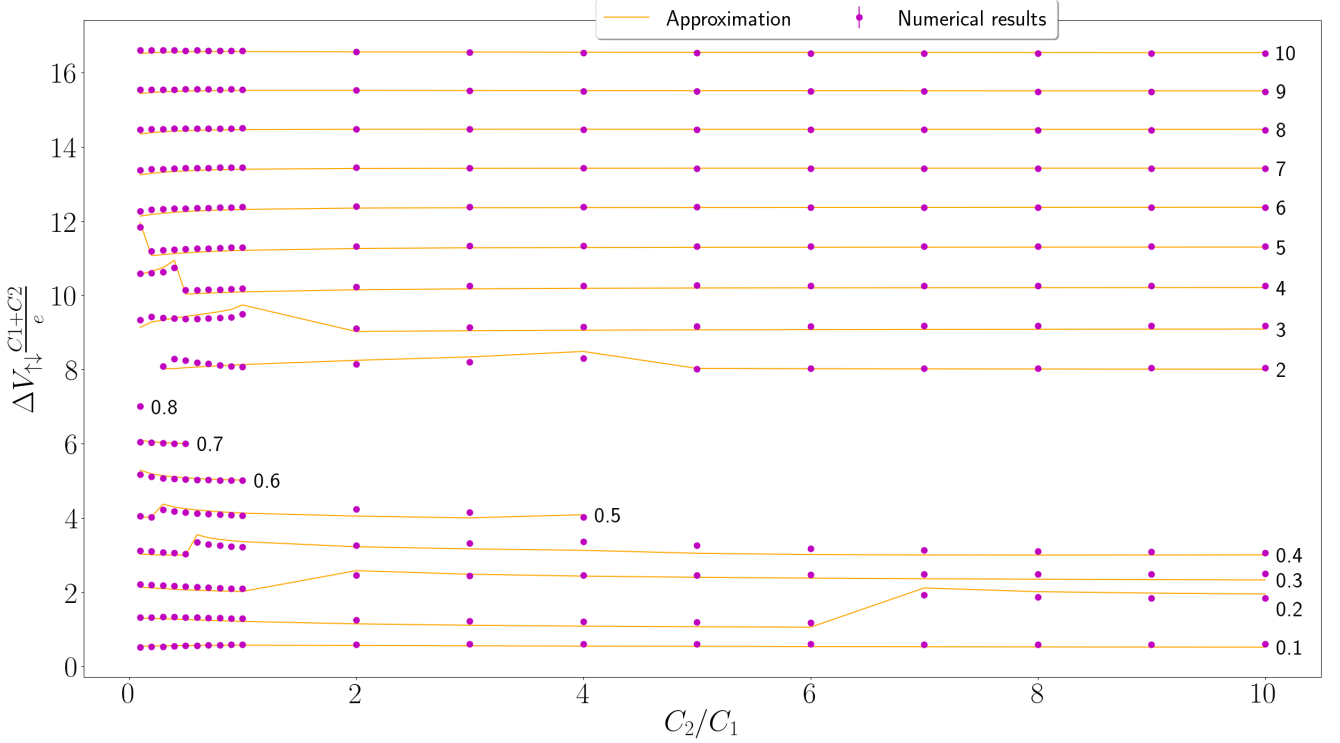


Figure A.7: Separation between upwards and downwards jumps, for the first hysteresis loop, as a function of C_2/C_1 for different value of R_2/R_1 , which are indicated to the right of each curve. Curves are shifted upwards by 1 with respect to each other. For big resistance ratios, analytical approximations match the numerical results. It becomes less accurate for $R_1 \sim R_2$. Only results where a jump was detected are shown. The discontinuities in the curves are caused by a changes in the voltage where downwards jump has occurred.

Common parameters: $\phi = 0.5e / (C_1 + C_2)$, $C_G = 2(C_1 + C_2)$, $V_{max} = 4e / (C_1 + C_2)$.

We can approximate the jump height in a similar way. For small V , the raising part of $\langle U \rangle_{Q_G}$ is approximately linear (see eq. A.42) with slope of $1 / (C_1 + C_2)$. We use geometrical consideration (see fig. A.5c) to find the jump in Q_G . When Q_G changes, so does n , by $n \rightarrow n \pm 1$ (in the opposite direction to Q_G). Thus, we can approximate the height of a jump from the first and second kinds using eq. A.34:

$$\begin{aligned} \Delta I_1 &\approx \frac{e}{C_\Sigma (R_1 + R_2)} \\ \Delta I_2 &\approx \Delta I_1 \times \frac{C_\Sigma}{C_G (R_{max} - R_{min})} \left[\frac{R_{max}}{C_1 + C_2} - \sqrt{\frac{R_1 R_2 V_\downarrow C_\Sigma}{e C_G (C_1 + C_2)}} \right] \end{aligned} \quad (\text{A.55})$$

A comparison between this approximation and the numerical results is plotted in fig. A.8. We see a very good agreement for large resistance ratios. For smaller ratios, approximations become less accurate, especially for decreasing voltage (jumps from the second kind).

Using eq. A.54 and A.55, we can approximate the hysteresis loop area, in the case of separate loop for each upwards jump, as $\Delta I \Delta V_{\uparrow\downarrow}$. If we know the voltage where downwards jump occurred, we can calculate the voltages for all jumps, using eq. A.52 and estimate the total signed area under the $I - V$ curve, the approximated area compares nicely with numerical results, as shown in fig. A.9.

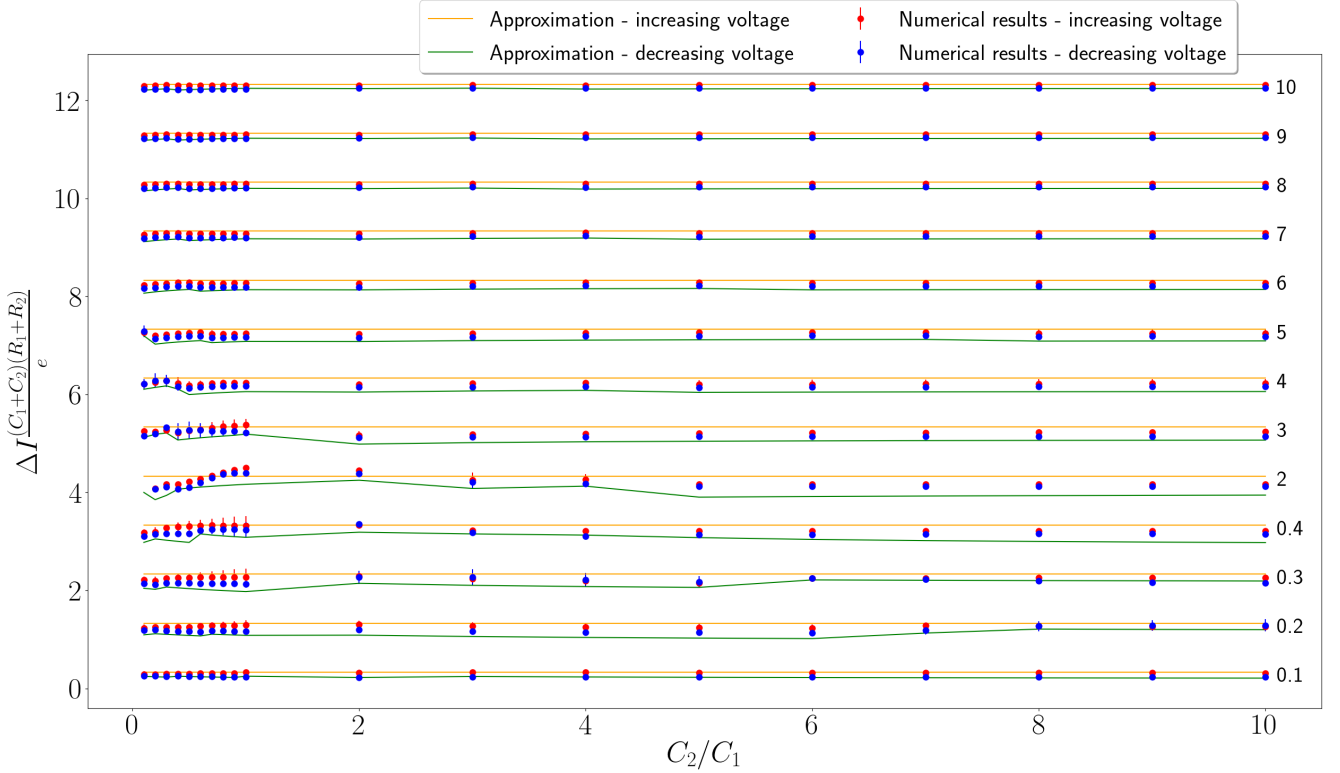


Figure A.8: Average jump height as a function of C_2/C_1 for different value of R_2/R_1 , which are indicated to the right of each curve. Curves are shifted upwards by 1 with respect to each other. The analytical approximation is in good agreement with numerical results for large resistance ratio. The upward jumps are slightly bigger than the downward jumps.

Common parameters: $\phi = 0.5e / (C_1 + C_2)$, $C_G = 2(C_1 + C_2)$, $V_{max} = 4e / (C_1 + C_2)$.

A.2.7 Threshold voltage

Assuming we start from $V = 0$ and increase the voltage slowly, such that the system can relax to its steady state for each V . Current will start flowing through the system when $n_{min} < n_{max}$. First, voltage increases until $n_{max} = n_{min}$. From eq. A.14, we see that this will happen for $V = V_{min}^{th} \equiv e \frac{C_G}{(C_1 + C_2)C_\Sigma}$ (except for the special case when $Q_0 \pm \frac{1}{2}$ is a whole number, than n_{min} jumps directly from $n_{max} - 1$ to $n_{max} + 1$). Let n_{ini} be n_{min} calculated for $V = V_{min}^{th}$. Conduction will happen when n_{min} decreases or n_{max} increases, whichever comes first. This gives us the following threshold voltage:

$$\begin{aligned}
 V_L^{th} &= \min \left[\frac{q^+}{C_2 + C_G}, \frac{q^-}{C_1} \right] \\
 V_R^{th} &= \min \left[\frac{q^+}{C_2}, \frac{q^-}{C_1 + C_G} \right] \\
 V^{th} &= \min \left[\frac{q^+}{C_2 + C_G/2}, \frac{q^-}{C_1 + C_G/2} \right] \\
 q^\pm &\equiv \pm (\phi C_G + e n_{ini}) + e \frac{C_\Sigma}{2(C_1 + C_2)}
 \end{aligned} \tag{A.56}$$

Where V_L^{th} is for the case $V_R = 0$ and V_L is increased, V_R^{th} is for the case $V_L = 0$ and V_R is decreased, V^{th} is for $V_L = -V_R = V/2$ and V is increased.

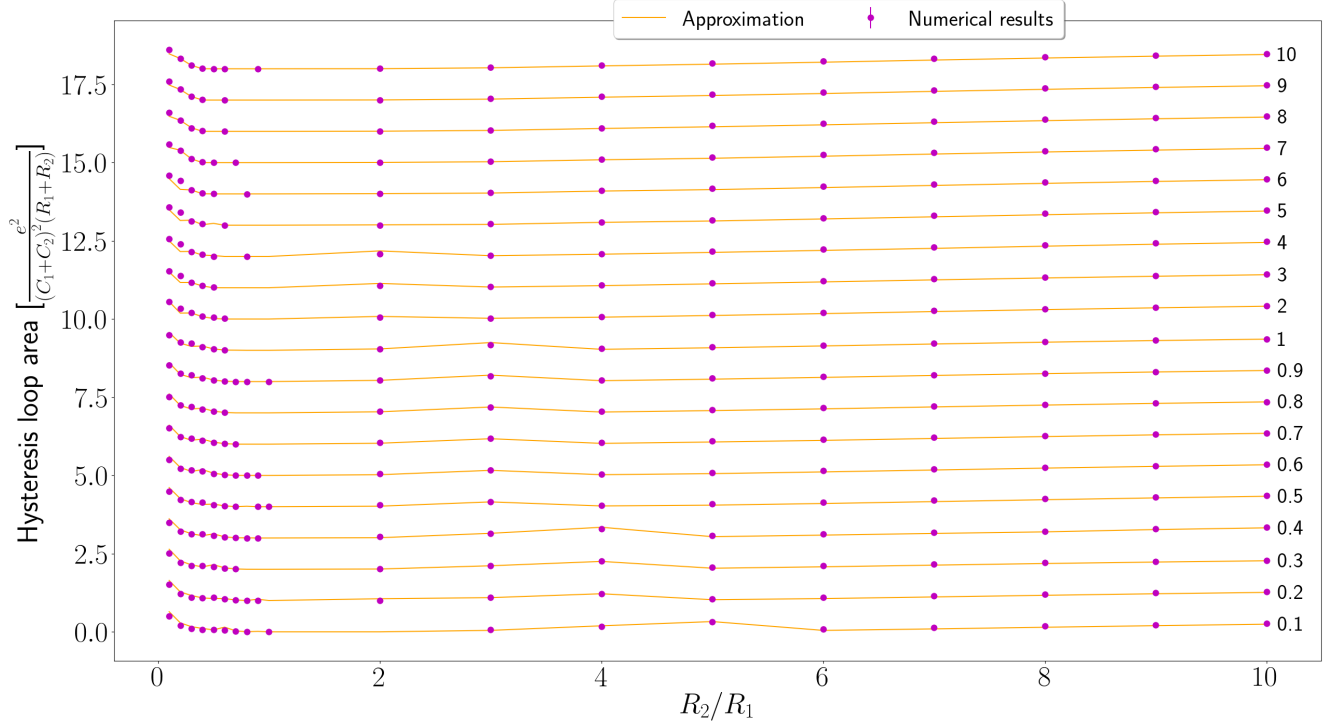


Figure A.9: The total signed area under the I-V curve as a function of R_2/R_1 for different value of C_2/C_1 , which are indicated to the right of each curve. Curves are shifted upwards by 1 with respect to each other. The analytical approximation is in good agreement with numerical results. **Common parameters:** $\phi = 0.5e/(C_1 + C_2)$, $C_G = 2(C_1 + C_2)$, $V_{max} = 4e/(C_1 + C_2)$.

For the slow relaxation case (eq. A.13) the situation is a bit more complicated. If the condition for hysteresis and jumps, eq. A.46, doesn't hold, we will get the same threshold as for the fast relaxation case (eq. A.56). n_{ini} would be chosen by the initial condition for Q_G . If the condition for hysteresis holds, we have more options. If $R_2 > R_1 (R_1 > R_2)$ and n_{max} increases first (n_{min} decreases first) it would result in a jump of Q_G . For $C_G < (C_1 + C_2) \left[\frac{e}{(C_1 + C_2)V} - 1 \right]^{-1}$ the jump would lead us to Q_G such that the system will conduct, and the threshold still remains as in eq. A.56. But, for larger C_G , the jump would cause an increase/decrease in both n_{min} and n_{max} . In this case, we need to repeat the calculation for this new n value. The maximum possible threshold value is $V_{max}^{th} = \frac{e}{C_1 + C_2}$, as can be seen from eq. A.13. Using the same condition, we see that the minimal threshold voltage is the same as for fast relaxation. For slow relaxation, an occupation change can occur for any V (unlike fast relaxation) but for $V < V_{min}^{th}$ it will cause a jump to a non-conducting state. In fig. A.10, a comparison with the numerical results is shown. Numerical results are in good agreement with the analytic calculation, except for few results for $R_1 \sim R_2$. In those, the maximal(minimal) value of $\langle U_{Q_G} \rangle$ for $R_2 > R_1 (R_1 > R_2)$ is smaller(bigger) than the value for which $d \langle U_{Q_G} \rangle / dQ_G = -1/C_G$. Therefore, we get jumps in the opposite direction to the one assumed when calculating the threshold voltage.

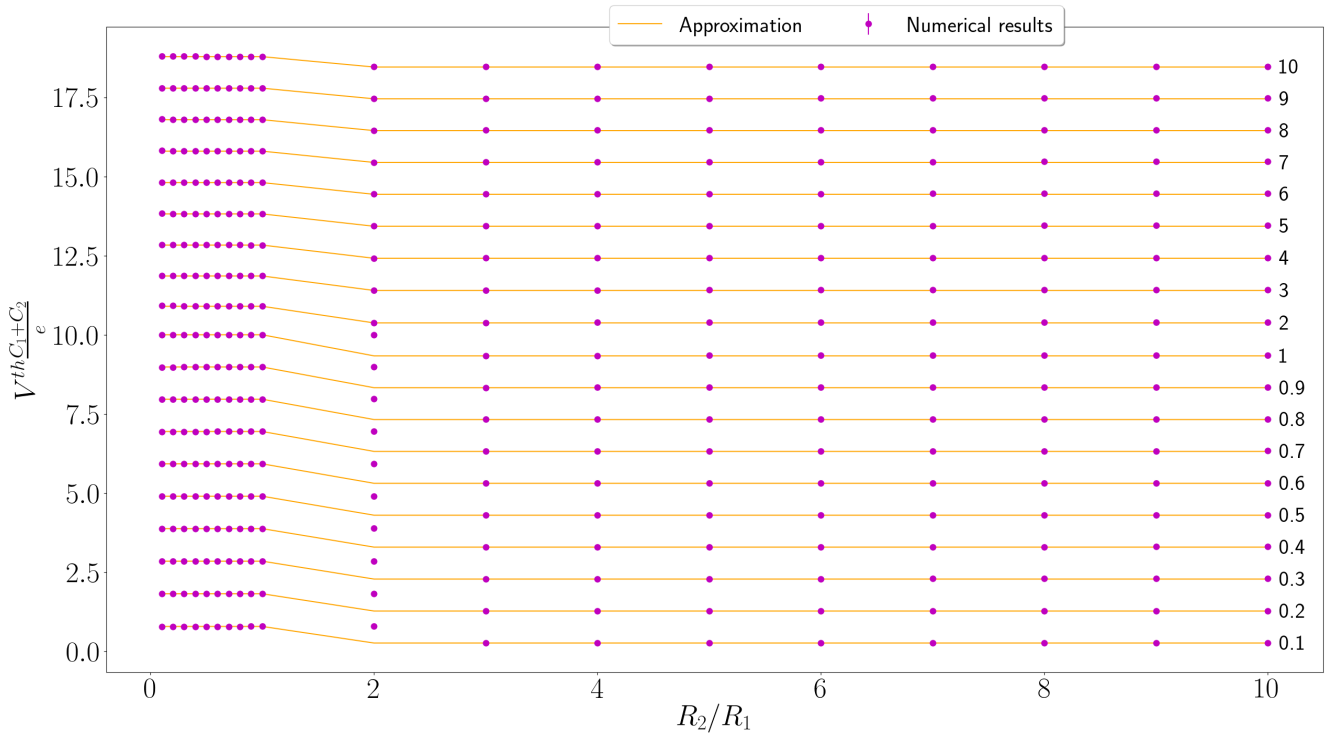


Figure A.10: Threshold voltage as a function of R_2/R_1 for different value of C_2/C_1 , which are indicated to the right of each curve. Curves are shifted upwards by 1 with respect to each other. The analytical result is in agreement with numerical results, except for few cases with $R_2 = 2R_1$. **Common parameters:** $\phi = 0.5e/(C_1 + C_2)$, $C_G = 2(C_1 + C_2)$, $V_{max} = 4e/(C_1 + C_2)$.

Appendix B

2 island arrays capacitance matrix

To understand better the interactions in an array, it is beneficial to get an exact solution for simple cases. Here we derive explicit expressions for the matrices that determine the interactions in the array, inverse capacitance matrix ($C_{i,j;k,l}^{-1}$) and the steady state capacitance matrix ($\sum_{k,l} C_{i,j;k,l}^{-1} \tau_{k,l;a,b}$). We will do this for the simple case when $R_{i,j}^G = R^G$ and $C_{i,j}^G = C_G$ are equal for all islands in the array. For this case, the steady state inverse capacitance matrix can be written as $(C_{i,j;k,l} + C_G \delta_{i,j;k,l})^{-1}$.

B.1 1X2 array

A schema of 1×2 array is plotted in fig. B.1. For this case, the capacitance matrix is

$$\mathbf{C} = \begin{pmatrix} C_1 + C_2 & -C_2 \\ -C_2 & C_2 + C_3 \end{pmatrix} \quad (\text{B.1})$$

and the inverse of it is

$$\mathbf{C}^{-1} = \begin{pmatrix} \left(C_1 + C_2 - \frac{C_2^2}{C_2 + C_3} \right)^{-1} & \left(C_1 + C_3 + \frac{C_1 C_3}{C_2} \right)^{-1} \\ \left(C_1 + C_3 + \frac{C_1 C_3}{C_2} \right)^{-1} & \left(C_2 + C_3 - \frac{C_2^2}{C_1 + C_2} \right)^{-1} \end{pmatrix} \quad (\text{B.2})$$

The inverse of the steady state capacitance matrix is given by

$$\mathbf{C}_{\text{steady-state}}^{-1} = \begin{pmatrix} \left(C_1 + C_2 + C_G - \frac{C_2^2}{C_2 + C_3 + C_G} \right)^{-1} & \left(C_1 + C_3 + 2C_G + \frac{(C_1 + C_G)(C_3 + C_G)}{C_2} \right)^{-1} \\ \left(C_1 + C_3 + 2C_G + \frac{(C_1 + C_G)(C_3 + C_G)}{C_2} \right)^{-1} & \left(C_2 + C_3 + C_G - \frac{C_2^2}{C_1 + C_2 + C_G} \right)^{-1} \end{pmatrix} \quad (\text{B.3})$$

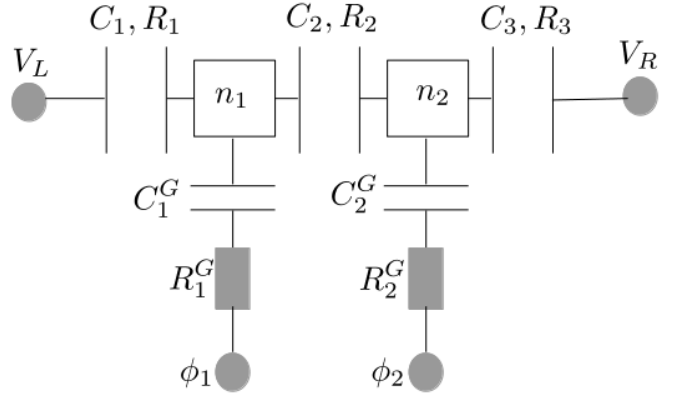


Figure B.1: Schematic drawing of a 1×2 array. C_i, R_i, Q_i are the capacitance, resistance (or tunneling resistance) and charge of the different components respectively. V_L, V_R, ϕ_i are the left, right and gate voltages respectively. C_i^G, R_i^G are the gate capacitance and resistance respectively.

B.2 2X1 array

A schema of 2×1 array is plotted in fig. B.1. For this case, the capacitance matrix is

$$\mathbf{C} = \begin{pmatrix} C_1 + C_2 + C' & -C' \\ -C' & C_3 + C_4 \end{pmatrix} \quad (\text{B.4})$$

and the inverse of it is

$$\mathbf{C}^{-1} = \begin{pmatrix} \left(C_1 + C_2 + C' - \frac{C'^2}{C_3 + C_4 + C'} \right)^{-1} & \left(C_1 + C_2 + C_3 + C_4 + \frac{(C_1 + C_2)(C_3 + C_4)}{C'} \right)^{-1} \\ \left(C_1 + C_2 + C_3 + C_4 + \frac{(C_1 + C_2)(C_3 + C_4)}{C'} \right)^{-1} & \left(C_3 + C_4 + C' - \frac{C'^2}{C_1 + C_2 + C'} \right)^{-1} \end{pmatrix} \quad (\text{B.5})$$

The inverse of the steady state capacitance matrix is given by

$$\mathbf{C}_{\text{steady-state}}^{-1} = \begin{pmatrix} \left(C_1 + C_2 + C' + C_G - \frac{C'^2}{C_3 + C_4 + C' + C_G} \right)^{-1} & \left(C_1 + C_2 + C_3 + C_4 + 2C_G + \frac{(C_1 + C_2 + C_G)(C_3 + C_4 + C_G)}{C'} \right)^{-1} \\ \left(C_1 + C_2 + C_3 + C_4 + 2C_G + \frac{(C_1 + C_2 + C_G)(C_3 + C_4 + C_G)}{C'} \right)^{-1} & \left(C_3 + C_4 + C' + C_G - \frac{C'^2}{C_1 + C_2 + C' + C_G} \right)^{-1} \end{pmatrix} \quad (\text{B.6})$$

B.3 Discussion

Examining these results, we can see some interesting features. The effective self capacitance, $1/C_{i,j;i,j}^{-1}$, is smaller than the self capacitance for all cases. Since the natural unit of the voltage over an island is 1 over the self capacitance, we expect an increase in all voltage values compared to a single island with the same self capacitance (i.e. threshold voltage, voltage separation between jumps, maximal voltage for hysteresis etc.). This can be understood also by examining the energy barrier that needs to be overcome for tunneling between an electrode and the i, j island (eq. 3.21). This barrier is given by $\frac{e^2}{2} C_{i,j;i,j}^{-1}$. The barrier is bigger for the 2×1 and 1×2 arrays, compared to the single island case. Thus, bigger voltage is needed. We can also calculate the barrier for tunneling between islands. For tunneling between island i, j and k, l it is given by $\frac{e^2}{2} \left(C_{i,j;i,j}^{-1} + C_{k,l;k,l}^{-1} - 2C_{i,j;k,l}^{-1} \right)$, which gives:

$$\Delta E = \frac{e^2}{2} \begin{cases} \left(C_2 + \frac{C_1 C_3}{C_1 + C_3} \right)^{-1} & 1 \times 2 \text{ array} \\ \left(C_2 + \frac{(C_1 + C_G)(C_3 + C_G)}{C_1 + C_3 + 2C_G} \right)^{-1} & 1 \times 2 \text{ array in steady state} \\ \left(C' + \frac{(C_1 + C_2)(C_3 + C_4)}{C_1 + C_2 + C_3 + C_4} \right)^{-1} & 2 \times 1 \text{ array} \\ \left(C' + \frac{(C_1 + C_2 + C_G)(C_3 + C_4 + C_G)}{C_1 + C_2 + C_3 + C_4 + 2C_G} \right)^{-1} & 2 \times 1 \text{ array in steady state} \end{cases} \quad (\text{B.7})$$

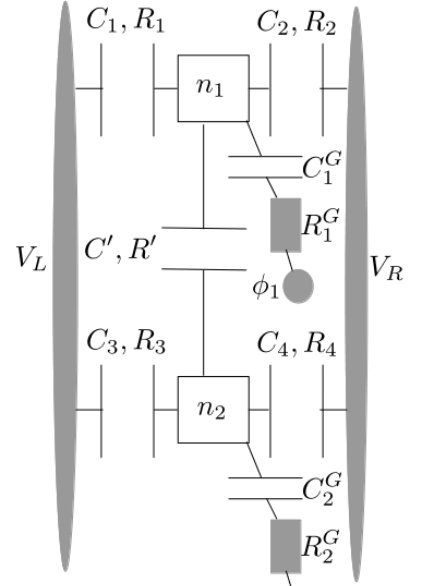


Figure B.2: Schematic drawing of a 2×1 array. C_i, R_i, Q_i are the capacitance, resistance (or tunneling resistance) and charge of the different components respectively. V_L, V_R, ϕ_i are the left, right and gate voltages respectively. C_i^G, R_i^G are the gate capacitance and resistance respectively.

The barrier is strongly dependent on the connecting junction's capacitance, it gets bigger as the connecting capacitance decreases.

Appendix C

Additional results

C.1 Gate capacitance

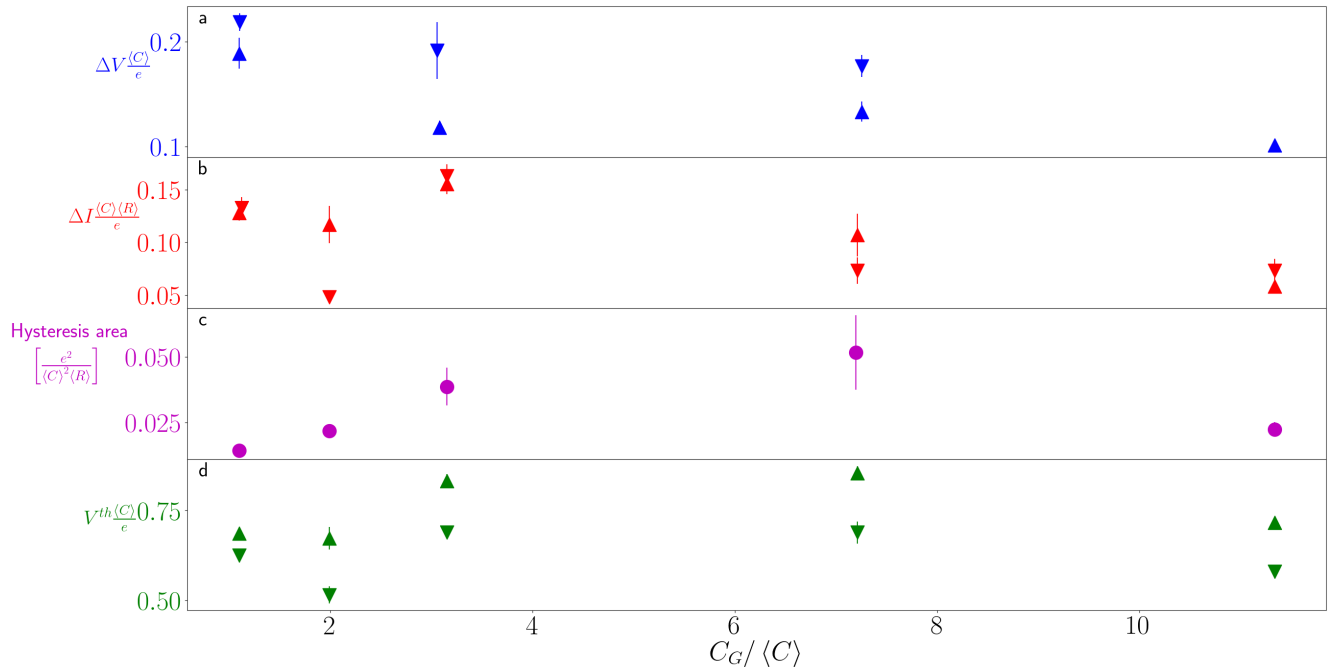


Figure C.1: Hysteresis area, height and separation of jumps, and threshold voltages as a function of gate capacitance, for different disorder realizations. Calculated by averaging the results from > 10 different array realizations for each data point. Error bars show standard error of averages. Upwards pointing triangles - increasing voltage. Downwards pointing triangles - decreasing voltage. **(a)** Jumps average separation. **(b)** Jumps height. **(c)** Hysteresis area. **(d)** Threshold voltages. For 3X3 arrays at $T = 0$. **Common parameters:** $\phi = 0$, $R_G = 100 \langle R \rangle$, $V_{max} = 2 \langle C \rangle / e$, $\sigma_C = 0.9 \langle C \rangle$, $\sigma_R = 2 \langle R \rangle$.

Fig. C.1 shows the dependency of jump separation and height, hysteresis area and threshold voltage on gate capacitance, for different disorder realizations. When changing C_G for the same realization, we saw (in chapter 4) that hysteresis loop area and threshold voltage both grow. Here it seems like they do increase with C_G up to a certain values, but then decrease when C_G keeps increasing. This can be the result of an optimal value for C_G , where jumps are not too small and $V_{\uparrow \downarrow}$ is big enough. Another option is that the dependency of hysteresis area and threshold voltage in C_G is weaker than their dependency on disorder realization (of tunneling resistance and capacitance) and we need more simulation results to average this dependency out, leaving us only with C_G dependency.

Jumps height and separation between jumps decrease with disorder (at least for high C_G), as for the single island case.

C.2 Tunneling capacitance and resistance

In fig C.2a,b simulation results for 1×2 arrays, with big entrance capacitance and small exit capacitance, are plotted. Although changing entrance and exit capacitance is effecting the average charge (For big capacitance, charge average jumps twice before conducting, while for small capacitance only once), its effect on the I-V curve is limited. For large entrance and exit capacitance we see a slightly bigger current jump than for small capacitance. The effect is much less visible than that of changing entrance and exit resistance (fig. 4.8).

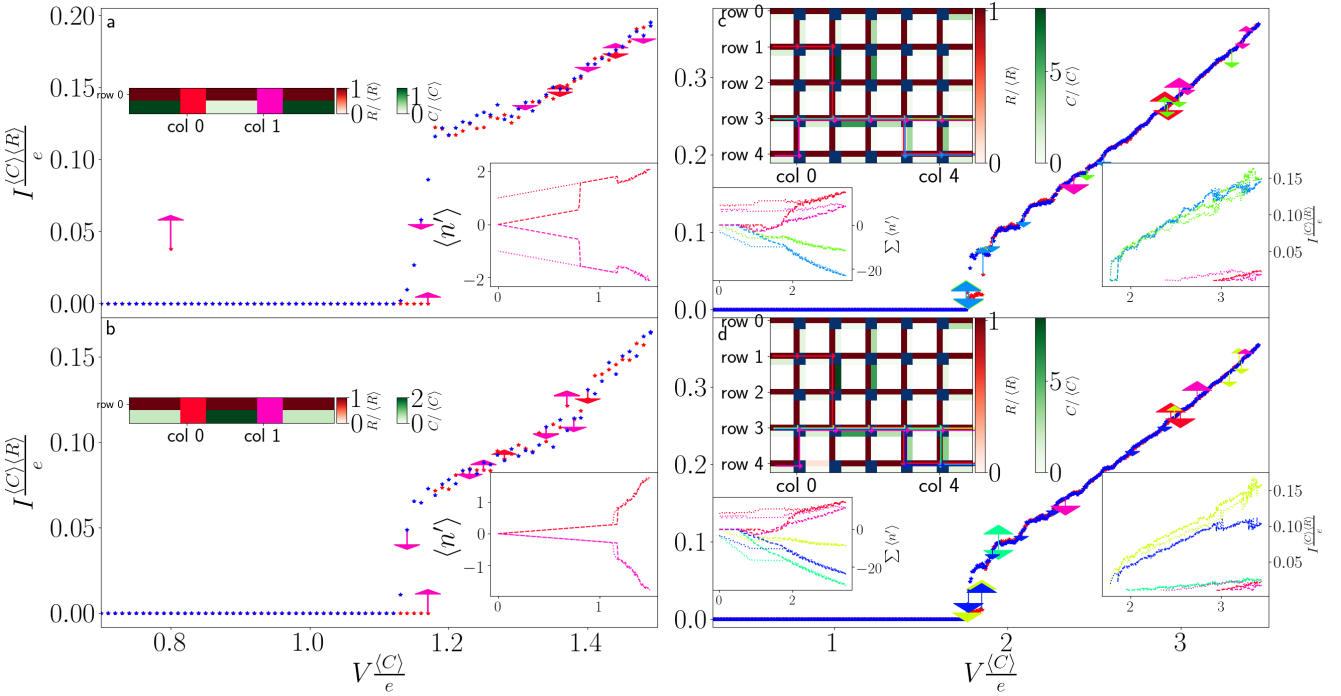


Figure C.2: Tunneling resistance and capacitance effect on current - additional results for 1D and 2D arrays. **Main figures:** I-V curves, red - increasing voltage, blue - decreasing voltage. Small arrows indicate occupation jumps with a different color for each island (a-b) or current jumps with a different color for each path (c-d). The same colors are used for insets. **Upper insets:** Resistance (red) and capacitance (green) of tunneling junctions. Each island (a-b) or path (c-d) is marked with its color. **Lower right insets:** Island average occupation $\langle n' \rangle$ (a-b) or current in each path (c-d) as a function of V . **Lower left subplots** sum of average occupations for all islands in each path (color indicating path). (a) 1D array with large entrance and exit capacitance. (b) 1D array with small entrance and exit capacitance. (c) The same array as in (4.8d), with smaller resistance in the middle of a conducting path (column 3 between rows 3 and 4). The partition of current to different paths had changed slightly, but there is no significant change to the total current. (d) The same array from (4.8d), with smaller resistance in a non-conducting junction. There is no significant change to current. **Common parameters:** $\phi = 0$, $R_G = 100 \langle R \rangle$. (a): $C_{max}/C_{min} = 4$. (b): $C_{max}/C_{min} = 7$ (c-d): $\sigma_C = 0.648 \langle C \rangle$. $R_{max}/R_{min} = 10$.

In fig. C.2c,d, we used the same array from 4.8d with small changes. In C.2c, we changed the tunneling resistance for one junction in the middle of a conducting path. In C.2d, we changed the

tunneling resistance for one non-conducting junction. For both cases there is no significant change to the I-V curve.

Appendix D

Perpendicular electrons temperature

One strong experimental evidence, supporting electrons-overheating model [3], was given by Levinson et. al. [35]. In their experiment, they have calculated the temperature of electrons using 2 different measurements, and showed they get good agreement between the results. To do that, they have followed these steps:

1. Created a rectangular sample. 2 electrodes were connected to both sides of the long, x -axis. 2 more electrodes were connected to both sides of the short, y -axis. y -axis electrodes are only connected to the middle of their edges, while the x -axis ones are connected to all of their edges (see fig 4.15a).
2. Measured the current in both x and y directions, while applying different DC voltages between x electrodes, and small AC voltage, with constant amplitude, between y electrodes. The results of these measurements were used to calculate the resistance in both directions, using Ohm's law, $R^{x/y} = V^{x/y} / I^{x/y}$.
3. Relations between resistance and electrons temperature were measured by applying small AC voltage, separately for each direction, and slowly changing the temperature. This way electrons have enough time to restore thermal equilibrium with environment, and therefore their temperature may be assumed to be the same as environment's. Calculating the resistance, for each direction (using Ohm's law) they obtained the relation $T(R_{x/y})$.
4. Using the relation obtained in (3), and the measured resistance from (2), electrons temperature was calculated for each direction, $T_{el}^{x/y} = T^{x/y}(R^{x/y})$.

This procedure had been repeated for numerous external magnetic field strengths. The calculated values of T_{el}^{el} had a very good agreement. For strong magnetic fields ($B > 0.15T$), $|T_{el}^x - T_{el}^y| / T_{el}^x$ was smaller than 0.05. For weaker magnetic fields the agreement was worse, but not too bad, $|T_{el}^x - T_{el}^y| / T_{el}^x < 0.3$.

To test if our model can reproduce these results we followed a similar procedure. We ran simulations for 5×15 normal arrays, with boundary terms that match electrodes connection in the experiment. Instead of using AC voltage, we ran our simulation twice for each value of V_x . In the first run, voltage on the upper electrode was slightly higher than the lower. In the second, upper and lower voltages were flipped. Current in the x direction was calculated as the average of those 2 runs. Current in the y direction was calculated as the RMS of results. To calculate $T(R^{x/y})$, we used the same simulation, changing temperature instead of voltage. V_x had a constant value, slightly below threshold.

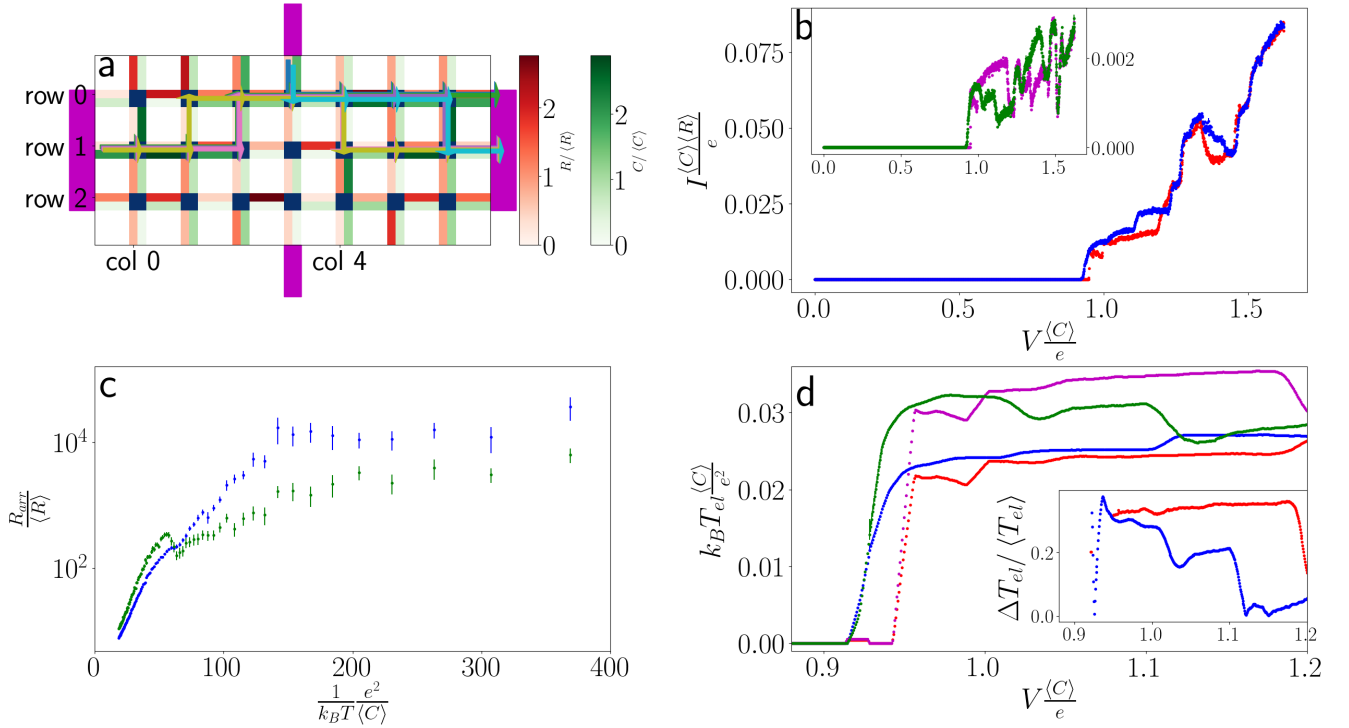


Figure D.1: Perpendicular electron temperature Results for 3×7 array, for $C_G = 8 \langle C \rangle$.
(a) Array parameters. Tunneling resistance (red) and capacitance (red) between conducting islands (blue). Electrodes locations are marked in purple. Current paths for maximum voltage are marked by colored arrows. They are plotted for $V_U > V_D$. **(b)** I-V curve for horizontal (x) direction. Subset - perpendicular (y) direction. Blue and green - decreasing voltage, red and purple - increasing voltage. **(c)** Array resistance as a function of temperature. Blue - horizontal (x) direction, green - vertical (y) direction. **(d)** Electrons temperature, calculated using the results from (b), (c): Red - x-direction, increasing V ; Blue - x-direction, decreasing V ; Purple - y-direction, increasing V ; Green - y-direction decreasing V . Inset - measurement difference, normalized by mean. Red - increasing V , blue - decreasing V . **Parameters:** $|V^y| = 0.06 \frac{e}{\langle C \rangle}$, $\phi = 0$ $R_G = 184 \langle R \rangle$, $C_G = 8 \langle C \rangle$, $\sigma_R = 3.4 \langle R \rangle$, $\sigma_C = 0.5 \langle C \rangle$. For I-V simulation (b): $k_B T = 0.6 \cdot 10^{-3} \frac{e^2}{\langle C \rangle}$, $V_{max}^x = 1.6 \frac{e}{\langle C \rangle}$. For I-T simulation (c): $k_B T_{max} = 0.05 \frac{e^2}{\langle C \rangle}$, $V^x = 0.81 \frac{e}{\langle C \rangle}$

D.1 Simulation results

Simulation results are plotted in figures 4.15, D.1, D.2 and D.3, including intermediate results. These results offer an alternative explanation o the measurement results from [35]. Since voltage differences are higher for x -axis, it is easier for carriers to flow from left to right than it is from up to bottom. Therefore, most of the current measured in y direction comes from paths connecting an x -axis electrode to a y -axis one. This is, in our model, the reason for correlation between perpendicular currents. For voltages near threshold, which are also near the ones used to calculate $T(R)$ this correlation between currents will translate to the same T_{el} .

When V^x increases, there are two possibilities. For samples with high disorder (fig. 4.15, D.1), paths from x to y would still be more dominant. In that case, R^x decreases slower than R^y and we calculate higher electrons temperature in the y -direction. This is a consequence of the way those resistances were calculated, $R^{x/y} = V^{x/y}/I^{x/y}$. In our simulation V^x increases with I^x , but V^y remains constant, while

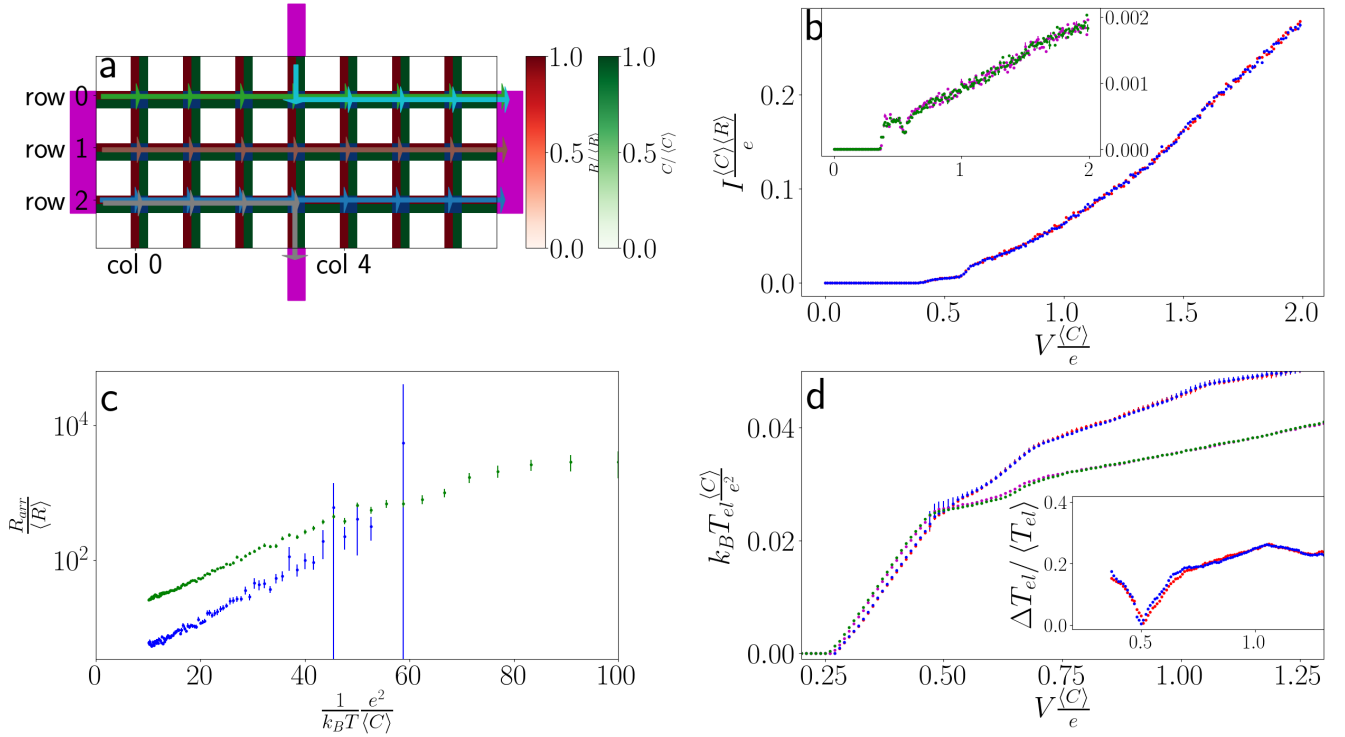


Figure D.2: Perpendicular electron temperature Results for 5 array, for $C_G = \langle C \rangle$ and no disorder. **(a)** Array parameters. Tunneling resistance (red) and capacitance (red) between conducting islands (blue). Electrodes locations are marked in purple. Current paths for maximum voltage are marked by colored arrows. They are plotted for $V_U > V_D$. **(b)** I-V curve for horizontal (x) direction. Subset - perpendicular (y) direction. Blue and green - decreasing voltage, red and purple - increasing voltage. **(c)** Array resistance as a function of temperature. Blue - horizontal (x) direction, green - vertical (y) direction. **(d)** Electrons temperature, calculated using the results from (b), (c): Red - x-direction, increasing V ; Blue - x-direction, decreasing V ; Purple - y-direction, increasing V ; Green - y-direction decreasing V . Inset - measurement difference, normalized by mean. Red - increasing V , blue - decreasing V . **Parameters:** $|V^y| = 0.1 \frac{e}{\langle C \rangle}$, $\phi = 0$ $R_G = 100 \langle R \rangle$, $C_G = \langle C \rangle$, $\sigma_R = 0$, $\sigma_C = 0$. For I-V simulation (b): $k_B T = 1 \cdot 10^{-3} \frac{e^2}{\langle C \rangle}$, $V_{max}^x = 2 \frac{e}{\langle C \rangle}$. For I-T simulation (c): $k_B T_{max} = 0.1 \frac{e^2}{\langle C \rangle}$, $V^x = 0.5 \frac{e}{\langle C \rangle}$

I^y increases (because of increasing V^x). For samples with low disorder (D.2 and D.3), left to right paths become more dominant and we would measure lower R^x and thus higher T_{el}^x .

The agreement between T_{el}^x and T_{el}^y is better for samples with higher disorder. This might explain the better agreement for high magnetic fields (which are associated with higher disorder) that was measured in [35].

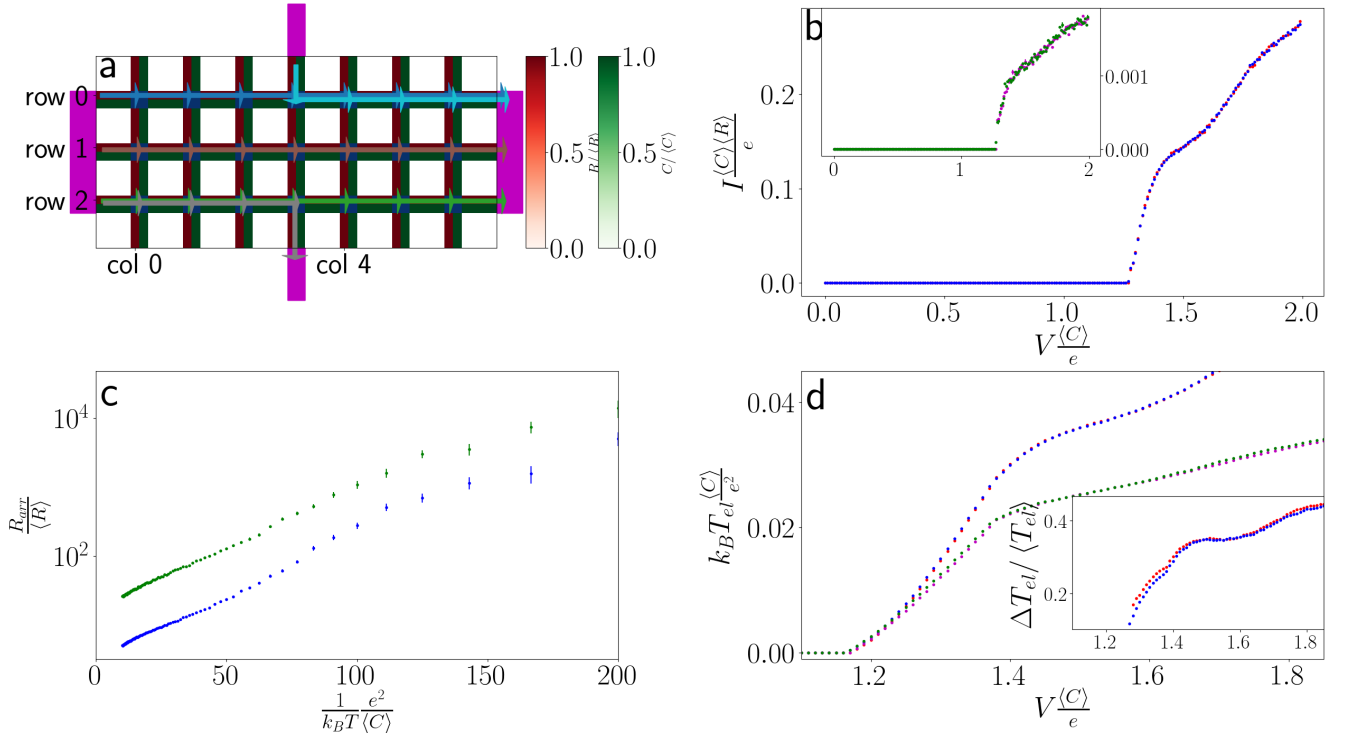


Figure D.3: Perpendicular electron temperature Results for 3×7 array, for $C_G = 5 \langle C \rangle$ and no disorder. (a) Array parameters. Tunneling resistance (red) and capacitance (red) between conducting islands (blue). Electrodes locations are marked in purple. Current paths for maximum voltage are marked by colored arrows. They are plotted for $V_U > V_D$. (b) I-V curve for horizontal (x) direction. Subset - perpendicular (y) direction. Blue and green - decreasing voltage, red and purple - increasing voltage. (c) Array resistance as a function of temperature. Blue - horizontal (x) direction, green - vertical (y) direction. (d) Electrons temperature, calculated using the results from (b), (c): Red - x-direction, increasing V ; Blue - x-direction, decreasing V ; Purple - y-direction, increasing V ; Green - y-direction decreasing V . Inset - measurement difference, normalized by mean. Red - increasing V , blue - decreasing V . **Parameters:** $|V^y| = 0.1 \frac{e}{\langle C \rangle}$, $\phi = 0$ $R_G = 100 \langle R \rangle$, $C_G = 5 \langle C \rangle$, $\sigma_R = 0$, $\sigma_C = 0$. For I-V simulation (b): $k_B T = 1 \cdot 10^{-3} \frac{e^2}{\langle C \rangle}$, $V_{max}^x = 2 \frac{e}{\langle C \rangle}$. For I-T simulation (c): $k_B T_{max} = 0.1 \frac{e^2}{\langle C \rangle}$, $V^x = 1 \frac{e}{\langle C \rangle}$

Bibliography

Book Sources

45. Tinkham, M. *Introduction to superconductivity* (Courier Corporation, 2004).

Article Sources

1. Otterlo, A., Bobbert, P. A. & Schön, G. Charge dynamics in junction arrays. *Helvetica Physica Acta* **65**, 379–380 (1992).
2. Agren, P., Johansson, J., Andersson, K. & Haviland, D. Hysteretic current–voltage characteristics and Coulomb blockade in 1D-arrays of Josephson junctions. *Physica B: Condensed Matter* **280**, 414–415 (2000).
3. Altshuler, B. L., Kravtsov, V. E., Lerner, I. V. & Aleiner, I. L. Jumps in Current-Voltage Characteristics in Disordered Films. *Physical Review Letters* **102**, 176803 (2009).
4. Ambegaokar, V., Halperin, B. I. & Langer, J. S. Hopping Conductivity in Disordered Systems. *Physical Review B* **4**, 2612–2620 (1971).
5. Averin, D. V. & Likharev, K. K. Coulomb blockade of single-electron tunneling, and coherent oscillations in small tunnel junctions. *Journal of Low Temperature Physics* **62**, 345–373 (1986).
6. Bakhvalov, N. S., Kazacha, G. S., Likharev, K. K. & Serdyukova, S. I. Statics and dynamics of single-electron solitons in two-dimensional arrays of ultrasmall tunnel junctions. *Physica B: Condensed Matter* **173**, 319–328 (1991).
7. Bardeen, J., Cooper, L. N. & Schrieffer, J. R. Theory of Superconductivity. *Physical Review* **108**, 1175–1204 (1957).
8. Baturina, T. I., Mironov, A. Y., Vinokur, V. M., Baklanov, M. R. & Strunk, C. Localized Superconductivity in the Quantum-Critical Region of the Disorder-Driven Superconductor-Insulator Transition in TiN Thin Films. *Physical Review Letters* **99**, 257003 (2007).
9. Baturina, T. I. et al. Quantum-critical region of the disorder-driven superconductor-insulator transition. *Physica C: Superconductivity. Proceedings of the Workshop on Fluctuations and Phase Transitions in Superconductors* **468**, 316–321 (2008).
10. Baturina, T. I. & Vinokur, V. M. Superinsulator–superconductor duality in two dimensions. *Annals of Physics* **331**, 236–257 (2013).
11. Böttcher, C. G. L. et al. Superconducting, insulating and anomalous metallic regimes in a gated two-dimensional semiconductor–superconductor array. *Nature Physics* **14**, 1138–1144 (2018).

12. Cohen, O., Ovadia, M. & Shahar, D. Electric breakdown effect in the current-voltage characteristics of amorphous indium oxide thin films near the superconductor-insulator transition. *Physical Review B* **84**, 100507 (2011).
13. Cole, J. H., Leppäkangas, J. & Marthaler, M. Correlated transport through junction arrays in the small Josephson energy limit: incoherent Cooper-pairs and hot electrons. *New Journal of Physics* **16**, 063019 (2014).
14. Cren, T., Roditchev, D., Sacks, W. & Klein, J. Nanometer scale mapping of the density of states in an inhomogeneous superconductor. *Europhysics Letters* **54**, 84–90 (2001).
15. Doron, A., Levinson, T., Gorniaczyk, F., Tamir, I. & Shahar, D. The critical current of disordered superconductors near 0 K. *Nature Communications* **11**, 2667 (2020).
16. Dubi, Y., Meir, Y. & Avishai, Y. Nature of the superconductor–insulator transition in disordered superconductors. *Nature* **449**, 876–880 (2007).
17. Duruöz, C. I., Clarke, R. M., Marcus, C. M. & Harris J. S., J. Conduction Threshold, Switching, and Hysteresis in Quantum Dot Arrays. *Physical Review Letters* **74**, 3237–3240 (1995).
18. Efetov, K. B. Phase transition in granulated superconductors. *Journal of Experimental and Theoretical Physics*, 8 (1980).
19. Février, P. & Gabelli, J. Tunneling time probed by quantum shot noise. *Nature Communications* **9**, 4940 (2018).
20. Fisher, M. P. A. Quantum phase transitions in disordered two-dimensional superconductors. *Physical Review Letters* **65**, 923–926 (1990).
21. Frydman, A., Naaman, O. & Dynes, R. C. Universal transport in two-dimensional granular superconductors. *Physical Review B* **66**, 052509 (2002).
22. Gantmakher, V. F. & Dolgopolov, V. T. Superconductor–insulator quantum phase transition. *Physics-Uspekhi* **53**, 1 (2010).
23. Gillespie, D. T. Approximate accelerated stochastic simulation of chemically reacting systems. *The Journal of Chemical Physics* **115**, 1716–1733 (2001).
24. Gillespie, D. T. Exact stochastic simulation of coupled chemical reactions. *The Journal of Physical Chemistry* **81**, 2340–2361 (1977).
25. Grabert, H. *et al.* Single electron tunneling rates in multijunction circuits. *Zeitschrift für Physik B Condensed Matter* **84**, 143–155 (1991).
26. Haviland, D. B., Liu, Y. & Goldman, A. M. Onset of superconductivity in the two-dimensional limit. *Physical Review Letters* **62**, 2180–2183 (1989).
27. Hebard, A. F. & Paalanen, M. A. Magnetic-field-tuned superconductor-insulator transition in two-dimensional films. *Physical Review Letters* **65**, 927–930 (1990).
28. Josephson, B. D. Possible new effects in superconductive tunnelling. *Physics Letters* **1**, 251–253 (1962).
29. Kamerlingh Onnes, H. Further experiments with liquid helium. *Communication, Leiden* **120b**, **122b**, **124c**, 1479–1481, 81–83, 799–812 (1911).

31. Kardar, M., Parisi, G. & Zhang, Y.-C. Dynamic Scaling of Growing Interfaces. *Physical Review Letters* **56**, 889–892 (1986).
32. Kautz, R. L. & Martinis, J. M. Noise-affected I - V curves in small hysteretic Josephson junctions. *Physical Review B* **42**, 9903–9937 (1990).
33. Korotkov, A. N. Single-electron transistor controlled with a RC circuit. *Physical Review B* **49**, 16518–16522 (1994).
34. Kravchenko, S. V. & Sarachik, M. P. A metal-insulator transition in 2D: Established facts and open questions. *International Journal of Modern Physics B* **24**, 1640–1663 (2010).
35. Levinson, T., Doron, A., Tamir, I., Tewari, G. C. & Shahar, D. Direct determination of the temperature of overheated electrons in an insulator. *Physical Review B* **94**, 174204 (2016).
36. Ma, M. & Lee, P. A. Localized superconductors. *Physical Review B* **32**, 5658–5667 (1985).
37. Meissner, W. & Ochsenfeld, R. Ein neuer Effekt bei Eintritt der Supraleitfähigkeit. *Naturwissenschaften* **21**, 787–788 (1933).
38. Middleton, A. A. & Wingreen, N. S. Collective transport in arrays of small metallic dots. *Physical Review Letters* **71**, 3198–3201 (1993).
39. Ovadia, M., Sacépé, B. & Shahar, D. Electron-Phonon Decoupling in Disordered Insulators. *Physical Review Letters* **102**, 176802 (2009).
40. Pilling, G., Cobden, D. H., McEuen, P. L., Duruöz, C. I. & Harris, J. S. Intrinsic bistability in nonlinear transport through a submicron lateral barrier. *Surface Science* **361-362**, 652–655 (1996).
41. Prados, A., Brey, J. J. & Sánchez-Rey, B. A dynamical monte carlo algorithm for master equations with time-dependent transition rates. *Journal of Statistical Physics* **89**, 709–734 (1997).
42. Rahman, M. A., Rahaman, M. Z. & Samsuddoha, M. N. A Review on Cuprate Based Superconducting Materials Including Characteristics and Applications. *American Journal of Physics and Applications* **3**, 39 (2015).
43. Sambandamurthy, G., Engel, L. W., Johansson, A., Peled, E. & Shahar, D. Experimental Evidence for a Collective Insulating State in Two-Dimensional Superconductors. *Physical Review Letters* **94**, 017003 (2005).
44. Staley, N. E., Ray, N., Kastner, M. A., Hanson, M. P. & Gossard, A. C. Electric-field-driven insulating-to-conducting transition in a mesoscopic quantum dot lattice. *Physical Review B* **90**, 195443 (2014).
46. Whan, C. B., White, J. & Orlando, T. P. Full capacitance matrix of coupled quantum dot arrays: Static and dynamical effects. *Applied Physics Letters* **68**, 2996–2998 (1996).
47. Yudson, V. I. & Kravtsov, V. E. Electron kinetics in isolated mesoscopic rings driven out of equilibrium. *Physical Review B* **67**, 155310 (2003).

תוכן עניינים

| | |
|----|---|
| 1 | 1 מבוא |
| 1 | 1.1 על-مولיכות ומעבר פאזה מעיל-מוליך למבודד |
| 2 | 1.2 אופיין זרם-מתה בקרבת מעבר הפאזה |
| 2 | 1.3 תוצאות דומות במערכות אחרות |
| 3 | 1.4 מטרות המחק |
| 4 | 2 סקירת ספרות |
| 4 | 2.1 מודל מערכם אקראים |
| 4 | 2.1.1 קצב מנהור |
| 5 | 2.1.2 חישוב אופיין זרם-מתה |
| 6 | 2.1.3 מערכם רגילים |
| 7 | 2.1.4 מערכם על-מוליכים |
| 8 | 2.1.5 השוואה לתוצאות הניסוי |
| 8 | 2.2 מודל זמומייתר של האלקטرونים |
| 9 | 2.2.1 השוואה לתוצאות הניסוי |
| 10 | 2.3 סיכום |
| 11 | 3 הצגת המודל |
| 11 | 3.1 מודל לאי בודד $RC - SET$ |
| 12 | 3.1.1 הפרדת סקלאות זמן |
| 13 | 3.2 הכללה למערך אקראי |
| 13 | 3.2.1 רלקסציה בין מנהורים |
| 15 | 3.2.2 אנרגיה |
| 16 | 3.2.3 מרחק אינטראקציה |
| 17 | 3.2.4 משווהת מסטר |
| 17 | 3.3 סימולציות דינמיות |
| 18 | 3.4 פתרון בעזרת גרפ, עבור $T = 0$ |
| 18 | 3.4.1 פתרון משווהת מסטר |
| 19 | 3.4.2 מטען במצב יציב עבור רלקסציה איטית |
| 20 | 3.5 מימוש אידסדר |
| 21 | 4 תוצאות |
| 21 | 4.1 אי בודד |
| 21 | 4.1.1 תנאים להיסטרוזיס וקפיצות |
| 23 | 4.1.2 גודל היסטרוזיס וקפיצות |
| 24 | 4.1.3 מתח סף |
| 26 | 4.1.4 חוק Arrhenius |

| | |
|-------------------|---|
| 26 | 4.1.5 סיכום |
| 27 | 4.2 מערכים |
| 29 | 4.2.1 אינטראקציות בין מסלולים שונים |
| 30 | 4.2.2 קיבול צמחי מנהור |
| 32 | 4.2.3 התנגדות צמחי מנהור |
| 34 | 4.2.4 קיבול גיט |
| 35 | 4.2.5 טמפרטורה |
| 37 | 4.2.6 מערכים על-مولיכים |
| 39 | 4.3 השוואה למודלים אחרים |
| 39 | 4.3.1 מודלים של מערכאים אקראים |
| 40 | 4.3.1 מודל חימום-יתר של האלקטרונים |
| 42 | 4.4 סיכום התוצאות |
| 44 | 5 דיוון ומסקנות |
| 44 | 5.1 מגבלות המחקר |
| 45 | 5.2 הצעות למחקר עתידי |
| 45 | 5.3 מסקנות |
| <i>i</i> | <i>A</i> ניתוח מפורט של אי בודד |
| <i>i</i> | <i>A.1</i> גיורת נסחאות המודל |
| <i>i</i> | <i>A.1.1</i> רלקסציה בין מנהורים |
| <i>ii</i> | <i>A.1.2</i> קצב מנהור |
| <i>iii</i> | <i>A.2</i> פתרון משווה מסטר עבור $T = 0$ |
| <i>iii</i> | <i>A.2.1</i> איכלוס מינימלי ומקסימלי באי |
| <i>iv</i> | <i>A.2.2</i> הסתברויות מצב יציב |
| <i>iv</i> | <i>A.2.3</i> פתרון עבור $V \geq 0$ |
| <i>vii</i> | <i>A.2.4</i> זרם מצב יציב עבור רלקסציה מהירה |
| <i>viii</i> | <i>A.2.5</i> מטען וזרם במצב יציב לרלקסציה איטית |
| <i>xii</i> | <i>A.2.6</i> כפיצות זרם עבור רלקסציה איטית |
| <i>xvi</i> | <i>A.2.7</i> מתח סף |
| <i>xix</i> | <i>B</i> מטריצת קיבול עבור שני איים |
| <i>xix</i> | <i>B.1</i> מערך בגודל 1×2 |
| <i>xx</i> | <i>B.2</i> מערך בגודל 2×1 |
| <i>xx</i> | <i>B.3</i> דיוון |
| <i>xxii</i> | <i>C</i> תוצאות נוספות |
| <i>xxii</i> | <i>C.1</i> קיבול גיט |

| | | |
|--------------|---------------------------------|------------|
| <i>xxiii</i> | קיבול והתנגדות צמחי מנהור | <i>C.2</i> |
| <i>xxv</i> | טמפרטורת אלקטرونים במאונך | <i>D</i> |
| <i>xxvi</i> | תוצאות סימולציה | <i>D.1</i> |

אוניברסיטת בן-גוריון בנגב

תקציר

הפקולטה למדעי הטבע
המחלקה לפיסיקה

תואר "מוסמך" בפקולטה למדעי הטבע

מודל תיאודטי להיסטרוזים וקפיצות במוליכי-על דו-dimensionים לא מסודרים, בסמו^ך
למעבר הפהה מ מוליך-על למבודד

מאת: שחר כסירר

בניסויים שונים עם מוליכי-על לא מסודרים התגלה כי חומרים אלו עוברים מעבר פואה, מ מוליך-על למבודד, כאשר איזהסדר, או השدة המגנטית, גדול. לפאה המבודדת ישן תכונות בלתי רגילות, אחת מהן היא אופיין המתח-זרום, אשר לעיתים כולל היסטרוזים וקפיצות בזרם הנמדד. מערכות נוספות, בהן נצפתה התנהגות דומה, הן מערכות של איים מוליכים, או מוליכי-על, המחוורבים על ידי צמתים מנהור. הדרך הנפוצה לממדל חומרים אלו הינה כרשת של נגדים וקובלים, כאשר אל המנהור מתיחסים כהפרעה קטנה למצב בו יש מספר מוגדר של נושא-אימטען על כל אי. במודלים אלו מניחים בדרך כלל כי הרלקסציה לשינוי-משקל (תרמי או אלקטростטי) הינה מהירה, כך שהמערכת חוזרת לשינוי משקל מיד אחריו כל מנהור, لكن ניתן התיחס למערכת כאילו היא תמיד נמצאת בשינוי-משקל. מודלים אלו משוחרים בהצלחה חלק מהתוצאות המדיניה, כולל מעבר הפואה עצמו, אך נכשלים בשחוור היסטרוזים וקפיצות באופיין הזרם-ימתח. במחקר זה אנחנו מתחקים בגבול הרלקסציה האיטית, בו המערכת לא בהכרח נמצאת בשינוי-משקל בין מנהורים. לשם כך, אנחנו משתמשים במודל עבור אי מוליך בודד, שהוצע על ידי Korotkov [33]. אנחנו מנתחים את תכונות ההולכה של המודל, ומרחיבים אותו למודל עבור מערך אקראי, כאשר איזהסדר ממושך עליידי בחירת התנגדות וקיים אקראים עבור כל צומת מנהור. אנחנו משתמשים בסימולציות Monte – Carlo קינטיות [24] כדי לחשב את התלות של הזרם במתח ובטמפרטורה, עבור מערכיים אקראים שונים. אנחנו מראים שמודול זה יכול לשחוור היסטרוזים וקפיצות בזרם, עבור פרמטרים מסוימים, וכי תוצאותיו מסקימות, באופן איקוטי, עם התוצאות שנמדדנו בניסוי. אנחנו מנתחים את השפעת הפרמטרים השונים של המודל ומשווים את התוצאות עם מודלים קיימים. אנו מסיים עם הצעות לדריכים בהן ניתן להשתמש במודל זה לצורכי מחקר עתידי.



אוניברסיטת בן-גוריון בנגב
הפקולטה למדעי הטבע
המחלקה לפיזיקה

**נושא החיבור: מודל תיאורטי להיסטרזים וקפיות במולכיד-על דו-מימדיים לא
מסודרים, בסמוך למעבר הפואה ממוליך-על למבודד**

חיבור זה מהווה חלק מהדרישות לקבלת התואר "מוסמן" בפקולטה למדעי הטבע

מאת: **שחר כסידר**

בנהנחת **פרופסור יגאל מאיר**

תאריך לועזי: 13.01.2021

תאריך עברית: כ"ט בטבת ה'תשפ"א